FAULT DETECTION AND IDENTIFICATION IN PERMANENT MAGNET SYNCHRONOUS MACHINES

By

Reemon Zaki Saleem Haddad

A DISSERTATION

Submitted to
Michigan State University
in partial fulfillment of the requirements
for the degree of

Electrical Engineering - Doctor of Philosophy

2016

ABSTRACT

FAULT DETECTION AND IDENTIFICATION IN PERMANENT MAGNET SYNCHRONOUS MACHINES

By

Reemon Zaki Saleem Haddad

Permanent Magnet Synchronous Machines are subject to a variety of failures in various parts of their structure. These faults cause different and independent changes to the motor parameters and its response behavior. This requires different detection and mitigation methods based on the fault type, location, and severity. Therefore, an effective fault detection and identification method is required, not only to identify if the motor is healthy or faulted, but to detect the fault type, separate it from others, and estimate its severity.

In this research, an algorithm is proposed to detect and separate between different faults in Permanent Magnet Synchronous Machines under different operating conditions. The incremental inductance approach is proposed when the motor it at standstill. This method uses the changes in the machine saturation, due to the presence of faults, as a fault indicator. Under steady state operation, the change in the machine commanded voltages is proposed as a fault indicator. However, if the motor is operating at steady state with high torque, the motor current or voltage signature analysis is proposed. The main advantage of the proposed method is that it doesn't require any additional hardware components. The same signals that are used for the controller can be used for fault detection, separation, and estimation. The proposed methods also does not require a complicated signal processing techniques. This makes the proposed methods fast, cost efficient and easy to implement.

Three common faults in Permanent Magnet Synchronous Machines are discussed in this work: static eccentricity, partial demagnetization and turn-to-turn short circuit faults. Finite

Element Analysis simulations and experimental testes were carried out for three Permanent Magnet Synchronous Machines under healthy and the faulted conditions. The differences between the motors are the winding topology, the input/output power, and the slot/pole combination. The first motor is a 12 poles, 72 slots with a distributed windings, the second motor is a 16 poles, 48 slots with a concentrated windings, the final machine is a 10 poles, 12 slots fractional slots concentrated winding machine. Both simulations and experimental results showed that the proposed methods were able to separate between the different faults with a high level of accuracy.

I dedicate this Dissertation to the memory of my beloved father, Zaki Haddad who helped during every stage of my life. A special gratitude to my loving mother, Asma Dababneh, and my family members, Rwena Haddad, Rami Haddad, Rani Haddad and Renada Haddad, who offered me unconditional love and support during my study.

I would like also to dedicate this work to my future wife, Mingming Zhou her patience and support was my inspiration and motivation. Thank you for all that you do and all that you are.

ACKNOWLEDGMENTS

First and above all, I praise God for providing me this opportunity and for the health, ability and strength to be where and who I am now.

I would like to express my special appreciation and thanks to my research advisor Professor Elias G. Strangas, for his support, assistance, guidance, and motivation to pursue and complete my doctoral degree. Also, I would like thank my graduate committee; Prof. Jose Antonino Daviu, Prof. Selin Aviyente, and Dr. Shanelle Foster, for their guidance and support.

A special thanks to my friends at Michigan State University, especially in the Electrical Machines and Drives Laboratory. I am grateful to have the opportunity to meet these amazing people who helped me during my PhD study. I would like to thank Cristian Lopez-Martinez, Rodney Singleton, Thang Pham, William Jensen, Steve Hayslett, Dr. Andrew Babel, Dr. Jorge G. Cintron-Rivera, Eduardo Montalvo-Ortiz, Arslan Qaiser, Muhammad Jawad Zaheer, and Zaid Bataineh. Their help, support, and advice made this work possible. I would also like to thank Jordan University of Science and Technology who supported me financially during my study.

Finally, I would like to thank my mother and my family members, who encouraged me to start my Ph.D and continues to support throughout my future goals and carrier. I would have never reached this point without their love and support.

TABLE OF CONTENTS

LIST OF TABLES

LIST OF FIGURES

Chapter 1

Introduction

1.1 Motivation

Permanent Magnet Synchronous Machines (PMSMs) are playing a major role in a wide array of industrial and automotive applications due to their high efficiency, reliability, wide operation range, and their high torque density. These applications include power traction and steering in electric/hybrid vehicles, robotics, household applications, power tools, and wind generators. The growth of use of PMSMs in the market has driven these machines to be exposed to different types of faults. Faults in PMSMs can be classified into three main categories: stator faults, rotor faults and bearing faults. Stator faults include turn-to-turn short circuit, phase-to-phase short circuit, phase-to-neutral short circuit, and open circuit faults. Rotor faults include eccentricity and demagnetization faults. Bearing faults include outer race, inner race, and ball bearing faults. Based on the industrial and commercial industries report [4] 10% of the total faults are related to rotor faults, 37% are related to stator faults and 41% are related to bearing faults.

The main objective of condition monitoring in electric machines is to capture the presence of faults and estimate the severity while it's still in the early stages. Detecting the machine health status and implement the suitable maintenance method, in the case of faulted cases, can help increase the motor reliability, maximize the machine operating lifetime, and reduce the maintenance cost.

1.2 Problem Statement

Faults develop in different ways and causes different changes to the machine parameters and performance. Depending on the fault type, severity, and location, different detection and mitigation methods can be implemented. These methods can be categorized as either interruption of the machine operation or change in the controller scheme. Some faults require an immediate actions to be performed to the machine, while other faults allow the machine to operate normally, if the fault severity is low, until a safe shutdown is performed to the machine.

Also, in order to avoid catastrophic consequences, it is important to detect the fault while it is still in the early stages. Proper early maintenance can be performed before the fault expands and causes severe damage, not only to the machine but also to humans. The work in this dissertation is focused on developing an algorithm to detect the machine health status (i.e. if the machine is healthy or faulted) under different operating conditions, determine the type of the fault and estimate its severity.

1.3 Literature Review

Several approaches have been proposed in the literature for single fault detection in PMSMs. These methods can be categorized as 1) the motor current or voltage signal analysis [1,5–11], 2) the vibration or noise signals analysis [12–15], 3) model based and analytical methods [16–19], 4) temperature monitoring, 5) flux monitoring [2], and 6) offline methods [20–22].

The Motor Current Signature Analysis (MCSA) or the Motor Voltage Signature Analysis (MVSA) is the most common technique for fault diagnosis. In this approach, frequency analysis using Fast Fourier Transform (FFT) (for steady state operation), or time frequency

analysis methods using Short Time Fourier Transform (STFT), Discrete Wavelet transform (DWT), Continuous Wavelet transform (CWT),... etc (for non stationary operation condition) are applied to the stator current or voltage signals. Features using specific harmonic band can be used as a fault indicator; the amplitude of these signatures are used to estimate the severity. The main advantage of the MCSA is that it does not require any additional hardware component, the current signals are always available for the controller to measure. In addition, this method is non-invasive and cost effective. The stator voltages can also be used for fault detection. It was shown in [23] that if the controller bandwidth is large enough, the signature harmonics that appear in the current signals will also appear in the stator phase voltage signals.

Ebrahimi *et al.* [5] proposed using the spectrum of the measured stator current for detecting eccentricity faults in PMSMs. The sideband frequency pattern given by (1.1) is proposed as an eccentricity faults signatures. The appearance of this sideband pattern in the current spectrum can be used as a fault indicate, and the amplitude of the sideband components can be used to estimate the fault severity. As the severity of eccentricity faults increase, the amplitude of the sideband harmonics will also increase.

$$f_{ecc} = \left(1 \pm \frac{2K-1}{P}\right) f_s \tag{1.1}$$

where P is the number of pole pairs, $K = 1, 2, 3, \ldots$, and f_s is the stator current frequency. It was noticed that in the case of dynamic eccentricity fault, the amplitude of the sideband components were higher compared to the case of static eccentricity fault. This was proposed as an indicator to separate between the two types of eccentricity faults. The same approach was applied to detect short circuit fault in PMSM [7]. The sideband components of the

stator current spectrum given by (1.2) were used as an indicator to detect short circuit fault. Similar to the case of eccentricity faults, the amplitude of the sideband components was used to estimate the severity.

$$f_{sho} = \left(1 \pm \frac{2K+1}{P}\right) f_s \tag{1.2}$$

Fig.1.1 shows a comparison of the normalized stator current spectrum under healthy and faulted PMSM. Fig.1.2a, and Fig.1.2b show the change in the current spectrum under healthy and different severities of static and dynamic eccentricity faults. Fig.1.1c, and Fig.1.1d shows the change in the spectrum of the stator current signal under healthy and different severities of short circuit fault under full load operation.

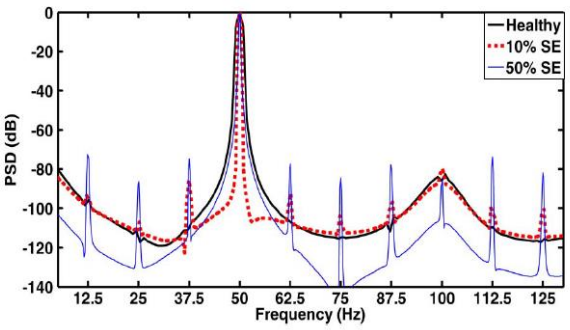

(a) Current spectrum for healthy and eccentricity faults [5]

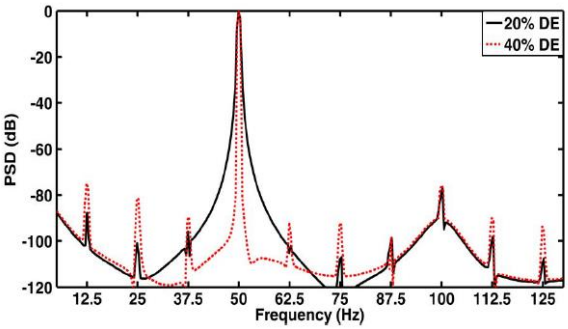

(b) Current spectrum for different severities of dynamic eccentricity fault [5]

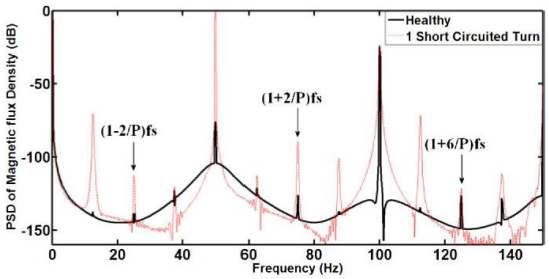

(c) Current spectrum for healthy and short circuit fault [7]

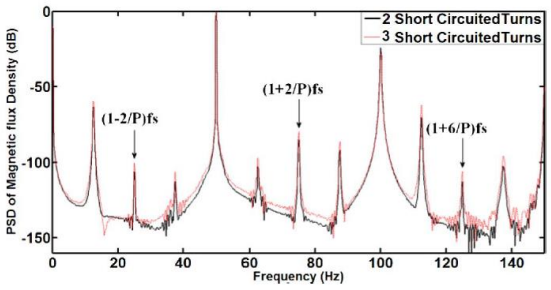

(d) Current spectrum for different severities of short circuit fault [7]

Figure 1.1 Comparison of the current spectrum of PMSM under healthy and different faults for full load operation

The increase in the sideband harmonics given by (1.1) can be observed in the case of eccentricity fault and the increase in the amplitude of the subharmonics given by (1.2) can be noted in the case of short circuit fault. This indicate that these subharmoncis can be used to detect the fault and estimate the severities. [24] is a review paper that describes the different types of faults and the frequency signatures each fault generate and the diagnostics schemes. The main challenge of using the current spectrum is that the fault signatures depend on the machine operating speed and load; at lower speeds it is difficult to detect these sideband patterns [25]. Also, it was shown in [26] and [27], that the relation between the number of poles and the stator slots affects the appearance of the stator current subharmonics in the case of eccentricity faults. All these reasons affect the accuracy of this method as an accurate fault detection and estimation method, since that PMSMs have different topologies, slot/pole combinations, and will be running at different operating conditions.

In [1,6,9–11] time frequency analysis techniques like Wavelet Transform, Wigner Distribution and Zhao-Atlos-Marks Distribution were applied for detecting several fault in PMSMs. Even tho they are capable of faults detection under transient operation. However, these methods require additional hardware components and more complex software. This will increase the total cost and the computational time.

The noise and vibration signals are also widely used for fault detection in PMSMs. Faults cause an increase in the magnetic pull force, which increases the magnetic stress acting on the stator. The magnetic stress is proportional to the square of the magnetic flux density. Therefore, any change in the magnetic flux density is reflected in the noise and vibration signals in the machine. By analysing the vibration signal using FFT or any of the time-frequency analysis methods, fault signatures can be extracted for fault detection and separation. In [15] the sideband components of the vibration spectrum given by 1.3 were proposed for detecting

eccentricity faults in PMSM.

$$f_{ecc} = \left(1 \pm \frac{K}{P}\right) f_s \tag{1.3}$$

Fig.1.2 shows the radial force spectrum for healthy and faulted conditions of PMSM under under static eccentricity fault.

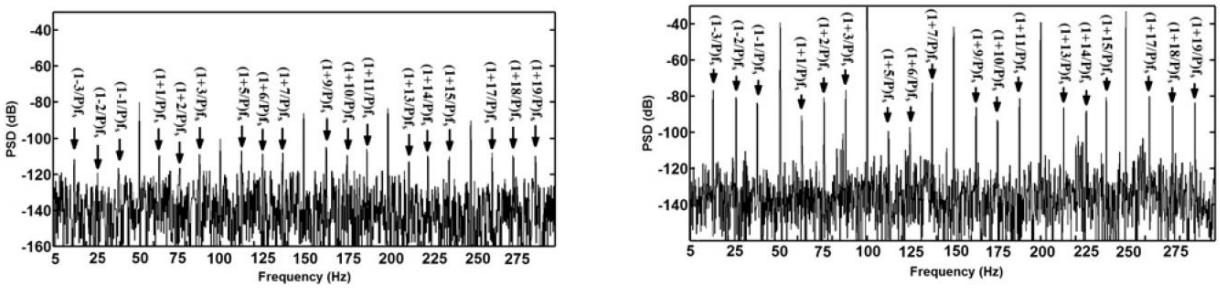

(a) Healthy machine [15]

(b) 30% static eccentricity fault [15]

Figure 1.2 Radial force spectra of the healthy and faulty PMSM under static eccentricity fault

The increase in the subharmonics components given by 1.3 can be observed in the case of eccentricity fault. The main drawback of using the vibration signals is that it requires the installation of a noise and vibration sensor on the motor surface, which might be expensive and not always possible based on the machine placement. Also the corresponding noise level of the machine is affected by the machine operating load and speed.

Analytical approaches and online parameter estimation techniques have the advantage of obtaining an accurate detection results while the motor is operating at different operating conditions. However, these techniques require an accurate model for the motor. This model should accounts for the manufacturing and the environmental variations of the machine. On the other hand, some parameter estimation techniques may require a heavy computation time, which increases the cost and makes the system more complex. Other methods have

Table 1.1 Comparison of fault detection techniques

Detection methods	Types of fault			Drawbacks
	Eccentricity	Stator fault	Demagnetization	
Current/ Voltage	•	•	•	Depend on the speed and load
Noise/ Vibration	•			Extra component and cost
Analytical/ Parameter est.		•	•	accurate model required
Temperature		•		Depend on the load and speed
Flux monitor	•	•	•	additional components
Stand still	•	•	•	Only at standstill

been proposed for fault detection when the motor is at standstill [20, 21]. These methods can be applied for a scheduled check for the motor, and they require a specific test to be applied to the motor. Table.1.1 summarizes the most common detection methods and the types of faults each method can detect.

A few methods have been proposed to separate between different faults. Roux *et al.* [1] proposed a method to separate between eccentricity faults (static and dynamic eccentricity) and broken magnets in PMSMs. It was shown that dynamic eccentricity can be detected using the amplitude of the current sideband harmonics given by $(\frac{K}{P} f_s)$, and static eccentricity can be detected using the change in the amplitude of the 5^{th} and 7^{th} harmonics of the negative sequence current in the *abc* frame of reference. Broken magnets can be detected by comparing the estimated magnetic flux linkage and the actual magnetic flux linkage. The magnetic flux linkage was estimated using the operating speed, the measured voltages and currents as follows:

$$\lambda^{e}_{dpm} = \frac{v_q - r_s i_q}{\omega_r} - L_d i_d \tag{1.4}$$

where v_q is the q-axis voltage, r_s is the stator resistance, i_q is the q-axis flux, ω_r is the electrical speed, L_d is the d-axis inductance, and i_d is the d-axis current. Fig.1.3a shows the current fault frequency components ($0.5 = \frac{1}{P}$ harmonic components where P is the number of pole pair) of a PMSM under healthy, broken magnets and eccentricity fault at different operating conditions. Fig.1.3b shows a comparison of the 7^{th} harmonic of the stator current between healthy and static eccentricity fault at different operating conditions. Fig.1.3c shows a comparison between the estimated magnetic flux linkages for healthy and different faults under different operating conditions.

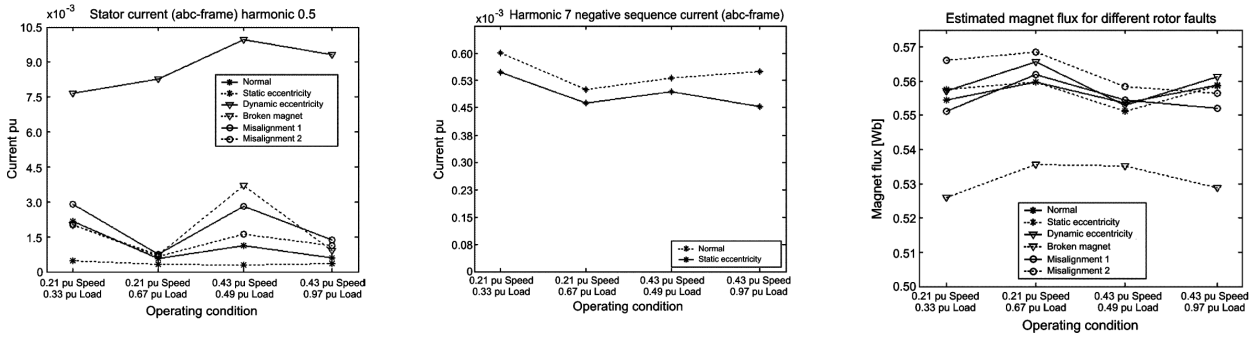

(a) Dynamic eccentricity detection (b) Static eccentricity detection (c) Broken magnets detection

Figure 1.3 Detecting broken magnets and eccentricity in PMSM [1]

For this method, a base line measurement for the machine need to be conducted first. During normal operation of the machine, the machine stator currents, phase voltages, and speed need to be monitored online continuously and the estimated flux is compared with the baseline measurements. A significant change in the fault harmonics of the stator current or a decrease in the estimated magnetic flux linkage can be used as a fault indicator to detect the fault type. The stator current spectrum was also used to separate between eccentricity and broken magnets in [28]. It was shown that the increase in the 0.75^{th} (i.e. $1 - 1/P$) harmonic was more observed in the case of eccentricity fault, while the increase in the 0.5^{th}

and the 0.25^{th} (i.e. $1-2/P$, and $1-3/P$) were more dominant in the case of broken magnets. The main drawback of this method is that it requires different indicators for fault detection, also the detection is based on the harmonics amplitudes. These harmonics are not always possible to notice, as they vary with the machine geometry and the operating conditions.

In [2] the induced voltages through search coils are used for monitoring the health status of PMSM, and for multi faults detection. A search coil was wound around each armature tooth, and the induced voltages were monitored during normal operations. The fundamental frequency component of the measured voltages were extracted from each coil and were used for fault detection and separation. Fig.1.4 shows a comparison of the field component of the measured voltages from each search coil under healthy and three different faults (static eccentricity, short circuit, and demagnetization faults).

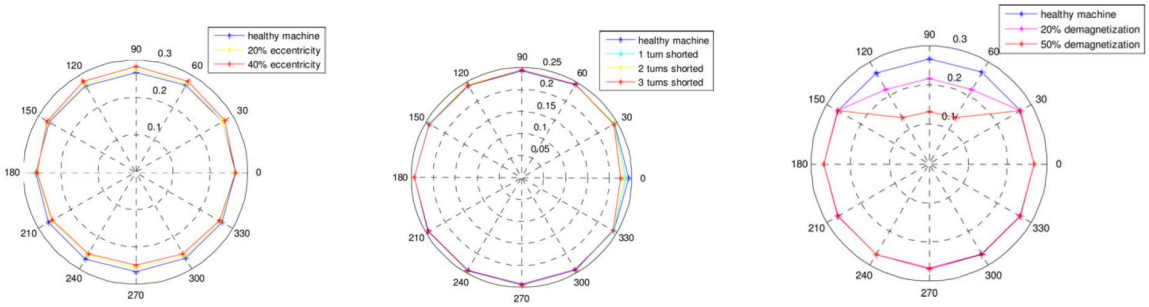

(a) Field component under static eccentricity (b) Field component under short circuit fault (c) Field component under demagnetization

Figure 1.4 Detecting multi faults in PMSM using search coils [2]

A change in the induced voltages can be used as a fault indicator in the machine. Based on the change, the fault type can be detected and the severity can be estimated. The method was able to separate between different faults, also it was capable of detecting the direction of eccentricity fault and the location of inter-turn short circuit fault. The main drawback for this method is the need for adding a search coil at every stator tooth during

the manufacturing of the machine, which may be expensive and not always possible.

The work in [13] presents a study of different time and frequency indicators, extracted from vibration signals, for detecting eccentricity and demagnetization faults in PMSM. It was shown that the combination of the skewness and the median frequency of the vibration signal, can be effective to decide whatever the machine is healthy or faulted, and to identify the type of the fault if existing. [3] studied vibration acceleration to detect and separate demagnetization from inter-turn short circuit faults using both mode shape and vibration frequency information. By analyzing the vibration signal using FFT, the change in the spectrum was used to detect and separate the two faults. Fig.1.5 shows a comparison of the vibration spectrum for PMSM under healthy, partial demagnetization, and inter-turn short circuit fault.

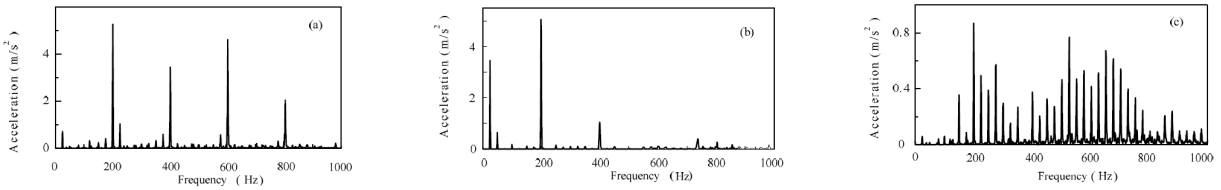

(a) Healthy machine (b) Partial demagnetization fault (c) Inter-turn short circuit fault

Figure 1.5 Spectrum of vibration signal under healthy and different faults [3]

In the case of demagnetization fault, vibration acceleration appears at low frequency region as shown in Fig.1.5b. In the case of short circuit fault, the vibration acceleration spectrum is spread over the frequency range as noticed in Fig.1.5c. This change in the spectrum can be used as an indicator to detect the presence and the type of the fault in PMSM. The main drawback of this approach is that using the vibration sensors is costly. Also, the operating condition and the placement of the motor affect the vibration signal, which might affect the clarity of the detection approach.

Hong *et al.* [20] proposed an offline method to separate eccentricity from demagnetization faults in PMSMs. This method is based on the change in the machine saturation, which is reflected in the incremental inductance curve. This method has the advantage of using the inverter signals for fault separation, which remove the necessity of adding a new hardware components. This method will be discussed in more details in chapter 4. There, it is also implemented to detect inter-turn short circuit fault, beside demagnetization and eccentricity faults. A classification algorithm is proposed to estimate the fault severity after determining the fault type.

The different methods for health monitoring in PMSMs, and the different fault diagnosis and prognosis methods are reviewed in [29]. So far, there is no single effective approach to separate between different faults. Most of the methods in the literature are only applicable under specific operating conditions, or can be applied to a specific type and topology of PMSMs.

1.4 Proposed Methods

This work proposes an algorithm for fault detection and identification in PMSMs based on the machine operating condition. The basic flow chart of the proposed algorithm is summarized in Fig.1.6

The proposed algorithm is based on the machine operating status. If the machine is at standstill, the incremental inductance method is proposed. In this method, the change of the incremental inductance curve, due to the change in the machine saturation, is used as a fault indicator. The direction of the shift in the incremental inductance curve peaks and the change of the peaks amplitude is used to detect the fault type and estimate the severity.

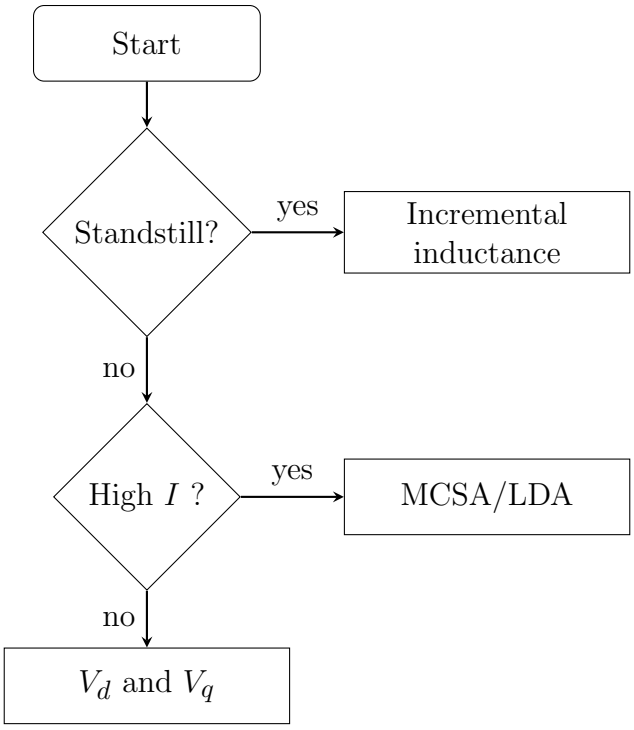

Figure 1.6 Proposed algorithm for fault detection and separation.

This method can also be applied as a last step in a manufacturing line to check the machine health status. If the motor is operating at steady state (i.e. constant speed and load), the change in the commanded voltages can be used for fault detection. The shift direction of the commanded voltages is used to detect the fault type, and the amount of the shift is used to estimate the fault severity. However, if the machine is operating at high torque, it is difficult to detect eccentricity faults using the commanded voltages approach. Here, the Motor Current or Voltage Signature Analysis (MCSA or MVCA) method with the Linear Discriminant Analysis (LDA) classification is proposed for fault detection and separation. This method is based on the variation in the amplitude of the stator current or voltage spectrum to generate the fault signatures. The main goal of the proposed algorithm is to avoid the need of any additional hardware components. The same signals that are used for the controller will be used for detecting the fault type and estimating its severity.

1.5 Organization

Chapter 2 presents the theoretical background and modeling for PMSM under healthy and faulted conditions. The model for the *dq* mathematical model for the machine will be used as the basic model for the proposed detection and estimation methods. An analytical approach is also discussed to calculate the magnetic flux distribution for both healthy and faulted conditions. Chapter 3 shows the geometry model and the parameters for the tested machines. It also shows how each fault was implemented in FEA and experimentally.

Chapter 4-6 are the core chapters for this work. They discuss the three proposed approaches for fault detection and estimation. Chapter 4 discusses the incremental inductance approach; how the incremental inductance curve is generated, the effects of each fault on the incremental inductance curve, and the proposed algorithm that uses it for fault detection. Chapter 5 talks about the MCSA and the MVSA using the LDA as a classification method. Chapter 6 discusses the shift in the commanded voltages approach. It shows how to use the commanded voltages as an easy and effective way to detect the machine health status and estimate the fault type and severity. Finally Chapter 7 brings the conclusions of this thesis.

Chapter 2

Theoretical Background

2.1 Healthy PMSM Model

A PMSM is a motor that uses permanent magnets, inserted in the rotor, to produce the airgap magnetic flux density. This gives these machines the advantages of having a high torque density and a wide operating range using the field weakening. PMSMs can be classified based on the direction of the field flux into two main categories [30]; if the flux direction is along the radius of the machine, the motor is called radial flux PMSM. If the flux direction is parallel to the rotor shaft, the motor is called axial flux PMSM. PMSMs can also be categorized based on the placement of the magnets in the rotor. If the magnets are positioned on the surface of the rotor outer surface, the motor is called Surface Mounted PMSM (SPMSM). If the magnets are positioned in the grooves of the outer edge of the rotor, the motor is called Surface Inset PMSM (SIPMSM). If the magnets are positioned in the center of the rotor laminations, the motor is called Interior PMSM (IPMSM). Fig.2.1 shows the three different configurations of PMSM based on the magnet placement.

For SPMSMs, all the magnets are in direct contact with the airgap, allowing them to have the maximum airgap flux density. However, this position for the magnet has lower structure robustness, which makes these machines suitable only for low speed operation. In the case of SIPMSMs the magnets are inserted inside the rotor allowing more mechanically robust structure, which makes these machines more suitable for high speed operation. IPMSMs

have the most mechanically robust structure, that is why these machines are used for very high speed applications, but they are harder to be manufactured. Generally in PMSM, two axes are defined in the rotor: a direct axis (*d-axis*) and a quadrature axis (*q-axis*). The *d-axis* is the rotor magnet axis and the path for the flux is through the magnet. The *q-axis* is 90 electrical degrees from the *d-axis*, the path of the flux is through the iron laminations only ($elect.\ deg. = \frac{mech.deg}{P}$). Fig.2.1 also shows the rotor *d-axis* and the *q-axis* for each rotor type.

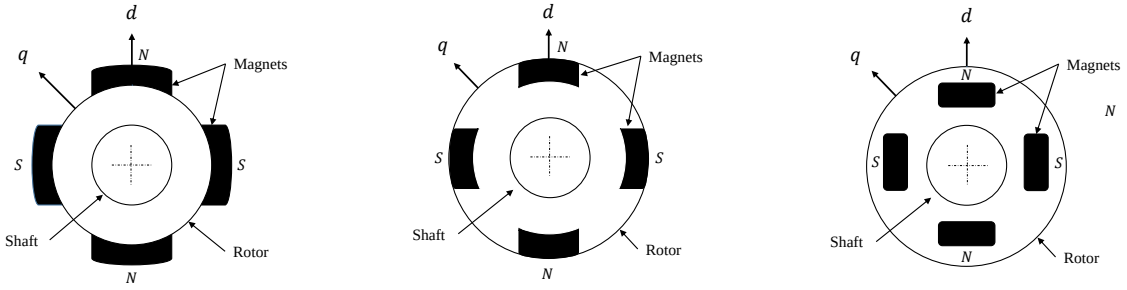

(a) Surface Mounted PMSM (b) Surface Inset PMSM (c) Interior PMSM

Figure 2.1 Comparison between the different configurations of PMSM based on the magnet placement

This work is focus on a balanced three phase IPMSMs with wye connected stator winding, this is one of the most common configuration for PMSMs. For a balanced three phase PMSM, the stator voltages, in the stator frame of reference (also known as the *abc* frame of reference), is given by (2.1)-(2.3):

$$v_a = R_a i_a + L_a \frac{d}{dt} i_a + M_{ab} \frac{d}{dt} i_b + M_{ac} \frac{d}{dt} i_c + \omega_e \lambda_a \tag{2.1}$$

$$v_b = R_b i_b + L_a b \frac{d}{dt} i_b + M_{ba} \frac{d}{dt} i_a + M_{bc} \frac{d}{dt} i_c + \omega_e \lambda_b \tag{2.2}$$

$$v_c = R_c i_c + L_c \frac{d}{dt} i_c + M_{ca} \frac{d}{dt} i_a + M_{cb} \frac{d}{dt} i_b + \omega_e \lambda_c \tag{2.3}$$

where v_a, v_b, and v_c are the three phase stator voltages, R_i is the stator resistance for phase i, L_i is the self inductance for phase i, M_{ij} is the mutual inductance between phase i and phase j, i_a, i_b, and i_c are the three phase stator currents, ω_e is the electrical speed, λ_a, λ_b, and λ_c represent the stator flux linkages generated by the rotor magnets. For a balanced three phase sinusoidal flux $\lambda_a = \lambda_{pm}\sin(\theta)$, $\lambda_b = \lambda_{pm}\sin(\theta - 120^0)$, and $\lambda_c = \lambda_{pm}\sin(\theta + 120^0)$.

To simplify the machine mathematical model, Park's transformation is used to transform the machine model from the stator three phase *abc* quantities to the rotor two phase *dq* quantities. This transformation is applied in two stages, first, the stator three phase quantities given by (2.1)-(2.3) is transformed to the equivalent stator space vector (α, β) components using Clark's transformation. Second, the (α, β) components are rotated to to be aligned with the rotor *dq* axes. Park's transformation combined both clack's transformation and the rotation matrix. The transformation is applied as follow:

$$x_{dq0} = P_a.x_{abc} \tag{2.4}$$

where x is the variable to be transformed, and P_a is Park's transformation matrix which is given by:

$$P_a = \begin{bmatrix} \cos(\theta) & \cos(\theta - \frac{2\pi}{3}) & \cos(\theta + \frac{2\pi}{3}) \\ \sin(\theta) & \sin(\theta - \frac{2\pi}{3}) & \sin(\theta + \frac{2\pi}{3}) \\ \frac{1}{2} & \frac{1}{2} & \frac{1}{2} \end{bmatrix} \tag{2.5}$$

where (θ) is the rotor position. It is important to note that the transformation is invertible, the inverse of Park's transformation matrix can be used to transform back the machine model

from the dq frame of reference to the abc frame of reference as follow:

$$x_{abc} = P_a^{-1}.x_{dq0} \tag{2.6}$$

where P_a^{-1} is the inverse of Park's transformation matrix at it is given as:

$$P_a^{-1} = \frac{2}{3}\begin{bmatrix} \cos(\theta) & \sin(\theta) & 1 \\ \cos(\theta - \frac{2\pi}{3}) & \sin(\theta - \frac{2\pi}{3}) & 1 \\ \cos(\theta + \frac{2\pi}{3}) & \sin(\theta + \frac{2\pi}{3}) & 1 \end{bmatrix} \tag{2.7}$$

By applying the transformation matrix (2.5) to (2.1)-(2.3), the PMSM model in the dq frame of reference is given by (2.11)-(2.10). The rotor position angle (θ) is either obtained using a rotor position sensor or it can be estimated. When the motor is rotating at a synchronous speed, the dq quantities become DC quantities in the rotor frame of reference. The equivalent circuit model is shown in Fig. 2.2.

$$\begin{aligned} v_d &= r_s i_d + L_d \frac{di_d}{dt} - \omega_e L_q i_q \\ &= r_s i_d + \frac{d\lambda_d}{dt} - \omega_e \lambda_q \end{aligned} \tag{2.8}$$

$$\begin{aligned} v_q &= r_s i_q + L_q \frac{di_q}{dt} + \omega_e L_d i_d + \omega_e \lambda_{pm} \\ &= r_s i_q + \frac{d\lambda_q}{dt} + \omega_e \lambda_d \end{aligned} \tag{2.9}$$

$$\lambda_d = L_d i_d + \lambda_{pm} \tag{2.10}$$

where v_d and v_q are the direct and quadrature axis voltages, i_d and i_q are the direct and quadrature axis currents, r_s is the stator resistance, λ_d and λ_q are the direct and quadrature linkage fluxes, L_d and L_q are the direct and quadrature inductances, and λ_{pm} is the magnet

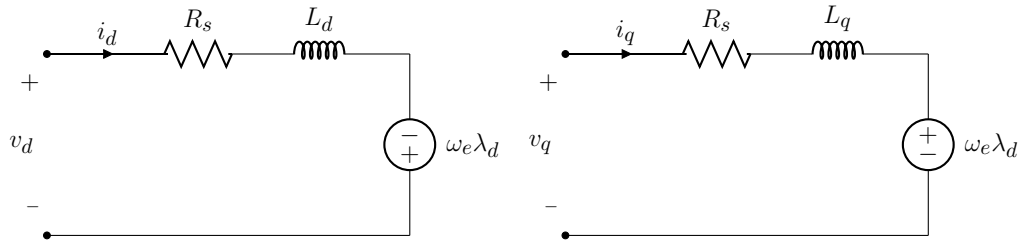

(a) d-axis equivalent circuit (b) q-axis equivalent circuit

Figure 2.2 The equivalent circuit model of PMSM in the dq frame of reference

flux linkage. Under steady state operation (the motor is rotating at a constant speed and torque), the dq quantities become DC quantities. In this case the time varying components $\frac{di_d}{dt}$ and $\frac{di_q}{dt}$ will be equal to zero. In this case the mathematical model for PMSM in the dq frame of reference at steady state operation is as follows:

$$v_d = r_s i_d - \omega_e L_q i_q \tag{2.11}$$

$$v_q = r_s i_q + \omega_e \lambda_d \tag{2.12}$$

The torque is produced from the interaction between the flux linkages and and the current in each axis as follow:

$$T = \frac{3P}{2}(\lambda_d i_q - \lambda_q i_d) = \frac{3P}{2}(\lambda_{pm} i_q + (L_d - Lq) i_d i_q) \tag{2.13}$$

A better representation of the machine model transformation is shown in Fig.2.3. In this orientation, the flux linkage due to the magnets (λ_{pm}) is aligned with the d axis. The q axis is 90 electrical degree counter clockwise from the d axis. The torque is produced mainly by the q axis current, since that it is perpendicular to the magnet flux (λ_{pm}), while i_d is used to control the amount of the flux. By controlling the current magnitude (I_s) and the current

angle (δ), the generated torque can be controlled.

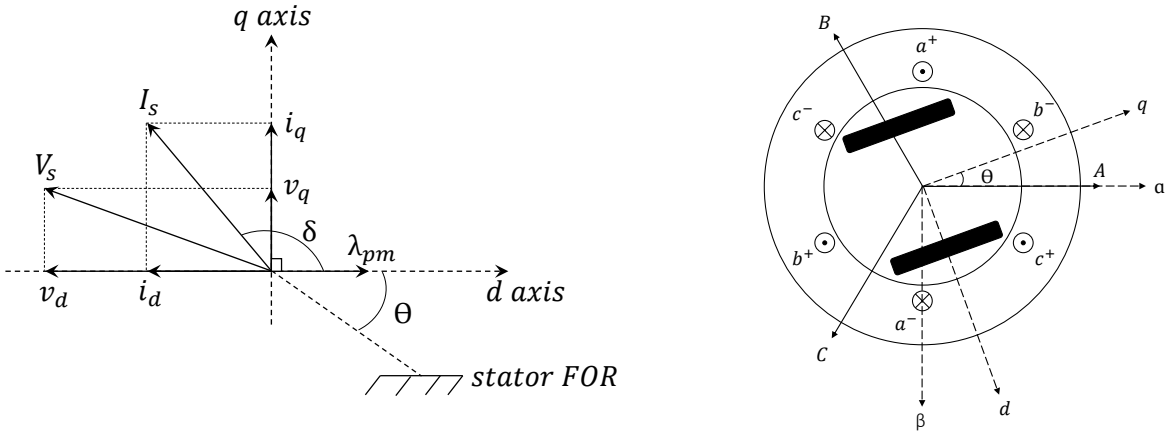

(a) Space vector diagram for PMSM

(b) Three phase winding transformation

Figure 2.3 Simplified model for PMSM transformation

It is important to note that this model assumes that the stator resistance, and self inductance for all three phases are the same (*i.e.* $R_a = R_b = R_c = r_s$, $L_a = L_b = L_c$). This model also does not account for iron losses, nor for the self and cross saturation between the stator three phases. However, it still represents the machine basic characteristics and performance accurately. It is important to note that the proposed methods are also applicable for all the different types of PMSM. Therefore, this model will be used as the reference machine model for this work.

To provide a better understanding of the machine model, and the change in the machine parameters under different faults compared to the healthy case, an analytical approach for calculating the motor magnetic flux density is required. Zhu *et al.* in [31–34] proposed an analytical approach to calculate the airgap magnetic flux density, for a surface mount Brushless Permanent Magnet DC motors. Based on their analysis, the total magnetic flux density can be calculated by adding the magnetic flux density from the magnets ($B_{rm}(r, \theta)$) [31] to the magnetic flux density generated from the winding ($B_{rw}(r, \theta)$) [32], taking the

slotting effect ($\tilde{\lambda}(r,\theta)$) [33] into account as follow:

$$B_r(r,\theta) = (B_{rm}(r,\theta) + B_{rw}(r,\theta)).\tilde{\lambda}(r,\theta) \tag{2.14}$$

Only the airgap magnetic flux density due to the magnets is of interest for this work, since that it is directly related to the motor geometry and it will be affected directly by the presence of faults in the machine. The radial component of the magnets flux density at the stator inner surface ($r = Rs$) (without taking into account the slots opening or the magnetic flux density from the stator winding) is given by (2.15) when $np = 1$

$$\begin{aligned} B_{rm}(\theta) = \sum_{n=1,3,5,\ldots}^{\infty} 2.\frac{\mu_0 M_n}{\mu_r}.\frac{np}{(np)^2-1}\left(\frac{R_s}{R_m}\right)^{np-1} . \\ \left[\frac{(np-1)R_m^{2np} + 2R_r^{np+1}R_m^{np-1} - (np+1)R_r^{2np}}{\frac{\mu_r+1}{\mu_r}[R_s^{2np} - R_m^{2np}] - \frac{\mu_r-1}{\mu_r}[R_m^{2np} - R_s^{2np}(\frac{R_r}{R_m})^{2np}]}\right] . \cos(np\theta) \end{aligned} \tag{2.15}$$

For $np \neq 1$ the radial component of the magnetic flux density is given by (2.16)

$$B_{rm}(\theta) = \frac{\mu_0 M_1}{\mu_r}.\left[\frac{\left(\frac{R_m}{R_s}\right)^2 - \left(\frac{R_r}{R_s}\right)^2 + \left(\frac{R_r}{R_s}\right)^2 ln\left(\frac{R_m}{R_r}\right)^2}{\frac{\mu_r+1}{\mu_r}\left[1-\left(\frac{R_r}{R_s}\right)^2\right] - \frac{\mu_r-1}{\mu_r}\left[\left(\frac{R_m}{R_s}\right)^2 - \left(\frac{R_r}{R_m}\right)^2\right]}\right] .cos(\theta) \tag{2.16}$$

where μ_0 is the permeability of free space ($\mu_0 = 4\pi * 10^{-7}$), μ_r is the relative coil permeability, $R_r = R_s - g - h_m$, $R_m = R_s - g$, R_s is the inner stator radius, g is the airgap length, h_m

is the thickness of the magnet, and M_n is given by:

$$M_n = 2\left(\frac{\beta_r}{\mu_0}\right)\alpha_p \frac{sin\left(\frac{n\pi\alpha_p}{2}\right)}{\left(\frac{n\pi\alpha_p}{2}\right)} \tag{2.17}$$

where β_r is the magnet remanence, and α_p is the pole arc to pole pitch ratio. The airgap magnetic flux, for each phase can be calculated by integrating numerically the total magnetic flux density over the entire area as:

$$\lambda = \int_0^{2\pi}\int_0^{r} B_r(r,\theta) r dr d\theta \tag{2.18}$$

Fig.2.4 shows a comparison of the magnetic flux density calculated analytically (without taking the slotting effect into account) and using Finite Element Analysis (FEA) for a three phase concentrated winding IPMSM.

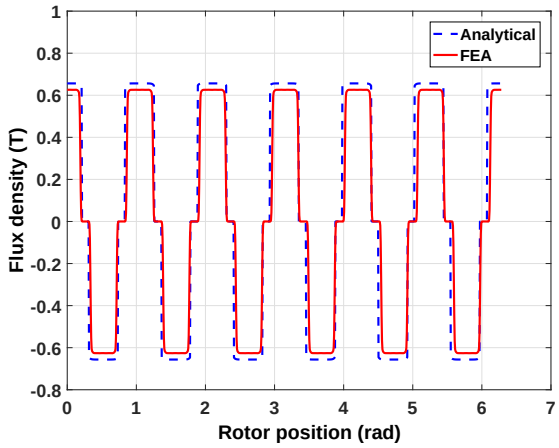

Figure 2.4 A comparison of the flux density between FEA simulation and analytical calculation for the concentrated winding machine

The difference between analytical calculations and FEA is due to the fact that the analytical calculations proposed in [31] were applicable to a surface mount PM Brushless DC machine, while the tested machine is an IPMSM.

2.2 PMSM Under Eccentricity Faults

Eccentricity is a condition of an uneven airgap between the stator and the rotor. This leads to an asymmetric airgap flux distribution, which creates an unbalanced magnetic pull causing vibrations, noise, and possibly wear of the bearings. By time the unbalanced magnetic force may further increase and cause the rotor and the stator to rub.

Eccentricity faults can be classified into three main types: static eccentricity, dynamic eccentricity, and mixed eccentricity. In the case of static eccentricity, the center of the stator geometric axis is different than that of the rotor and the rotation axis. This could be caused by an incorrect rotor stator aligning during the assembly of the machine or due to the different mechanical and electrical stresses applied to the machine. In the case of dynamic eccentricity, the center of the rotor geometric axis is different than that of the stator and the rotation axis. The main reasons for dynamic eccentricity include: a bend in the machine shaft, bearing wear, mechanical and thermal stresses applied to the shaft, and mechanical resonance at critical speed. In the case of mixed eccentricity, the rotation axis is different than the stator and the rotor geometric axes. This type combines both static and dynamic eccentricities. Fig.2.5 shows a comparison of the cross section geometry between healthy machine and the three different types of eccentricity faults. Only static eccentricity is discussed and tested for this work because it is the most common type of eccentricity.

In the case of static eccentricity, the airgap length (g) in (2.15) and (2.16) will no longer be symmetric, it depends on the rotor position. Based on Fig.2.6 and following [35], a general formula for the airgap, in the case of static eccentricity, can be derived as follows:

$$R_s.\cos(\theta') = \varepsilon\cos(\phi) + (R_m + g_{ecc})\cos(\theta) \tag{2.19}$$

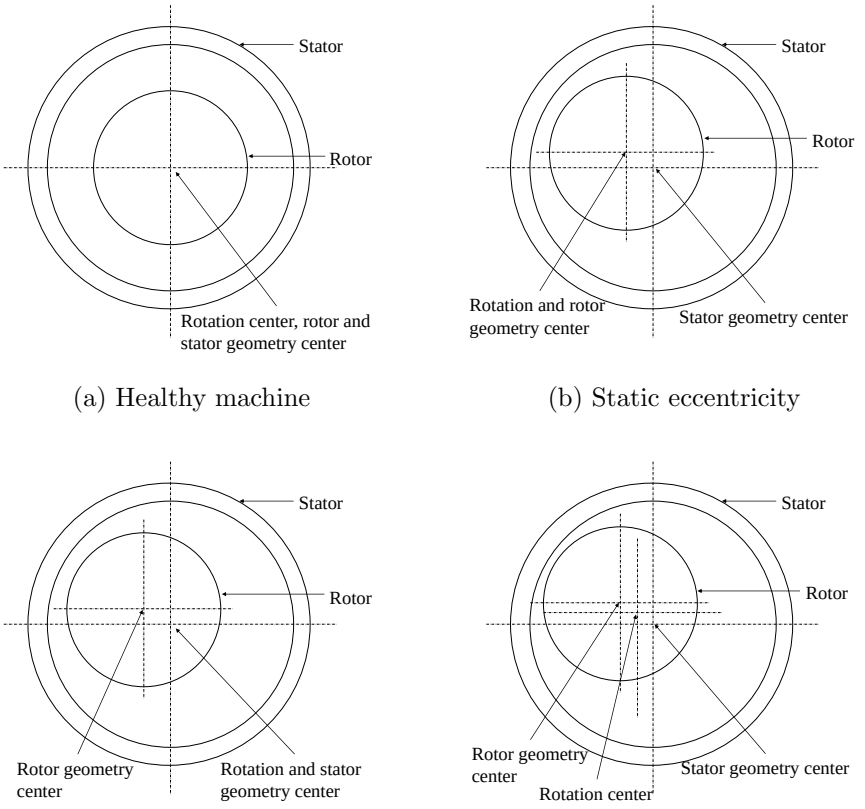

(a) Healthy machine

(b) Static eccentricity

(c) Dynamic eccentricity

(d) Mixed eccentricity

Figure 2.5 Comparison between healthy and eccentricity machine

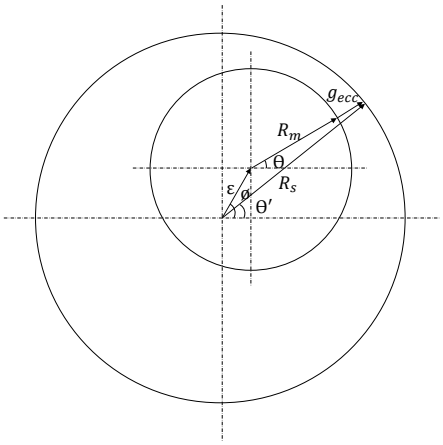

Figure 2.6 Analytical approach to calculate eccentricity

$$R_s.\sin(\theta') = \varepsilon\sin(\phi) + (R_m + g_{ecc})\sin(\theta) \tag{2.20}$$

Taking the square of (2.19) and (2.20), and adding them together is given as:

$$R_s^2 = \varepsilon^2 + (R_m + g_{ecc})^2 + 2\varepsilon(R_m + g_{ecc})\cos(\phi - \theta) \tag{2.21}$$

$$\Rightarrow g_{ecc} = -\varepsilon\cos(\phi - \theta) \pm \sqrt{R_s^2 - \varepsilon^2\sin(\phi - \theta)^2} - R_m \tag{2.22}$$

Since $R_s \gg \varepsilon$, the airgap in case of static eccentricity is given by:

$$g_{ecc} = (R_s - R_m) - \varepsilon\cos(\phi - \theta) = g - \varepsilon\cos(\phi - \theta) \tag{2.23}$$

Fig.2.7 shows a comparison of the airgap between healthy machine and a machine with eccentricity fault.

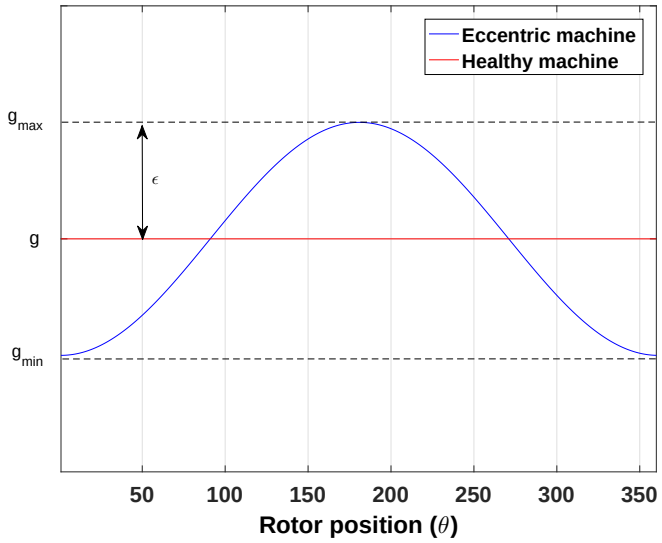

Figure 2.7 Airgap under healthy and eccentricity fault

The severity of eccentricity fault is expressed as following:

$$ECC = \frac{\epsilon}{g} \times 100\% \tag{2.24}$$

The change in the analytical calculation for the magnetic flux density under eccentricity fault can be studied by replacing the airgap in (2.15) & (2.16) the new airgap g_{ecc}.

It is important to detect eccentricity faults while it is still in the early stage. With time, the unbalanced magnetic force between the rotor and the stator may further increase causing the rotor and the stator to rub, which will cause a severe damage to the machine. [36] studied the effect of rotor eccentricity on the Unbalanced Magnetic Pull (UMP) for large Synchronous Machines with Permanent Magnets Synchronous Machines and Winding Fields Synchronous Machines. According to [37], any eccentricity less than 10% can be neglected, and any eccentricity higher than 60% requires immediate repair to prevent any rubbing between the stator and the rotor, which will damage the machine.

Static eccentricity fault causes a change in the airgap length, which cases a change in the reluctance. Changing the reluctance causes a change in the total flux linkages around the airgap causing a change in the machine saturation level. The machine flux linkages and the airgap length are related by the machine reluctance as follows:

$$\mathcal{R} = \frac{g}{\mu_0 A_g} \tag{2.25}$$

$$\phi = \frac{\mathcal{F}}{\mathcal{R}} \tag{2.26}$$

where A_g is the airgap area, $\mathcal{R}$ is the reluctance, $\mathcal{F}$ is the magnetomotive force, and ϕ is the magnetic flux. The area with lower airgap will have lower reluctance and therefore higher

flux concentration. This causes higher saturation in that region. On the other hand, the area with higher airgap length will have higher reluctance and therefore lower flux concentration. This causes lower saturation in the higher airap region. In the case of ideal machine, the amount of the increase in the flux linkages will be equal to the amount of the decrease in flux linkage, which average the total flux linkages in the machine. However, due to the non linearity and the saturation in the machine, the increase in the magnetic flux at the smallest airgap region will be higher than the decrease of the magnetic flux in the largest airgap region. This increases the total magnetic flux causing the machine to saturate faster in the case of eccentricity fault compared to the healthy case. This effect can be explained using the flux vs Magnetomotive Force (MMF) curve of the machine. Fig.2.8 shows the flux vs MMF curve under healthy case and eccentricity fault.

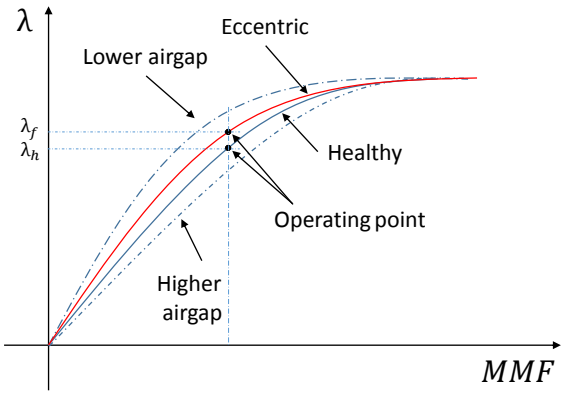

Figure 2.8 Flux vs MMF under healthy and eccentric machine

The area with the lower airgap region will cause an increase in the slope of the curve, while the area with higher airgap will decrease the slope of the curve. Due to the saturation and the nonlinearity in the machine, the average of the two curves will be higher compared to the healthy machine curve. Therefore, the machine under eccentricity fault saturates faster, and at any operating point, the total flux linkages in the machine will be higher compared

to the healthy case. Fig.2.9b shows the FEA simulation results for the maximum of the magnetic flux density measured at the center of each pole pair for the FSCW machine (the machine parameters is in Table3.1) under healthy and two severity levels of static eccentricity fault (40% and 80%). Fig.2.9c shows the vector summation of the x and y component of the magnetic flux for all the pole pairs under healthy and four severities of eccentricity fault.

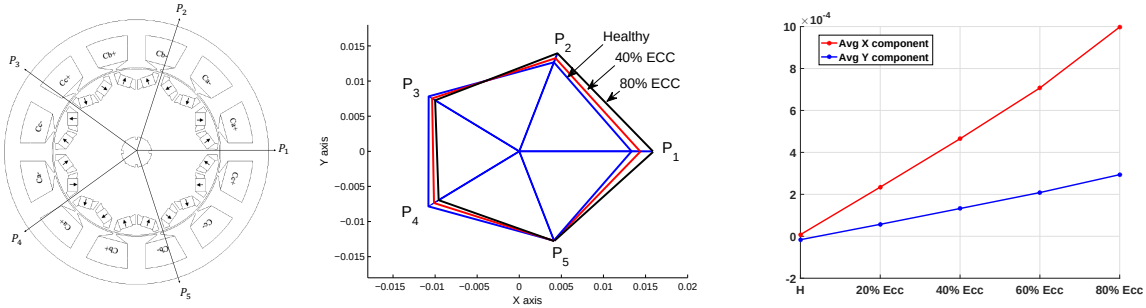

(a) Tested machine (b) Maximum of the magnetic flux (c) Average of the X and Y components

Figure 2.9 Comparison of the magnetic flux density between a healthy machine and two severities of eccentricity fault

It can be noted that for healthy machine, the vector summation in the x and y components equal to zero. This is expected since that the machine is healthy and the distribution of the airgap length and the magnetic flux is uniform around the machine. However, for eccentric machine, the sum will no longer be equal to zero. It will be higher compared to the healthy machine, and the amount of the increase is proportional to the severity of the fault. As the fault severity increases, the total summation will increase causing more flux linkages. It can also be noticed that the main increase is in the x axis because the shift of the rotor and the rotation axis was in the positive x direction.

2.3 PMSM Under Demagnetization Faults

Demagnetization is also a common rotor fault in PM machines. The demagnetized magnets will cause asymmetric distribution of the flux density, which causes a reduction in the total permeance flux in the machine. This reduces the average torque, increase the torque ripple and reduce the motor efficiency. The main factor that cause demagnetization faults is turn-to-turn short circuit fault, as the severity of short circuit fault increases, a higher current will flow in the shorted turns, this current will weaken the magnets and by time will lead to demagnetizing the rotor magnets. Other factors that might cause demagnetization fault include: the aging of the magnet, high temperature, and operation under strong field weakening.

Demagnetization faults can be classified into two main types: uniform demagnetization and partial demagnetization. In the case of uniform demagnetization, all the magnets in the rotor are demagnetized. In the case of partial demagnetization, only a specific number of magnets are demagnetized.

In the case of partial demagnetization fault, a nonuniform magnetic flux density generates in the airgap, which causes a disturbance to the magnetic flux in the motor and reduction in the total magnetic flux density. The effect of demagnetization can be noted whenever the demagnetized magnets interact with the stator slots. This can be clearly observed in the case of single layer fractional slots concentrated winding machines. Fig.2.10 shows a comparison of the magnetic flux linkages of phase A over one mechanical cycle, under healthy and demagnetization fault (Mag_1 of the FSCW machine was fully demagnetized).

Demagnetization faults affects the saturation of the machine, but in an opposite way compared to eccentricity faults. The demagnetized magnets will cause a reduction in the

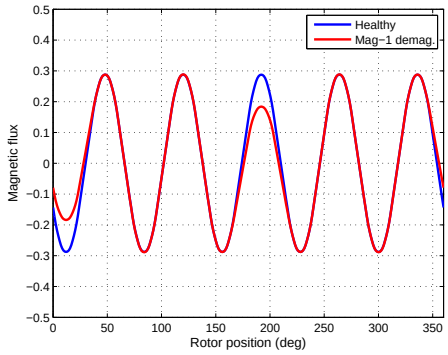

Figure 2.10 Comparison of the magnetic flux under healthy and demagnetization fault

total magnetic flux linkages, which reduces the total saturation of the machine. In this case, the machine requires more currents in order to have the same saturation as the healthy machine.

For analytical calculations, the same analytical approach that was used for healthy macine can also be used to analyze the effect of demagnetization faults. In the case of demagnetization fault, the remanence flux density (β_r) of the demagnetized magnets in (2.17) will change according to the severity and the position of the demagnetized magnets are determined using the following equation:

$$\beta_{rdem} = \beta_r \times (1 - \beta_{rdemag}) \tag{2.27}$$

where β_{rdemag} is the percentage of demagnetization. Fig.2.11 shows the flux density distribution for healthy, 66% eccentricity and one magnet demagnetized, using FEA simulation compared to the analytical calculations. The change in the magnetic flux density under eccentricity and demagnetization faults can be observed using both the analytical calculations and using FEA simulations. In the case of eccentricity fault, the decrease in the airgap length will cause an local increase in the magnetic flux density and therefore, increase the total flux of the machine. For demagnetization fault, the demagnetized magnets will cause

a reduction in the magnetic flux density which will reduce the total generated flux.

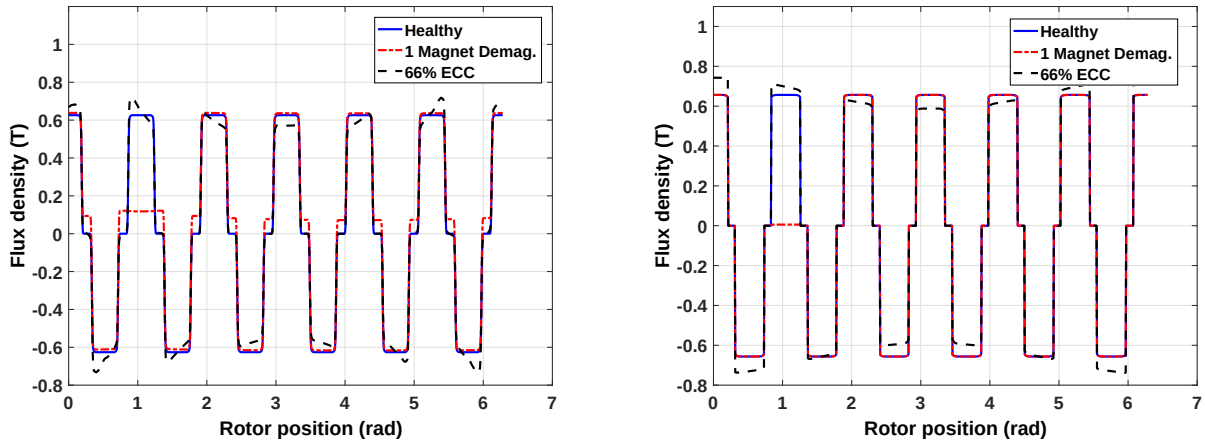

(a) FEA simulation (b) Analytical calculations

Figure 2.11 Comparison between FEA simulation and Analytical calculations or healthy, one magnet demagnetized and 66% eccentricity

2.4 PMSM Under Turn-to-Turn Short Circuit Fault

Of the many possible types of stator winding faults, turn-to-turn short circuit fault consider one of the most common. This fault can be caused due to mechanical, electrical and thermal stress applied to the stator winding. These stresses may lead to an insulation breakdown of the coil conductor, which leads to shorting some of the turns. In the case of turn-to-turn short circuit fault, the shorted turns create an extra high current path that is magnetically and electrically coupled with the winding current and the flux path. This current will heat the shorted turns, causing further insulation damage and may expand to short the nearby windings. Therefore, detecting turn-to-turn fault at an early stage is important to protect the machine and the winding from any further damage. Fig.2.12 shows a series connected three phase winding with turn-to-turn short circuit fault in phase A. The fault is modeled by a small resistance R_{f} connected in parallel across the shorted turns. Two factors defines

the severity of turn-to-turn short circuit fault: the number of shorted turns, and the shorted resistance.

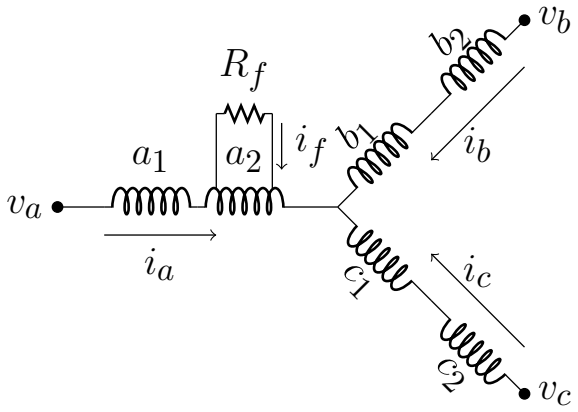

Figure 2.12 Series winding with shorted turns.

Following [38], in the case of turn-to-turn short circuit fault, a high short circuit current will flow in the shorted turns adding a new induced voltage related to the short circuit fault. The mathematical model for a machine under turn-to-turn short circuit fault can be described as follows:

$$\begin{bmatrix} v_{ah} \\ v_{af} \\ v_b \\ v_c \end{bmatrix} = \begin{bmatrix} r_{ah} & 0 & 0 & 0 \\ 0 & r_f & 0 & 0 \\ 0 & 0 & r_s & 0 \\ 0 & 0 & 0 & r_s \end{bmatrix} \begin{bmatrix} i_a \\ i_a - i_f \\ i_b \\ i_c \end{bmatrix} + \begin{bmatrix} e_{ah} \\ e_{af} \\ e_b \\ e_c \end{bmatrix} + \begin{bmatrix} L_{a_h} & M_{a_h a_f} & M_{a_h b} & M_{a_h c} \\ M_{a_h a_f} & L_{a_f} & M_{a_f b} & M_{a_f c} \\ M_{a_h b} & M_{a_f b} & L_b & M_{bc} \\ M_{a_h c} & M_{a_f c} & M_{bc} & L_c \end{bmatrix} \frac{d}{dt} \begin{bmatrix} i_a \\ i_a - i_f \\ i_b \\ i_c \end{bmatrix} \tag{2.28}$$

where v_{ah} and v_{af} are the voltages across the healthy and faulty coils respectively, r_{ah} and r_{af} are the resistance for healthy and faulty section of the coil, i_f is the short circuit current, e_{ah} and e_f are the induced emf voltages across the healthy and faulted coils, e_b and e_c are the induced emf voltages of phase B and phase C respectively. Park's transformation can also be used to transform the model of a PMSM machine under turn-to-turn short circuit

fault from the *abc* frame of reference to the *dq* frame of reference. For concentrated winding machines, the mutual inductance between the shorted turns and the other two phases can be neglected, only the mutual inductance between the shorted turns and the healthy turns in the same phase need to be considered. In this case, the model for PMSM machine under turn-to-turn short circuit fault in the *dq* frame of reference is given by (2.29)-(2.34)

$$v_{dsh} = v_d + v_{df} \tag{2.29}$$

$$v_{qsh} = v_q + v_{qf} \tag{2.30}$$

where

$$v_d = i_d r_s + L_d \frac{di_d}{d_t} - \omega_e L_q i_q \tag{2.31}$$

$$v_{df} = \frac{2}{3}\left(r_f \cos(\theta) i_f + (M_{a_h a_f} + L_{af}) \cos(\theta) \frac{di_f}{dt} - \omega_e (M_{a_h a_f} + L_{a_f}) i_f \sin(\theta)\right) \tag{2.32}$$

$$v_q = i_q r_s + L_q \frac{di_q}{d_t} + \omega_e (L_d i_d + \lambda_{pm}) \tag{2.33}$$

$$v_{qf} = \frac{2}{3}\left(r_f \sin(\theta) i_f + (M_{a_h a_f} + L_{af}) \sin(\theta) \frac{di_f}{dt} + \omega_e (M_{a_h a_f} + L_{a_f}) i_f \cos(\theta)\right) \tag{2.34}$$

It can be noted that the machine model under short circuit fault contains two main components. The first component is similar to the healthy model, the second component is related to the short circuit fault. The fault related component depends on the severity of the short circuit fault (i.e. number of shorted turns and the shorted resistance) and the machine operating condition (i.e. operating torque and speed). Similar to the healthy machine, at steady state operation, the time varying components in (2.29)-(2.34) will be equal to zero.

In this case, the component related to short circuit fault will be given by:

$$v_{df} = \frac{2}{3}\Big(r_f \cos(\theta) i_f - \omega_e (M_{a_h a_f} + L_{a_f}) i_f \sin(\theta)\Big) \tag{2.35}$$

$$v_{qf} = \frac{2}{3}\Big(r_f \sin(\theta) i_f + \omega_e (M_{a_h a_f} + L_{a_f}) i_f \cos(\theta)\Big) \tag{2.36}$$

Chapter 3

Experimental and Simulation Setup

3.1 Augmented Finite Element Analysis Simulations

Finite Element Analysis (FEA) is a powerful and flexible technique for solving ordinary and partial differential equation using numerical methods. In the case of electromagnetic analysis, FEA is used to calculate the magnetic field in electrical machine by solving Maxwell differential equations. The behaviour of the machine is determined by the distribution of the magnetic field and current density, which is coupled with an external circuit that is used to control the stator currents. In FEA simulations, the geometry is dividing into a finite number of small sections called elements, which makes a grid called mesh. The accuracy of the solution depends on the element topology, the way they were assigned, and on the size of each element. The elements are assigned to the geometry according to the variation of the magnetic potential; such that an area with a high variation in the magnetic vector potential, need a higher number of elements (i.e. finer mesh) compared to an area with a little or no magnetic vector potential variation. The result is a system of a nonlinear equations, which is solved iteratively till it converges to a unique solution.

FEA simulation is used for machine analysis and design; it is used to analyze different machine topologies with any materials, windings distribution, and slot/pole combinations. The main advantage of FEA is the ability to calculate the motor inductances, flux linkages, forces and the electromagnetic torque for the machine accurately without the need to an

analytical approach. FEA can also be used to study the effect of faults on electrical machines and shows how the machine parameters and performance changes according to each fault. Therefore, for this work FEA simulations were performed first in order to understand the effect of each fault, and then experimental tests were carried out to validate the simulation results.

In this work, three PMSMs were tested under healthy and faulted conditions. All the tested machines were a 3 phase Y-connected, with different slot/pole combinations, winding distribution and different input and output power. The tested motors were as follows: a 12-pole distributed winding machine, a 16-pole concentrated winding machine and a 10-pole Fractional Slot Concentrated Winding (FSCW) machine. Fig.3.1 shows the cross sections for the tested machines, and Table 3.1 shows their parameters.

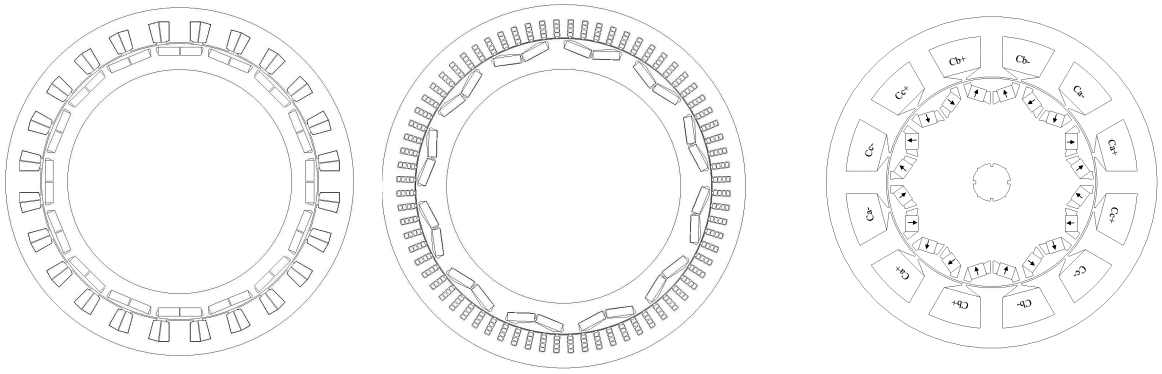

(a) Concentrated winding machine (b) Distributed winding machine (c) FSCW machine

Figure 3.1 Geometry cross section for the tested machines

Table 3.1 Parameters for the tested machines

	Concentrated winding machine	Distribution winding machine	2/5 SPP FSCW machine
Number of phases	3 phase	3 phase	3 phase
Maximum current	300A	300A	25A
Maximum torque	310N.m	315N.m	50N.m
Number of slots	24	48	12
Number of poles	16	12	10
Turns per phase	46	8	150

3.2 Faults Implementation in FEA

3.2.1 Implementing Eccentricity Fault

To apply static eccentricity faults in FEA, the axis of the stator geometry should be different than the rotor geometry and the rotational axis center. Therefore, a separate coordinate system was assigned to the stator geometry that is different than the rotor and the rotational coordinate system; by changing the center of stator coordinate system, only the stator geometry shifts while the rotor and the rotation axis stay the same. This allows controlling the direction and the degree of eccentricity fault, and the severity of the fault was varied based on the machine airgap according to (2.24).

3.2.2 Implementing Demagnetization Fault

To apply partial demagnetization, the material of the chosen demagnetized magnets was replaced with a material that has the same electrical and mechanical characteristics but with different permeance flux density compared to the healthy magnets. The permeance is changing based on the percentage of demagnetization fault (2.27). For a demagnetization fault with a 100% demagnetization, the magnet remanence flux was changed to $0T$. For

this work a partial demagnetization with a percentage of 100% was tested. To change the severity of the fault, the number of the demagnetized magnets was varied.

3.2.3 Implementing Turn-to-turn Short Circuit Fault

The way turn-to-turn short circuit fault was applied in FEA simulations depends on the machine stator winding topology. For the distributed winding machine, two end turns were shorted through a small resistance. Based on the machine winding diagram, the corresponding coils were assigned to a faulted coil (C_f), which was shorted through a resistance (R_f) in the control circuit, while the healthy coils were assigned to the healthy coil (C_a) as shown in Fig.3.2. To vary the severity of short circuit fault another two end turns were shorted. The short resistance for each case was varied as well to study the effect of the short resistance on the behaviour of short circuit fault.

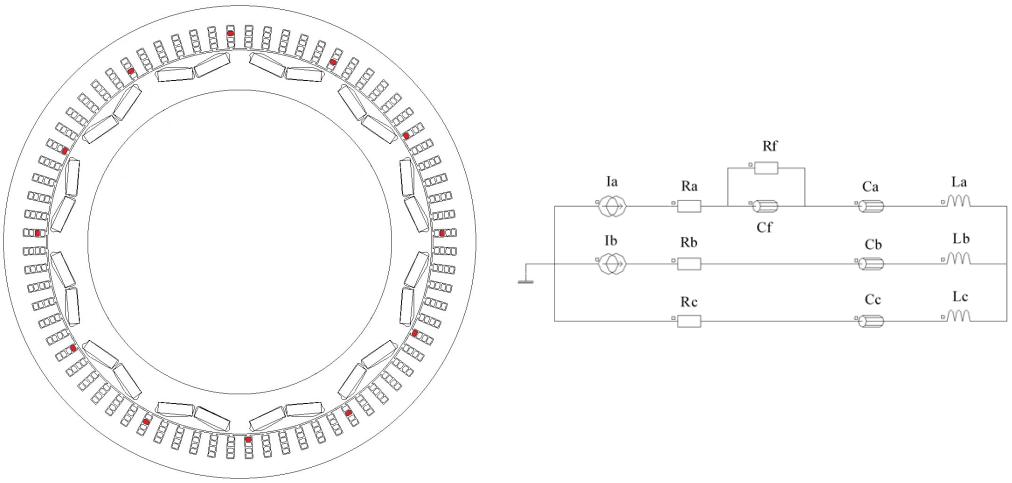

(a) Distributed winding machine with 12% short circuit fault

(b) Control circuit with short circuit fault

Figure 3.2 Implementing short circuit fault in FEA for the distributed winding machine

For concentrated windings machines, a new faulted regions related to the shorted turns needs to be added in the faulted slots. The number of shorted turns need to be assigned to

the new regions and subtracted from the healthy one. For the control circuit, the shorted turns were assigned to a faulted coil (C_f), and a small resistance was connected in parallel to the shorted coil to represent short circuit fault. Fig.3.3 shows the modified cross section and the control circuit of the concentrated winding machine with turn-to-turn short circuit fault. To vary the severity of the fault, the number of shorted turns were varied and also the short resistance was varied as well.

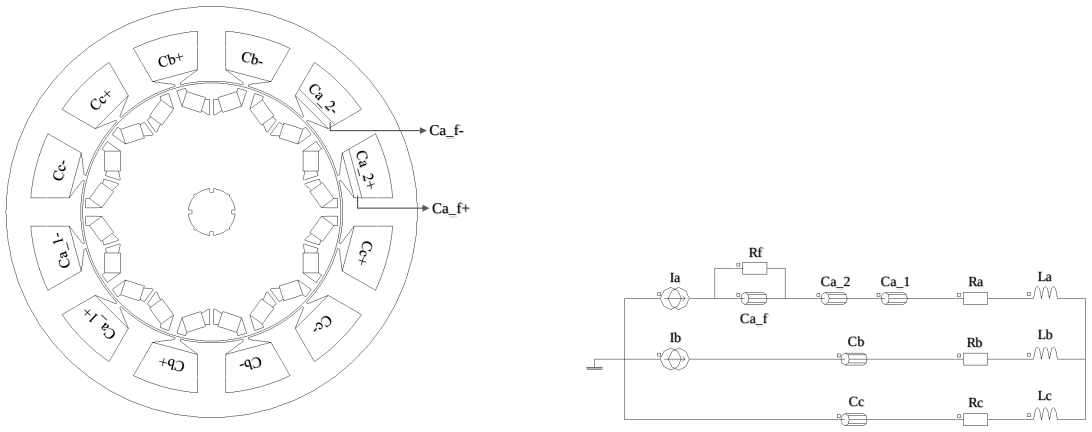

(a) Modified cross section area for the tested machine with a short circuit fault

(b) Modified control circuit with extra coil to represent a short circuit fault

Figure 3.3 Implementing short circuit fault in FEA for the FCSW machine

3.3 Experimental Setup

Experimental tests were performed on the three tested machines to validate the simulation results. National Instrument (NI) Real Time Lab-VIEW (RTLV), was used to operate and control the tested machines. This real-time system consists of two desktop computers: one is used as host and the other as the target. The controller was developed first in the host computer then deployed to the target where it is run by the target computers processor.

The host computer was used to monitor the feedback data from the target and applies the changes to the controller parameters.

The Field Oriented Control (FOC) was used as a control scheme to operate the tested machines. The main objective of this controller is to control the direct and quadrature currents (I_d and I_q) using the rotor position (θ) to achieve the desired torque. I_d is used to control the amount of the flux linkage, while I_q is the main torque producing component. Fig.3.4 shows the basic block diagram for the FOC. In this controller, first the three phase stator currents are measured. These measured currents are fed into Park's transformation that output the current in the dq frame of reference. The measured dq currents are contrasted with the commanded dq currents. The output of the PI controllers are the commanded voltages (v_d^* and v_q^*). These voltages are applied to the inverse Park transformation to generate the three phase machine voltages in the abc frame of reference. The three phase voltages are fed to the Space Vector Pulse Width Modulation that control the inverter signals, that used to control the tested machine.

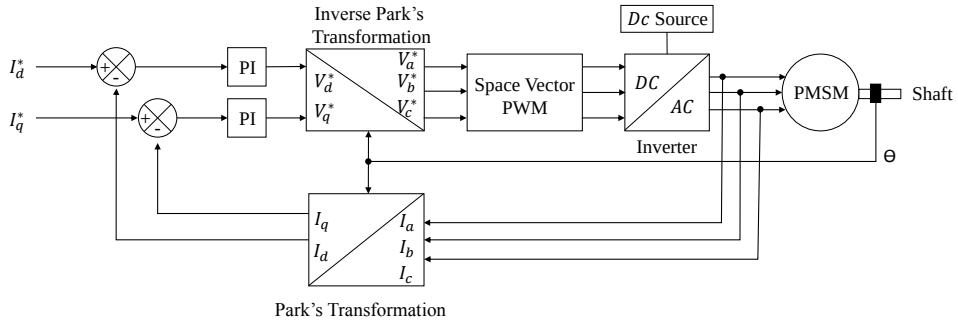

Figure 3.4 Block diagram of the Field Oriented Controller for PMSMs

The main advantages of using the FOC include fast dynamic response, high efficiency, and the ability to control the torque over a wide operating speed using field weakening. For this type of controller, the measured currents and the commanded voltages are always

available. Therefore, signatures generated from these signals will be used for fault detection and estimation.

In order to obtain a model that is a realistic representation of the actual machine, the main machine parameters need to be calculated accurately. The machine parameters can be determined using a process known as motor characterization. The main parameters that need to be estimated in PMSMs are the flux linkages. In this process the machine terminal voltages, currents and the rotor position are used to calculate the machine parameters for different operating conditions. Using the method proposed in [39, 40] the characterization method can be summarized as follows:

- The open circuit voltages are used to align the rotor position sensor with the rotor d and q flux axis.
- While the machine is rotating at a constant speed (usually lower than the base speed), the stator current I_s is varied from 0 to the base current (I_{smax}), and for every current step the current angle δ is varied from 90 to 180 degrees.
- The commanded current magnitude I_s and the current angle δ control the amount of the flux and torque in the machine.
- Park's transformation, with the rotor position, is applied to the measured three phase currents and the commanded three phase voltages to calculate the corresponding dq axes currents and voltages for every data point.
- Based (2.11) and (2.12), the machine flux linkages are calculated and using (2.13) the generated torque can be estimated.
- For SPMSM the maximum torque is archived at a current angle of ($\delta = 90^0$) since

that $L_d = L_q$, in this case the torque is given by 3.1. However, for IPMSM, $L_d \neq L_q$ the current angle needs to be estimated from the dq fluxes using 3.2 to find the point where the motor will be operating at maximum torque.

$$T_{SPMSM} = \frac{3P}{2}\lambda_{pm} i_q \tag{3.1}$$

$$T_{IPMSM} = \frac{3P}{2}(\lambda_{pm} i_q + (L_d - Lq) i_d i_q) \tag{3.2}$$

3.4 Fault Implementation Experimentally

3.4.1 Implementing Eccentricity Fault

For the distributed and the concentrated winding machine, shims of 25% thickness of the airgap were mounted below the machine bearing to lift the rotor and the rotation axis. This shifts the rotor geometry and the rotation axis to the positive y direction without affecting the stator geometry axis, as shown in Fig.3.5a. It would make no difference if the shift was in any other direction or at a different angle. To apply the second severity; additional 4 shims were added on the top of the first 4 shims to further shift the rotor and the rotation axis causing further reduction in the airgap length in the positive y direction and more airgap length in the negative y direction. Two severities were tested 25% and 50%.

For the FSCW machine, a modified brass rings were mounted between the shaft bearing and the end ring. The rings were modified such that the center of these rings is shifted. This caused a shift in the machine rotor geometry and the rotation axis without changing the stator geometry, as shown in Fig.3.5b. The center for the modified rings was shifted based on the desired severity of eccentricity fault. Three rings were used to represent three

severities of eccentricity fault (40%, 60%, and 80%).

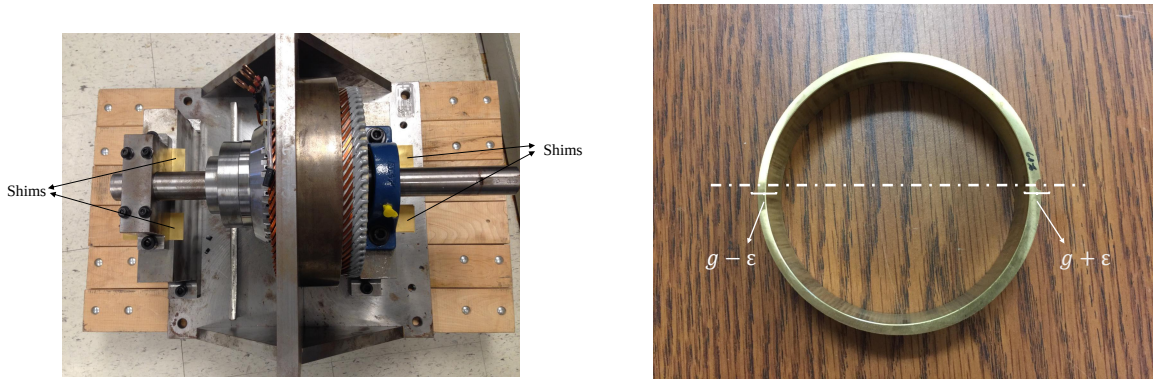

(a) Implementing eccentricity fault for the distributed winding machine

(b) Modified ring for the FSCW machine

Figure 3.5 Implementing eccentricity fault experimentally for the distributed winding machine and the FSCW machine

3.4.2 Implementing Turn-to-turn Short Circuit Fault

Turn-to-turn short circuit fault was applied experimentally to the distributed winding machine and the FSCW machine. For the distributed winding machine, two of the end turns were welded to a copper wire and shorted using a short resistance equal to 200% of the stator phase resistance, as shown in Fig. 6.4. The shorted resistance was chosen to be 200% of the phase resistance because it was the lowest available resistance that can handle the high flowing current under short circuit fault fault. To represent the second severity, another two adjacent end turns were shorted to a short resistance using copper wires. Shorting one end turn is equivalent to shorting 12.5% of the total conductors of phase A, and shorting the second end turn is equivalent to shorting 25% of the total conductors of phase A.

For the FSCW machine, a percentage of the turns of phase A were shorted through a resistance. The number of shorted turns represents the fault severity, two severities were tested, 10% (15 out of 150 turns were shorted) and 20% (30 out of 150 turns were shorted).

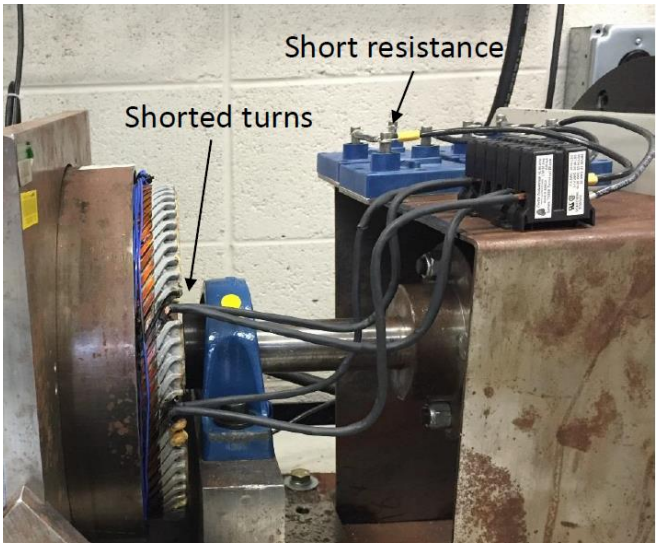

Figure 3.6 Turn-to-turn short circuit fault experimentally

For each fault severity, two shorted resistances were used 0.5Ω and 0.25Ω, which is equivalent to 25% and 12.5% of the stator winding resistance.

3.4.3 Implementing Demagnetization Fault

Demagnetization fault was applied experimentally only to the FSCW machine. A non-magnetic material, was used to replaced the healthy magnet. Only partial demagnetization with 100% demagnetization was applied. Three severities of demagnetization fault were tested by changing one, two and three magnets. The corresponding demagnetized magnets is shown in Fig.6.2

Neodymium Iron Boron (NdFeB) Magnets with permeance ($\beta_r = 1.2T$) and relative permeability of ($\mu_r = 1.05$) was chosen as the material for the magnets. Stainless steel material was used to replace the demagnetized magnets. This material have the same conductivity and relative permeability as the magnets material, but with zero magnet permeance.

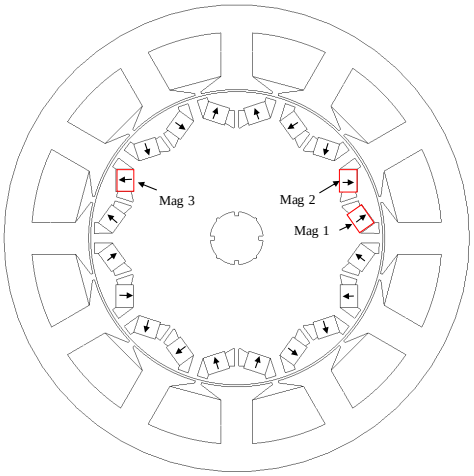

Figure 3.7 Implementing demagnetization fault experimentally.

Chapter 4

The Incremental Inductance Approach

Of the different changes faults might cause to the machine, changing the saturation level is one of these main changes. Faults will cause a disturbance in the magnetic flux distribution, which affects the localized and the total flux linkages in the machine causing a change in the machine saturation. This change is reflected in the incremental inductance curve as a change in the peak amplitude and/or a shifts of the position of the peaks. Based on the shift direction and the amplitude of the curve peaks, the type of the fault can be detected and its severity can be estimated. This chapter shows how to use the incremental inductance curve as a fault detection and separation technique. This approach can be performed when the motor is at standstill, it can also be used as a testing stage at the end of a manufacturing line to check the machine health status.

4.1 Definition of Incremental Inductance

Fig.4.1 shows the saturation curve for PMSM. This curve represents the relation between the d axis flux (λ_d) and the d axis current (I_d). The saturation curve can be divided into three regions: the linear region, the knee region and the saturation region. In the linear

region the relation between λ_d and I_d is linear and can be given by:

$$\lambda_d = L_d I_d + \lambda_m \tag{4.1}$$

The knee region, is the region where the machine starts to saturate. There, the relation between λ_d and I_d starts to change from linear to nonlinear. The saturation region is the region when the relation between λ_d and I_d is nonlinear. It is important to note that the saturation curve depends on the machine geometry and the materials characteristics of the stator, the rotor, and the magnets. The incremental inductance is defined as the rate of change of λ_d over I_d as follow:

$$\hat{L_d} = \frac{\Delta\lambda_d}{\Delta I_d} \tag{4.2}$$

The knee region will appear as a peak in the incremental inductance curve. This peak can be used as an indicator to show when the machine starts to saturate. Fig.4.1 shows the saturation curve and the corresponding incremental inductance.

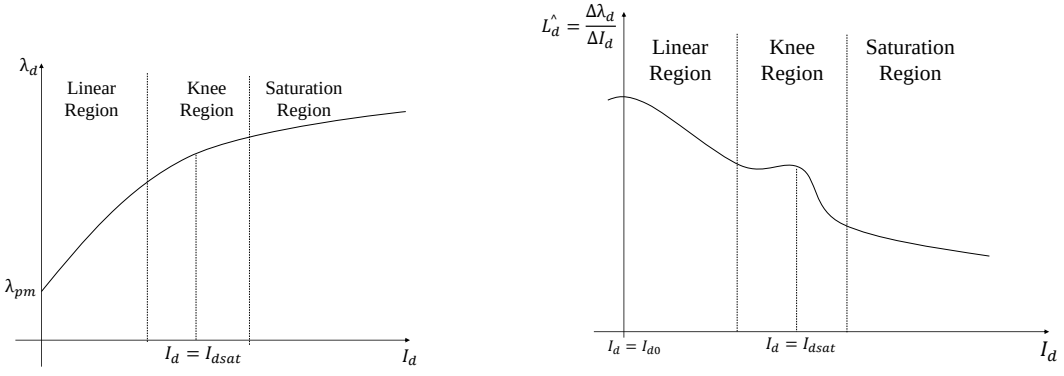

(a) λ_d vs I_d curve. (b) Incremental inductance vs I_d curve.

Figure 4.1 Incremental inductance curve

4.2 Effects of Faults on the Incremental Inductance Curve

It was shown in Chapter 2 that in the case of eccentricity fault the total flux linkages in the machine will be higher compared to healthy machine. This will cause an early saturation in the machine. This early saturation means that the machine require less current to saturate, which can be observed in the incremental inductance as a shift of the knee region peak to the left, and a change in the peak's amplitude. The amount of the shift depends on the severity of eccentricity fault; as the severity of eccentricity fault increases, the machine saturates sooner, causing the peak to shift more to the left.

In the case of turn-to-turn short circuit fault, the shorted turns will cause a reduction in the total armature flux in the machine, which causes a shift down in the incremental inductance curve. This shift causes a reduction in the peaks amplitude, but it wont cause a shift in position of the saturation curve peaks. The decrease is proportional to the severity of the short circuit fault. As the number of shorted turns increases or as the value of the shorted resistance decreases, the incremental inductance curve will shift down more.

For partial demagnetization fault, the region with demagnetized magnets will have a similar characteristics of an air region. This will cause two effects in the incremental inductance curve. The total magnetic flux will be lower. Therefore, the motor requires more current to saturate, which mean that the peak of the incremental inductance will have a higher amplitude. Another effect includes an early saturation due to the concentrated flux in the demagnetized magnet area. The region of the demagnetized magnets will force more flux to concentrate causing an early saturation in that region, which causes as an increase in the curve peak at $I_d = I_{d0}$. Fig.4.2 summarizes the effect of each fault on the incremental

inductance curve and how it can be used to detect the type of the fault.

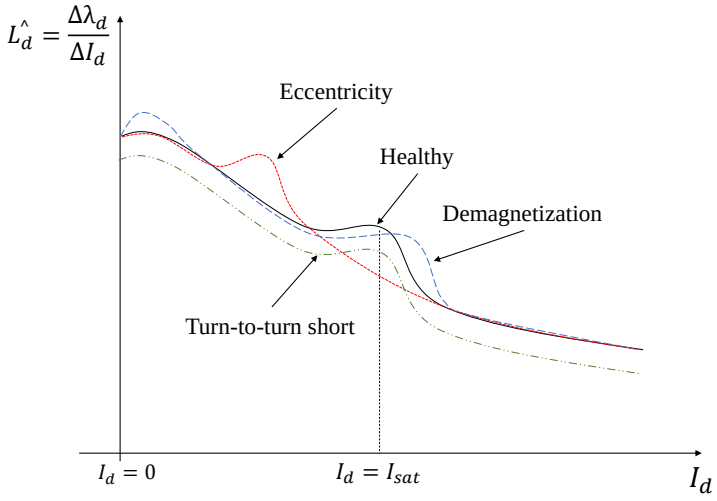

Figure 4.2 Effects on faults on the incremental inductance curve

4.3 Methods to Generate the Incremental Inductance Curve

Different methods can be used to generate the incremental inductance curve. Hong *et al.* [20] proposed a method using the inverter signals to generate the incremental inductance curve. The method is based on applying a small AC current with different offsets to the positive d-axis of the machine while the motor is at standstill. The measured three phase currents and the commanded three phase voltages are fed into Park's transformation to calculate the equivalent currents and voltages space vector using 4.3 and 4.4.

$$v_d = \cos(\theta)v_a + \cos(\theta - \frac{2\pi}{3})v_b + \cos(\theta + \frac{2\pi}{3})v_c \tag{4.3}$$

$$i_d = \cos(\theta) i_a + \cos(\theta - \frac{2\pi}{3}) i_b + \cos(\theta + \frac{2\pi}{3}) i_c \tag{4.4}$$

From the commanded voltages and the measured currents space vectors the motor impendence can be calculated, and from the machine impedance, the incremental inductance can be extracted using 4.5

$$Z_d = \frac{\vec{V_d}}{\vec{I_d}} = r_d + \jmath\omega\hat{L_d} \tag{4.5}$$

where $\vec{V_d}$, and $\vec{I_d}$ are the fundamental components of the voltage and current space vector.

Another method to generate the incremental inductance curve is by rotating the machine at a constant speed and commanding a current to the positive d axis of the machine. As the commanded d axis current increases, the flux linkages will increase causing the machine to saturate. From the measured three phase currents and the commanded three phase voltages, the d and q axis voltages and current can be calculated using (2.11) and (2.12). At steady state operation, the time varying components in (2.11) and (2.12) are equal to zero, so the d and q axis fluxes can be calculated as follows:

$$\lambda_d = \frac{V_q - R_s.I_q}{\omega_e} \tag{4.6}$$

$$\lambda_q = \frac{V_d - R_s.I_d}{-\omega_e} \tag{4.7}$$

The commanded current is applied to the positive d axis of the machine, so the q axis current will be equal to zero. Therefore, (4.6) is given by (4.8), and the incremental inductance curve can be generated using (4.2).

$$\lambda_d = \frac{V_q}{\omega_e} \tag{4.8}$$

This approach is different than the typical control for PMSMs. During normal control, the current is applied to the q axis of the machine in order to produce torque. However, in this case, the current is applied to the positive d axis ($I_q = 0A$) to control the flux in the machine, in this case no torque is produced. The main objective is to increase the saturation in the machine by increasing the total flux.

4.4 Comparison Between the Incremental Inductance Approaches

Using any of the two methods should make no difference in order to generate the incremental inductance curve. However, using the stand still approach might produce some difficulties. First, the stand still method is affected by the rotor position. Fig.4.3 shows the FEA simulation results for the change in the incremental inductance curve for the FSCW machine by changing the rotor position in steps of 2 mechanical degrees.

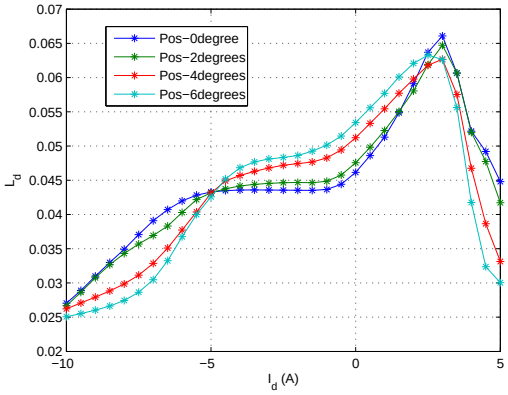

Figure 4.3 Effects of rotor position

It can be noted that the rotor position affects the shape and the peak position of the generated incremental inductance curve. This can affect the accuracy of fault detection if

the motor is tested at different positions. The change in the incremental inductance due to the rotor position is based on the the motor geometry and the relation between the number of poles and slots. Fig.4.4 shows a comparison of the incremental inductance curve for both the concentrated and the distributed winding machines calculated using the two methods.

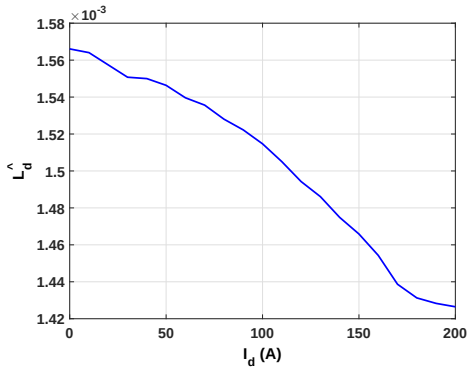

(a) Concentrated winding machine Standstill method

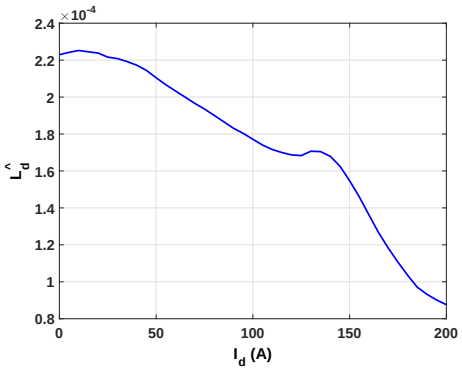

(b) Distributed winding machine Standstill method

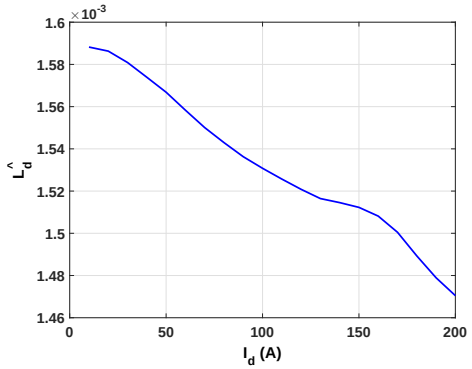

(c) Concentrated winding machine Rotation method

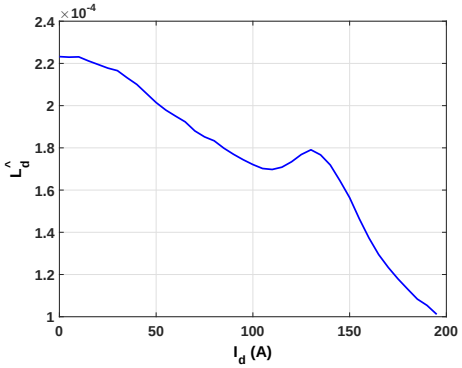

(d) Distributed winding machine Rotation method

Figure 4.4 Comparison between the two methods to generate the incremental inductance method (FEA simulation)

It can be noticed that for the distributed winding machine, both methods generate similar curves, in which it is clear to detect the position and the amplitude of the incremental inductance peaks using both methods. However, for the concentrated winding machine, it is not possible to detect the peak using the standstill method. This is due the the motor geometry and the slot/pole combination: for the distributed winding machine, at any rotor

position, the d-axes are aligned to both a tooth and a slot which average the total flux. For the concentrated winding machine, all the rotor d-axes are aligned with either a tooth or a slot at any instant of time, causing an unbalance in the magnetic flux linkages based on the rotor position. For the rotating method, since that the motor is rotating at a constant speed, the d-axis will face both a slot and a tooth, which average the total airgap flux. The effect of the machine geometry can be solved by rotating the motor at a very low speed while applying the AC current signal. This allows the d-axis to pass by a slot and a tooth, which average the total flux, and since that the motor is rotating at a very low speed, then the effect of the Back emf voltage is neglected.

Another factor that needs to be considered while using the standstill approach is the amplitude of the AC current; applying a large AC amplitude will affect the amplitude of the generated incremental inductance curve peak. In some cases if the amplitude of the incremental inductance curve is too high it might mask the appearance of the peak if the knee region is too small. Fig.4.5 shows the simulation results for the changes in the incremental inductance curve using the standstill test with different amplitudes of the AC signal for the FSCW machine under healthy conditions.

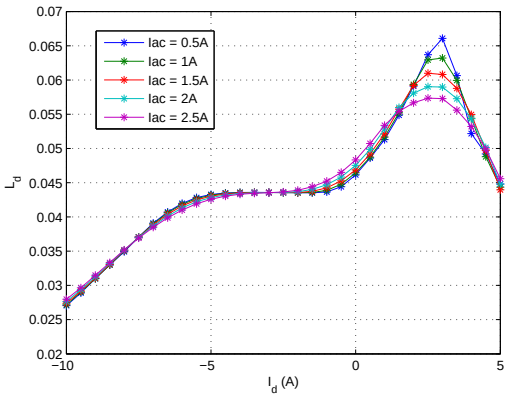

Figure 4.5 Effects of the AC current amplitude

It can be noted that as the amplitude of the AC signal increases, it becomes harder to detect the peak of the incremental inductance curve. Therefore, it is preferred for the AC signal to be as low as possible. however, the amplitude of the AC signal is chosen based on the machine parameters and the control resolution.

To overcome the drawbacks of the standstill method, the motor can be rotating at a very low speed while applying the AC signal to the d-axis. The motor is rotate a very slow speed to allow the d-axis to pass by a tooth and a slot, which average the total flux, and neglect the effect of the position dependent. The motor needs to be operating at a very low speed to neglect the effect of the induced back emf due to the rotation of the rotor. For this work the incremental inductance curve was generated experimentally by rotating the motor at a low speed ($10rpm$), and exciting the positive d-axis with a small AC signal of amplitude $0.5A$ at a frequency of $100Hz$. Fig.4.6 shows comparison of the incremental inductance generated using the slow rotation method and the fast speed method using FEA simulation. It can be noted that there is no difference between the two methods (slow rotation and fast rotation) in the shape of the incremental inductance curve, since that both of them account for the variation in the flux due to the slots and tooth. The main drawback of using the rotating method is that the incremental inductance is generated using the derivative of the flux, which may introduce noise especially from the experimental data.

4.5 Simulation and Experimental Results

Fig.4.7 shows the calculation of the incremental inductance curve using FEA simulations for the concentrated winding machines under healthy and the three tested faults with different severities. The incremental inductance curves were generated using the rotating method,

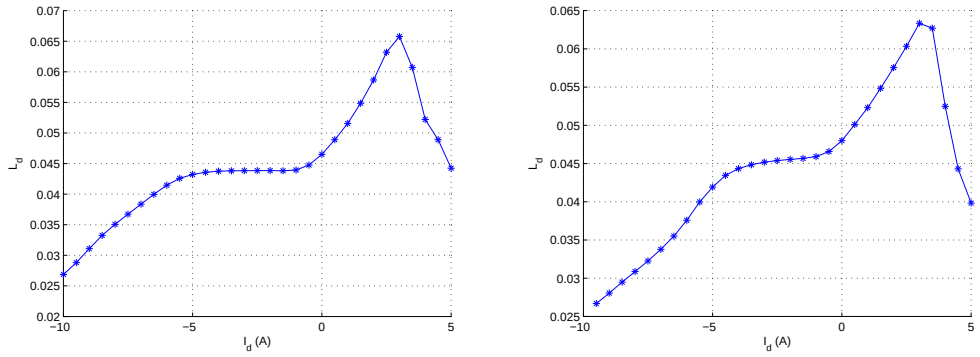

(a) Slow rotation method (b) Fast rotation method

Figure 4.6 Incremental inductance comparison between the slow rotation method and the constant speed method

the motor was operating at a speed of $500rpm$, the applied d-axis current was varied from -50 to $200A$ in steps of $5A$. Four severities of eccentricity fault were tested (20%, 40%, 60% and 80%), three severities of partial demagnetization fault, by fully demagnetizing 1, 2 and 3 magnets, and three severities of turn-to-turn short circuit fault. The severities of short circuit fault were varied by shorting 12.5%, 25% and 62.5% of the turns in phase A coils through a resistance of 0.25Ω.

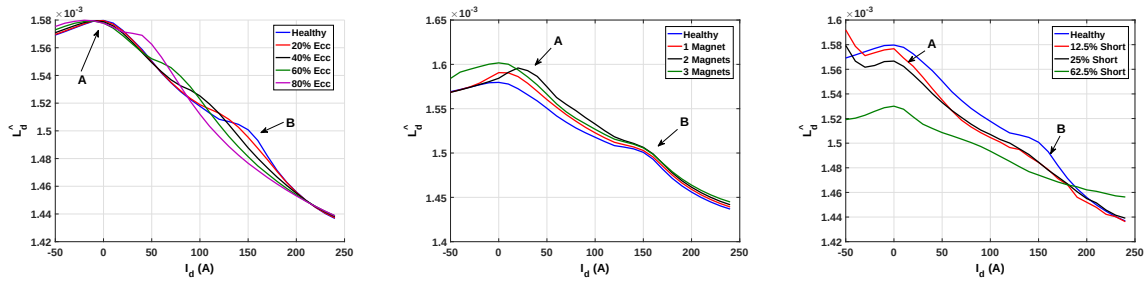

(a) Incremental inductance variation eccentricity fault (b) Incremental inductance variation demagnetization fault (c) Incremental inductance variation turn-to-turn short circuit fault

Figure 4.7 Incremental inductance variation under different faults

Fig.4.8 shows a comparison between the experimental and the FEA simulation results for the distributed winding machine under healthy, two severities of eccentricity fault (25%

and 50%) and two severities of turn-to-turn short circuit fault (12% and 25%).

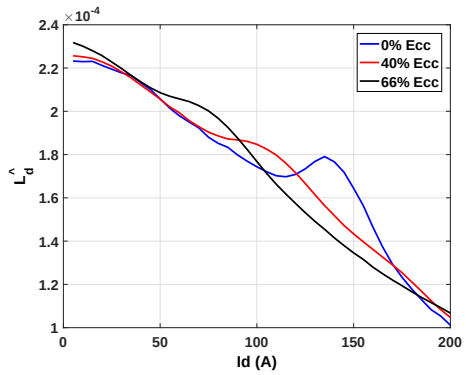

(a) Simulation results for eccentricity fault

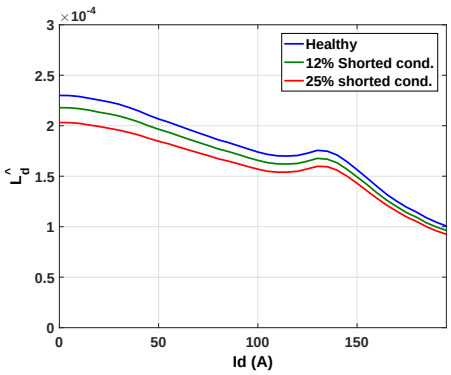

(b) Simulation results for short circuit fault

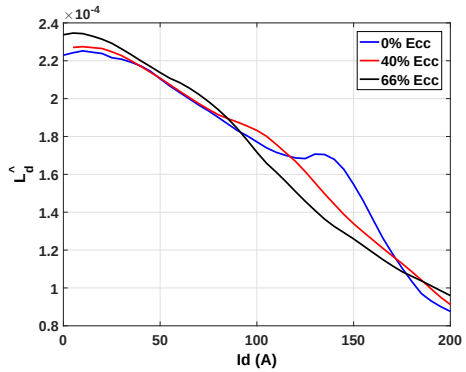

(c) Experimental results for eccentricity fault

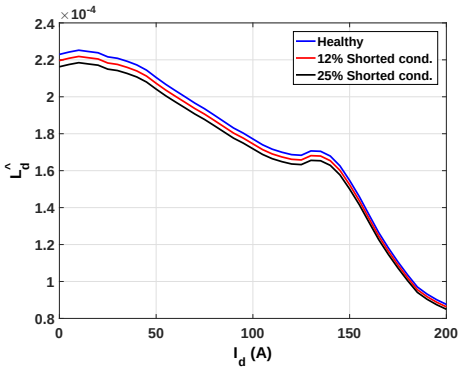

(d) Experimental results for short circuit fault

Figure 4.8 Comparison between simulation and experimental incremental inductance results

Fig.4.9 shows a comparison between the experimental and the FEA simulation results for the FSCW machine under healthy, three severities of eccentricity fault (40%, 60% and 50%) and three severities of demagnetization fault (1, 2, and 3 magnets were fully demagnetized).

As discussed earlier, it can be noted that in the case of static eccentricity fault, the peak of the incremental inductance is shifted to the left (point B), while no change in the peak amplitude or position at $I_d = 0$ (point A). It can also be noted that the amount of the shift depends on the severity of the fault. As the severity of the fault increases, the shift in the peak will also increases. For the concentrated winding machine, it start to saturate at

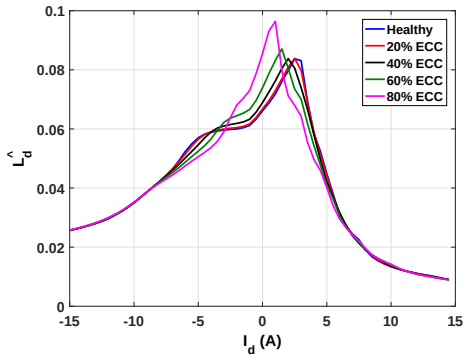

(a) Simulation results for eccentricity fault

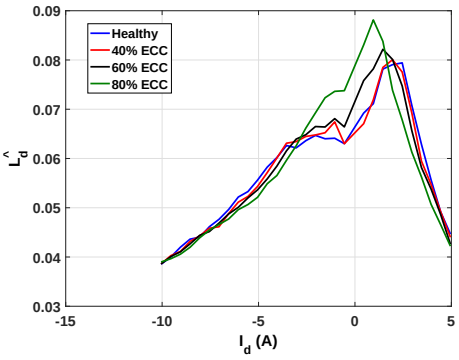

(b) Simulation results for experimental fault

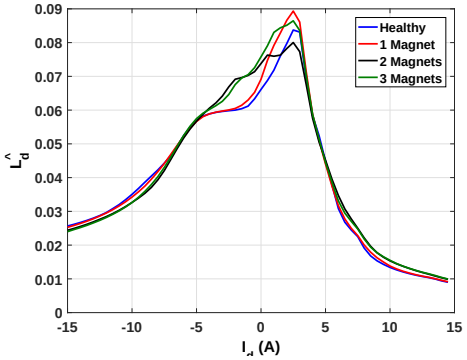

(c) Experimental results for demagnetization fault

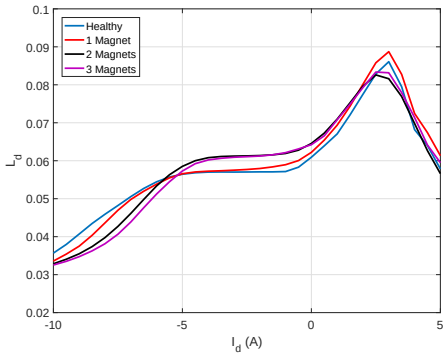

(d) Experimental results for demagnetization fault

Figure 4.9 Comparison between simulation and experimental results for the FSCW machine

$I_d = 150A$. However, for a static eccentricity fault of 80%, the peak position was shifted from $I_d = 150A$ to $I_d = 45A$. For the distributed winding machine the saturation peak was shifted from $I_{dsat} = 135A$ to $I_{dsat} = 75A$ under 66% eccentricity. The peak shift can also be noticed for the FSCW machine under static eccentricity fault. Fig.4.10 shows the relation between the severity of eccentricity fault vs the saturation current I_{dsat} (point B) for the concentrated and the FSCW machines. It is clear that the relation between the severity of eccentricity fault and I_{dsat} is almost linear. Based on this curve, any severity of static eccentricity fault can be estimated using the peak position.

In the case of partial demagnetization fault, due to the early saturation in the demag-

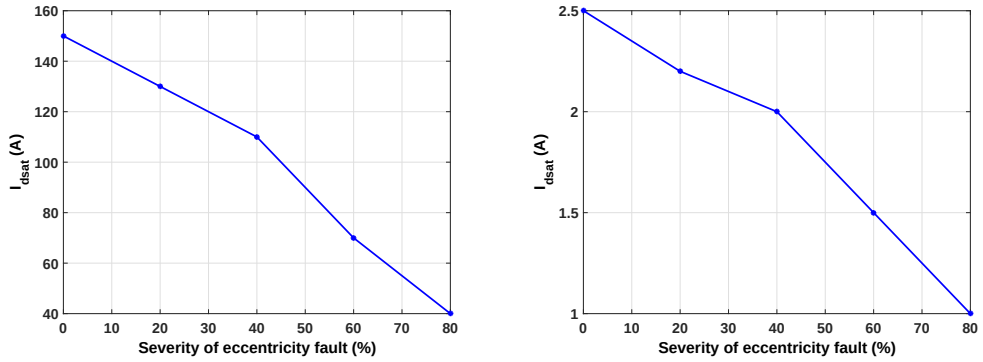

(a) concentrated winding machine (b) FSCW machine

Figure 4.10 The change in I_{dsat} under static eccentricity fault

netized magnets region, a change in the peak amplitude and position can be noted in the incremental inductance curve at $I_d = 0$ (point A). However, no detectable change can be noticed in the saturation peak. The change in the peak amplitude and position at $I_d = 0A$ can be used as an indicator to detect the severity of partial demagnetization fault. For turn-to-turn short circuit fault, due to the reduction in the total flux in the motor, the incremental inductance curve is shifted down compared to the healthy case. The amount of the shift depends on the severity of the fault. As the number of shorted turns increases or the shorted resistance increase, the reduction in the incremental inductance will increase.

4.6 Fault Detection and Separation Algorithm

The change in the peaks amplitude and position of the incremental inductance curve can be used as an indicators to detect the fault type and estimate its severity. However, the slope, the position of the peak, and the peak amplitude varies between motors, depending on the machine geometry and the material used. To automate the detection method, the algorithm in Fig.4.11 is proposed.

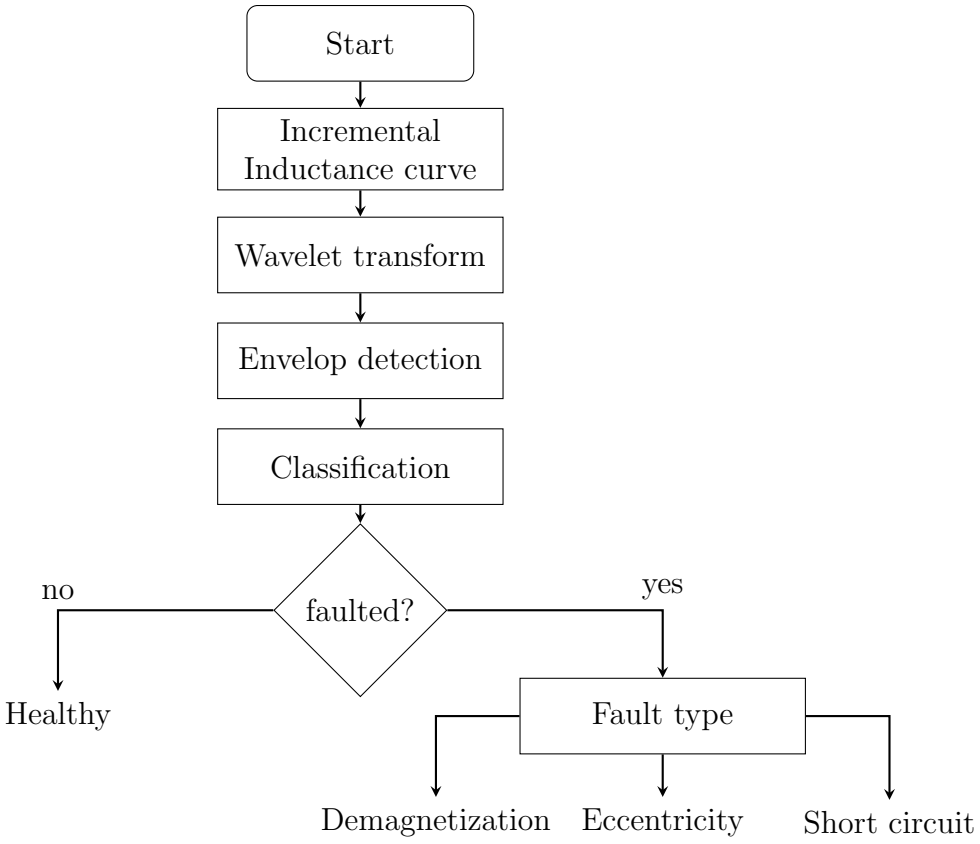

Figure 4.11 Block diagram for the incremental inductance approach

[1] Using any of the proposed methods discussed earlier, the incremental inductance for the tested machine is generated. For the concentrated and the distributed winding machine 50 points were used to generate incremental inductance curve by varying the d-axis current from $0A$ to $250A$ in steps of $5A$. For the FSCW machine 31 points were used to generate incremental inductance curve by varying the d-axis current from $-5A$ to $10A$ in steps of $0.5A$

[2] Wavelet transform is applied to the incremental inductance curve to detect the curve peaks. For this work, a 4 level Haar wavelet decomposition is applied. In order to have a better resolution for the wavelet transform, interpolation was applied first to the incremental inductance curve to increase the curve resolution.

[3] Using an envelope detection algorithm, the peaks and the corresponding d-axis current can be detected (points A ad B) as shown in Fig.4.12

[4] The d-axis current and the value of the incremental inductance at the d-axis current can be used as the classifier features. The output of the classifier defines the machine health status, detects the fault type, and estimates its severity.

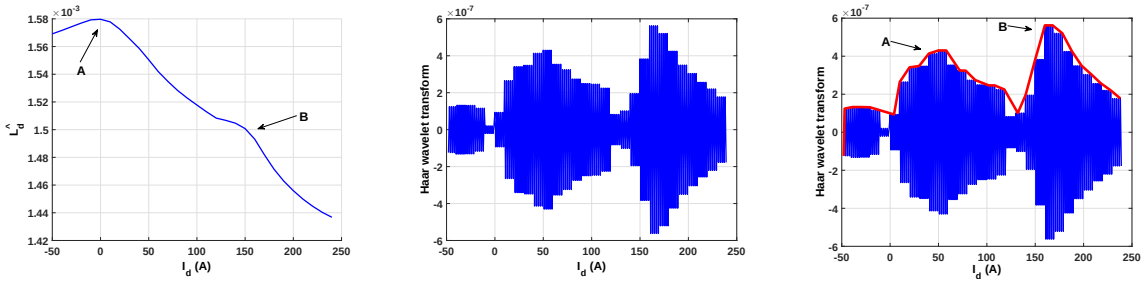

(a) Incremental inductance healthy case (b) Haar wavelet transformation (c) Envelope curve detection

Figure 4.12 feature extraction for kNN classifier

Three classification approaches were applied to validate the detection and estimation method: k-Nearest Neighbor, Linear Discriminant Analysis, and Quadrature Discriminant Analysis. The same features were selected for each classifier.

4.6.1 k-Nearest Neighbor

k-NN [41] is a common non-parametric classification method. In this classifier, for a known training vector, the sample space is divided into a number of clusters based on a distance function. A tested sample is assigned to a specific cluster with the nearest k samples. For this work k is chosen to be 1, which means that the tested sample is assigned to its closest sample in the sample space. The distance function is chosen to be Euclidean distance. For a $j \times n$ training matrix Y and a $l \times n$ testing matrix X, the Euclidean distance is given as:

$$d_{XY} = \sqrt{\sum_{i=1}^{n}(x_{mi} - y_{pi})^2} \tag{4.9}$$

where $X = [x_{m1}, \ldots, x_{mn}]$ is the tested matrix, $Y = [y_{p1}, \ldots, y_{pn}]$ is the training matrix, $m = 1, \ldots, j$ is the number of tested samples and $p = 1, \ldots, l$ is the number of testing samples. The amplitude and the position of the peaks are used as features for k-NN classifier.

4.6.2 Discriminant Analysis

Discriminant Analysis is used to maximize the ratio between the variance for different classes and the variance within the same class to achieve maximum separation between the feature sets in each class. For this classifier, the sample space is divided into K classes, where each class consists of a specific number of samples corresponding to the same state. These classes are associated with weighting coefficients, and each class has its own coefficients that are used to calculate the corresponding discriminant function for that class. The discriminant function for class k is given by (4.10)

$$C_k(X) = \alpha_{1k}x_1 + \alpha_{2k}x_2 + \cdots + \alpha_{Nk}x_N + \alpha_{N+1k} \tag{4.10}$$

where $X = [x_1, x_2, \ldots, x_N]$ is the N dimensional sample vector and $[\alpha_{1k}, \alpha_{2k} \ldots \alpha_{N+1k}]$ is the coefficient matrix for the k^{th} class.

The weighting coefficient matrix is determined using an iterative process, the training phase. During this phase, since we know the proper classification for each sample, the weighting matrix will keep changing until each sample is classified into its correct class. To classify an unknown sample, the measured coefficients from the training phase are used in (4.10) to calculate the discriminant functions for this sample. A sample vector belongs to a

particular class if the linear discriminant function for that sample is greater than any other linear discernment function. For example, a sample vector i belongs to a class j if,

$$C_j(X_i) \geq C_k(X_i) \qquad \forall j \neq k \tag{4.11}$$

4.6.3 Classification Methodology and Results

FEA simulations and experimental tests were performed to generate the incremental inductance curve under healthy and faulted conditions. For the concentrated winding machine, 11 cases were generated using FEA. One case corresponds to the healthy conditions, four cases correspond to static eccentricity fault, generated by varying the severity from 20% to 80% in steps of 20% of the airgap length, three cases corresponds to demagnetization fault, by demagnetized 1, 2 and 3 consecutive magnets, and three cases represent turn-to-turn short circuit fault (12.5% and 25% and 62.5% of the total phase A conductors are shorted). For the distributed winding machine, a total of five cases were generated. Two faults were tested using both FEA and experimentally; a case for healthy condition, two severities of static eccentricity fault (40% and 66%) and two severities of turn-to-turn short circuit fault (12% and 25%). For the FSCW machine 12 cases were generated using FEA, one for healthy, 4 for eccentricity fault (20%-40% in steps of 20%), three cases for demagnetization by demagnetizing 1, 2, and 3 adjacent magnets, and 4 cases represent short circuit fault (10% with $R_f = 0.5$, 12% with $R_f = 0.25$, 20% with $R_f = 0.5$, and 20% with $R_f = 0.25$). Experimental tests were performed for the FSCW machine under healthy, static eccentricity, and partial demagnetization faults.

Four features were extracted from each case: the saturation current $I_{dsat} = I(B)$, the

incremental inductance peak amplitude at the saturation current ($L(I_{dsat}) = L(B)$), the zero d-axis current ($I_{d0} = I(A)$), and the incremental inductance peak amplitude at the zero d-axis current ($L(I_{d0}) = L(A)$). 100 samples were generated from each case by varying the selected $d\text{-}axis$ and the corresponding incremental inductance amplitude around $I_d = I(A)$ and $I_d = I(B)$. 10 currents were selected around $I_d = I(A)$ and another 10 currents were selected around $I_d = I(B)$. The variation of the current was chosen to be 15% of the selected currents, (i.e. if the machine saturates at $I_d = 150A$, the selected currents varies from $142.5A$ to $157.5A$). A total of 100 combination samples can be generated for all the current combinations. The feature vector for each sample is selected based on (4.12)

$$x_j^i = [I^{ij}(A) \quad L^{ij}(A) \quad I^{ij}(B) \quad L^{ij}(B)] \tag{4.12}$$

where i is the number of machine health status cases, j is the number of samples in each case, and x is the features vector. All the samples for healthy and faulted cases were combined together in one classification matrix. The leave one out method was used to validate the classification results; one sample from the sample space is selected and left out. The coefficient matrix is calculated from the rest of the samples. The selected sample was classified using these coefficients. This process was then repeated for every sample in the sample space. Each time the coefficients are recalculated and the left-out sample is classified using these coefficients. The classification accuracy for each class was calculated as:

$$CC(\%) = \frac{N_{correct}}{N_{total}} \times 100\% \tag{4.13}$$

where $N_{correct}$ is the number of samples that were classified correctly, and N_{total} is the total number of samples in the sample space. Table 6.3 compares the classification results for

the concentrated winding machine using the three classifiers. Table 4.2 shows a comparison of the classification results between simulations and experimental data for the distributed winding machine, and Table 6.4 shows the classification results for for the FSCW machine.

Table 4.1 Classification results for the concentrated winding machine

	Concentrated winding machine		
Machine Status	K-NN	LDA	QDA
Healthy	90%	98%	95%
20% Eccentricity	80%	96%	95%
40% Eccentricity	82%	100%	98%
60% Eccentricity	100%	100%	100%
80% Eccentricity	100%	100%	100%
1 Magnet	82%	98%	95%
2 Magnets	85%	97%	96%
3 Magnets	96%	98%	98%
12.5% Short	83%	92%	92%
25% Short	90%	90%	90%
50% Short	92%	90%	90%

Table 4.2 k-NN Classification results for the concentrated winding machine

	Distributed winding machine					
	FEA Simulation			Experimental results		
Machine Status	K-NN	LDA	QDA	K-NN	LDA	QDA
Healthy	80%	97%	95%	80%	92%	91%
40% ECC	90%	100%	97%	88%	97%	97%
60% ECC	93%	100%	98%	89%	98%	98%
12.5% Short	88%	95%	95%	85%	90%	90%
25% Short	85%	100%	97%	83%	92%	88%

Table 4.4 summarizes the the average classification results for all tested machines using the three classification methods.

The classification results show that the proposed algorithm was able to detect the fault type and estimate its severity accurately. Even for the cases when the severity are not

Table 4.3 k-NN Classification results for the concentrated winding machine

	Distributed winding machine					
	FEA Simulation			Experimental results		
Machine Status	K-NN	LDA	QDA	K-NN	LDA	QDA
Healthy	92%	96%	97%	90%	97%	96%
40% ECC	82%	100%	95%	80%	92%	93%
60% ECC	88%	98%	94%	82%	95%	94%
80% ECC	88%	100%	94%	90%	94%	94%
1 Magnet	89%	93%	93%	89%	88%	88%
2 Magnets	84%	96%	95%	85%	88%	87%
3 Magnets	85%	95%	94%	85%	87%	85%

Table 4.4 k-NN Classification results for the concentrated winding machine

	Concentrated winding	Distributed winding		FSCW machine	
	FEA	FEA	EXP	FEA	EXP
KNN	89.1%	87.2%	85%	86.8%	85.8%
LDA	96.2%	98.4%	93.8%	96.8%	91.5%
QDA	95.3%	96.4%	92.8%	94.5%	91%

classified correctly, the algorithm was able to detect the fault type. It is also noted that using LDA classification provide the highest accuracy for fault detection and classification.

4.7 Effects of Parameter Variation

To test the robustness of the detection method, FEA simulations were performed by varying the machine operating and environmental conditions. Two parameters were varied: the aligning angle and the operating temperature. The incremental inductance curve depends on the change in the saturation of the machine. Therefore, it is important for the applied d-axis current to be accurately aligned to the rotor d-axis. Any misalignment between the applied current and the rotor d-axis will affect the saturation in the machine. To estimate

the sensitivity of the aligning angle, the motor was misaligned by 1, 6 and 10 mechanical degrees. The results of the incremental inductance under different misalignment angles for the concentrated winding machine are shown in Fig.4.13

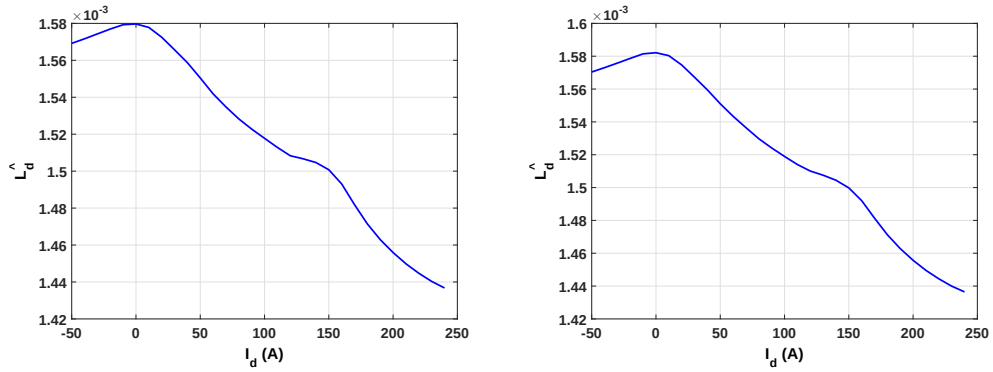

(a) Incremental inductance healthy 0 degree misaligned

(b) Incremental inductance healthy 1 degree misaligned

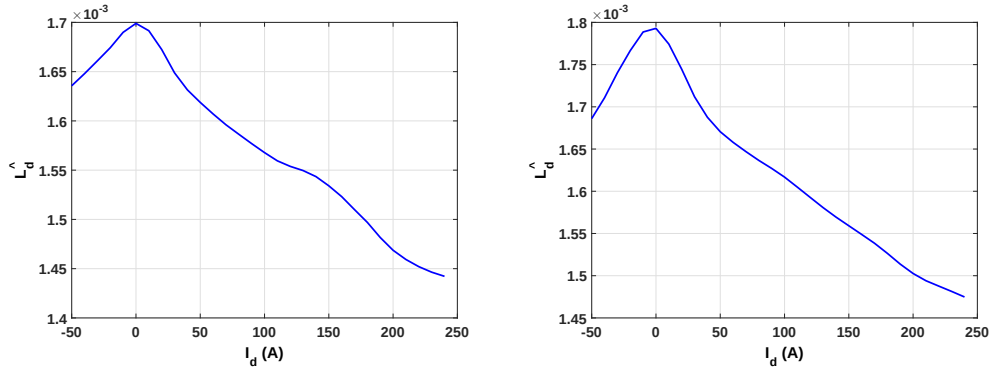

(c) Incremental inductance healthy 6 degree misaligned

(d) Incremental inductance healthy 10 degree misaligned

Figure 4.13 incremental inductance under different misaligning angle

To vary the operating temperature of the machine, the motor stator resistance and the magnet permeance were changed in the model based on the following equations:

$$R_s(T) = R_{s0}\left[1 + \alpha_R(T - T_0)\right] \tag{4.14}$$

$$B_r(T) = B_{r0}\left[1 + \alpha_{Br}(T - T_0)\right] \tag{4.15}$$

where α_R is the temperature coefficient for the stator resistance ($\alpha_R = 0.00393$), α_{Br} is the temperature coefficient for the magnets ($\alpha_{Br} = -0.0011$), T is the operating temperature, and T_0 is the reference temperature. Three temperatures were tested 20^0C,100^0C and 150^0C. The results of the incremental inductance curve under temperature variation for the concentrated winding machine is shown in Fig.4.14

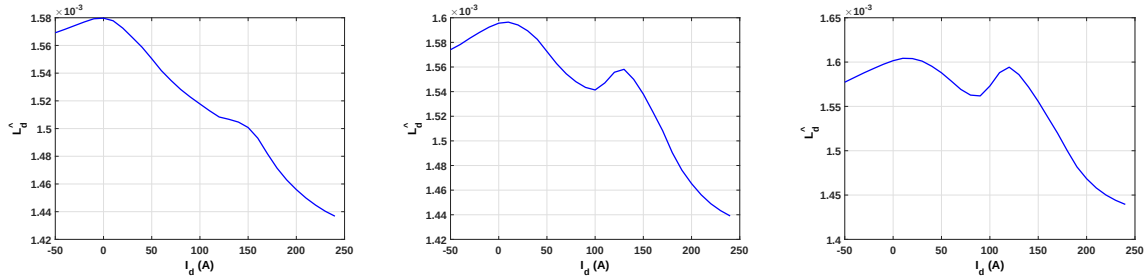

(a) Incremental inductance healthy at $T = 20^0C$ (b) Incremental inductance healthy at $T = 100^0C$ (c) Incremental inductance healthy at $T = 150^0C$

Figure 4.14 variation of the operating temperature

It can be noted that the effect of the operating temperature won't affect the shape of the incremental inductance curve; the two peaks were still detectable. However, in the case of the aligning angle, as the machine became more misaligned, it became harder to detect the saturation peak and therefore estimate the fault type. Table 4.5 shows the classification results for the concentrated winding machine under different parameter variations.

Table 4.5 k-NN Classification results under parameters variation

	Classification Results					
Classifier	20^oC 0 degree	100^0C 0 degree	150^0C 0 degree	20^oC 1 degree	20^oC 6 degree	20^oC 10 degree
KNN	89.1%	88%	85%	89%	84%	80%
LDA	96.2%	95%	94.2%	96%	91%	83%
QDA	95.3%	93%	92.2%	95%	90%	81%

The classifier was able to detect the fault type and its severity with a good accuracy

for different levels of variations in the operating temperatures. The main parameter that needs to be considered is the aligning angle. Inaccurate aligning angle will mask the fault signature, which will reduce the detection accuracy, only 80% of the samples were classified correctly in the case of 10 degree misaligned angle compared to a 96.3% with correct aligning using the KNN classifier.

Chapter 5

The MC/VSA and LDA Classification Approach

Most of the detection methods in the literature using the MCSA approach have been tested for single fault detection. They are based on analyzing the stator current signal under healthy and faulted conditions. The amplitude of the generated subharmonics are used to detect the fault type and estimate its severity. The use of these subharmonics presents some difficulties. It was shown in [5] and [9] that similar side band patterns will appear for both eccentricity and short circuit faults, which makes this approach unable to separate between the two faults. Also, the amplitudes of the generated subharmonics depend on the operating speed and load conditions; at lower speeds it was difficult to detect these sideband patterns compared to high speed operation [25]. In [26] and [27], it was shown that the relation between the number of poles and the stator slots affects the appearance of the stator current subharmonics related to eccentricity faults. Based on this, using the subharmonics only for fault detection might not be adequate for fault detection and separation. On the other hand, there will always be a change in the amplitude of the harmonics of the voltage or the current signals in faulted cases. The change in the amplitude is related to the type and the severity of the fault.

The main objectives of this chapter include 1) evaluating the accuracy of using the MCSA

and the LDA to detect the machine status, whether it is healthy or faulted, separation between different faults, and estimation of the fault severity. 2) Using either the measured stator currents or the commanded voltages for fault detection and identification. 3) Using the amplitude of the harmonics as fault detection and classification features instead of the subharmonics. This approach can be used as a method to separate between different fault when the motor is operating at steady state. However, Since that only the first 15 harmonics are needed for the classifier, only few cycles are needed which can be extracted when the motor is at operating standstill for a short period of time.

5.1 Algorithm for Fault Detection and Classification

Fig.5.1 shows the general flow diagram for the fault detection algorithm using the MC/VSA approach. The algorithm contains two classifiers: The first classifier is used to detect the presence and type of the fault, while the second is used to estimate the fault severity once the type of fault is determined. The proposed method is as follows:

[1] Three phase currents are used to control and operate the machine under both healthy and faulted conditions. The stator phase current or voltage signals in the *abc* frame of reference were measured for processing.

[2] FFT was applied to the measured current or voltage signals. The amplitudes of the harmonics were selected as features for the classification. In this method, a vector of the amplitude of the first 15 harmonics was chosen from phase A spectrum, as the features for each sample. (i.e. the fundamental and the harmonics 2^{nd}-15^{th})

[3] LDA classification is applied to detect whether the machine is healthy or faulted, and

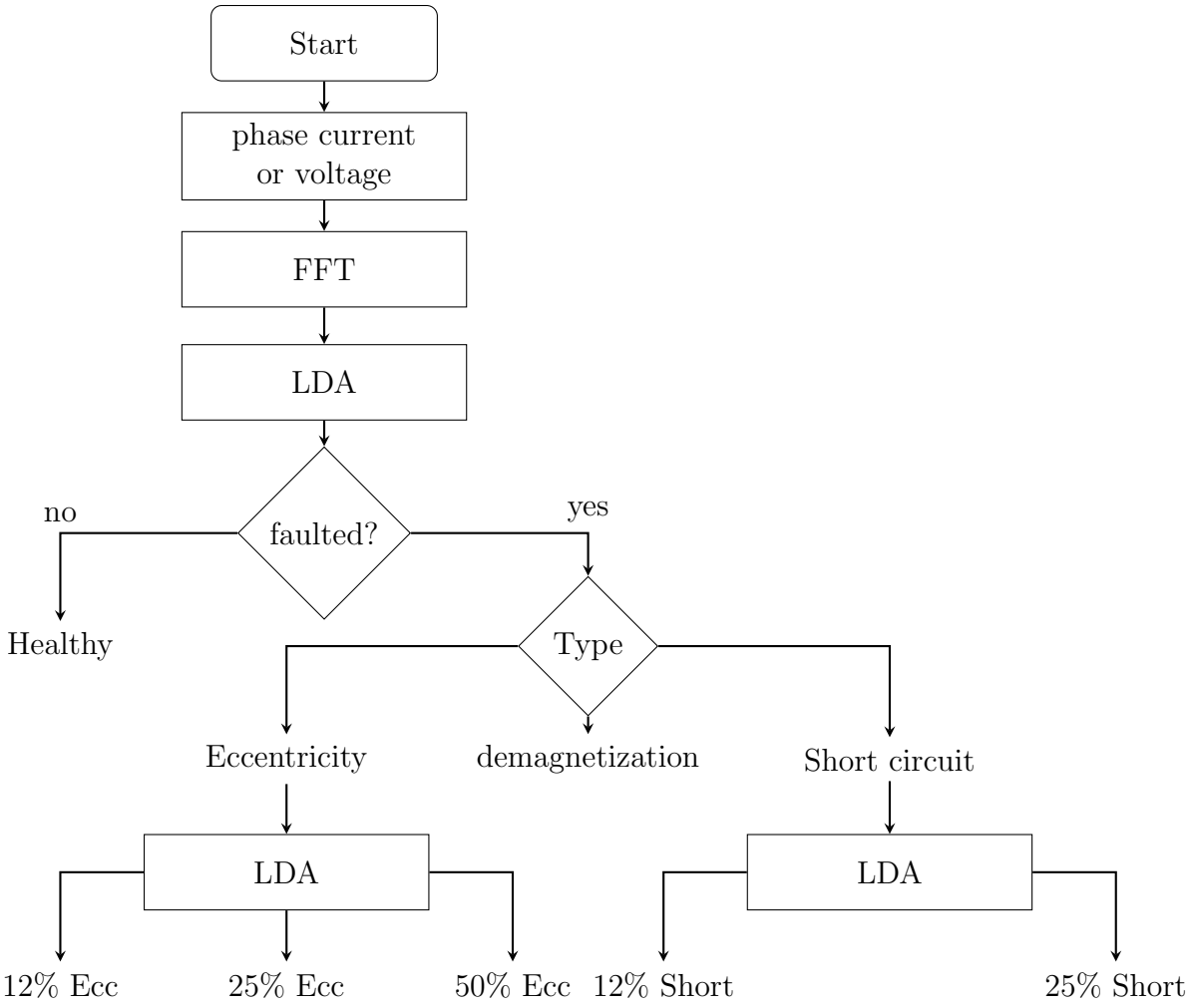

Figure 5.1 Block diagram for the MC/VSA approach

determine the type of the fault. The sample space for the first classifier contains samples from all the studied faults. In the faulted case, it detects the type as one of the following: static eccentricity, turn-to-turn short circuit, or partial demagnetization.

[4] If the fault is detected as static eccentricity or turn-to-turn short circuit fault, another LDA classifier is applied to determine the severity of that fault. In this classifier, the sample space contains samples from the same type of fault but with different severities.

5.2 Simulation and Experimental Results

Fig.5.2a shows the spectrum of the stator current for the distributed winding machine under healthy and two faults with different severities (25% and 50% of eccentricity fault and 12% of the coils in phase A shorted). Fig.5.2b shows the spectrum of the stator current of the concentrated winding machine under healthy and two severities of eccentricity faults (25% and 50%). The current spectrum was collected experimentally for a load of $50A$ and operating speed of 500 rpm. The change in the amplitudes of the 5^{th} and 7^{th} harmonics were under faulted cases compared to the healthy one.

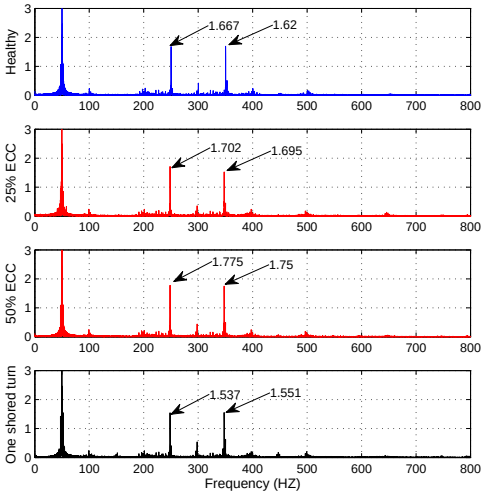

(a) Experimental results of the stator current spectrum for the distributed winding machine

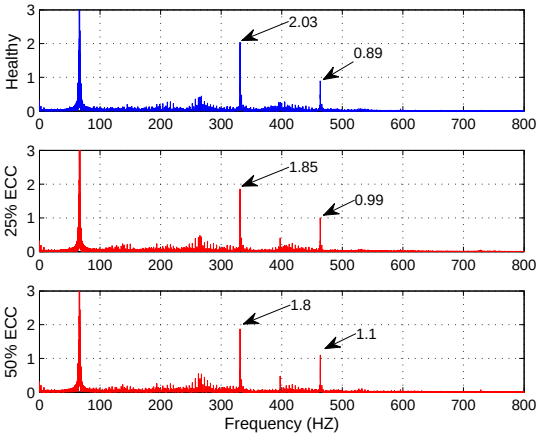

(b) Experimental results of the stator current spectrum for the concentrated winding machine

Figure 5.2 Experimental results for the stator current harmonics under different faults

It can be noticed from Fig.5.2 that faults introduces different changes to the current spectrum, the amplitude of some harmonics like the 5^th harmonic increases in the case of eccentricity fault, but it decreases in the case of turn-to-turn short circuit fault. This change depends on the type and the severity of that fault. These changes in the harmonics amplitude can be used as classification features to detect the fault type and estimate the severity. It

is important to mention that the harmonics of the current signal from phase A only were selected for the classification features. This might affect the results for short circuit fault but not demagnetization or eccentricity. However, the short circuit fault was applied using a high short resistance ($R_f = 0.125\Omega$), while the machine phase resistance is around 0.1Ω. This reduces the unbalance between the three phases. Fig.5.3 a comparison of the current spectrum from phase A, B and C in the case of 12% turn-to-turn short circuit fault for the distributed winding machine. The harmonics from the three phases have similar amplitudes. Therefore, this method is able to detect the short circuit fault, no matter which phase the harmonics were selected from. However, it is not able to detect which phase is the shorted one.

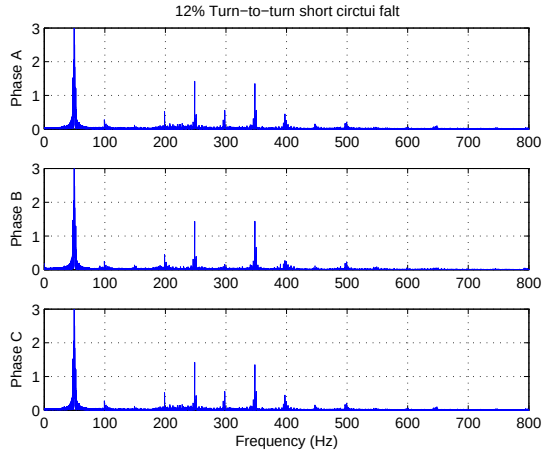

Figure 5.3 Comparison between the current spectrum from phase A, B and C under 12% short circuit fault

The reason why all the first 15 harmonics were chosen as features for the classifier, is that turn-to-turn short circuit fault often generates even order harmonics, Therefore, both the odd and the even harmonics were selected to improve the detection accuracy in the case of short circuit fault. Fig.5.4 shows a comparison of the current spectrum between healthy case and 25% short circuit fault. The increase in the harmonics amplitude at 200 and $400Hz$

(4^{th} and 8^{th} harmonics) can be noted in the case of short circuit fault.

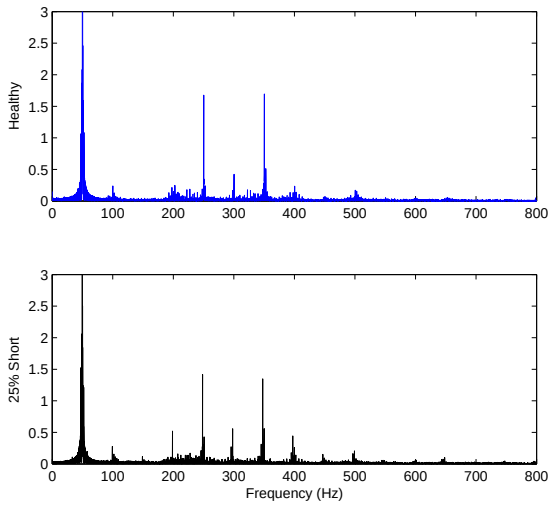

Figure 5.4 Comparison between the current spectrum under healthy and 25% short circuit fault

5.2.1 Identifying the Fault Type

LDA classification is used first to detect the type of fault. Since the first 15 harmonics are used as features for the classifier, a number of samples higher than 15 is required in the sample space for the classification matrix to converge [42]. Table 5.1 shows the classification results of fault detection, for the concentrated and distributed winding machines, using FEA simulation for two different operating loads (30% and 60% of the full load). LDA was performed separately at each load. The sample space contains 44 samples that correspond to four different classes. Each class represents a specific machine state as follows: class 0 corresponds to the healthy case, class 1 corresponds to 12% static eccentricity, class 2 corresponds to 12% shorted conductors (one shorted turn of the distributed winding machine) and class 3 corresponds to 80% demagnetization for one magnet. 11 samples were generated for each class by varying the speed from 1000 rpm to 2000 rpm in steps of 100 rpm. The samples for

each fault were chosen as the minimum accepted severity, so that, if the algorithm was able to detect the fault with lower severity, the fault with a higher severity can also be detected. The first 15 harmonics from the current or voltage spectrum with a sampling frequency of 10 kHz, were chosen as features for the classification. To validate the classification results the leave-one-out method was used.

From the results in Table 5.1, it can be noted that LDA was able to classify the type of fault correctly and distinguish between different faults for both machines at different operating conditions.

Table 5.1 LDA classification results for fault detection using FEA results. (Each class contains 11 samples correspond to speeds $1000 - 2000$ rpm).

	Classification Results			
	Concentrated Winding		Distribution Winding	
	30% full load	60% full load	30% full load	60% full load
Healthy	100%	100%	100%	91%
12% eccentricity	91%	91%	100%	91%
One shorted turn	100%	100%	100%	100%
80% demag.	100%	100%	100%	100%

5.2.2 Determining the Fault Severity

After detecting the fault and determining its type, it is necessary to detect its severity. In this section, it is assumed that the type of fault is correctly detected. Another LDA classification was used again to estimate the severity of eccentricity fault or the turn-to-turn short circuit fault. Table 5.2 shows the classification results for eccentricity severities for both machines under two different loads at 30% and 60% of full load using FEA simulation. Table 5.3 shows the classification results for the turn-to-turn short circuit fault. For static eccentricity case,

the sample space consists of 33 samples for three different severities: 12%, 25%, and 45%. Each sample corresponds to a specific speed from 1000 rpm to 2000 rpm in steps of 100 rpm. A total of 3 classes assigned as follows: class 0 corresponds to 12% static eccentricity, class 1 corresponds to 25% static eccentricity and class 2 corresponds to 45% static eccentricity. For the turn-to-turn circuit fault, the sample space consists of 33 samples, corresponding to healthy case and two degrees of shorted turns: class 0 corresponds to healthy case, class 1 corresponds to 12% shorted conductors (one turn was shorted) and class 2 corresponds to 24% shorted conductors (two turns were shorted). The leave-one-out method was used to validate the results.

Table 5.2 LDA classification results to detect the severity of static eccentricity fault using FEA results. Each class contains 11 samples correspond to speeds $1000 - 2000$ rpm).

	Classification Results			
	Concentrated Winding		Distribution Winding	
	30% full load	60% full load	30% full load	60% full load
12% eccentricity	91%	100%	100%	91%
25% eccentricity	91%	100%	100%	100%
45% eccentricity	100%	100%	100%	100%

Table 5.3 LDA classification results to detect the severity of turn to turn short circuit fault using FEA results. (Each class contains 11 sample corresponds to speeds $1000 - 2000$ rpm).

	Classification Results			
	Concentrated Winding		Distribution Winding	
	30% full load	60% full load	30% full load	60% full load
Healthy	100%	100%	100%	91%
12.5% short circuit	91%	100%	91%	100%
25% short circuit	100%	100%	100%	100%

From the classification results, it is clear that LDA classification can be used for either

machine, to detect the type of fault and estimate its severity. However, some of the samples related to the 12% static eccentricity fault were not classified correctly, even though only simulation experiments were used that did not have measurement noise. The reason for that, because for low severities of eccentricity faults, most of the harmonic amplitudes for the 12% eccentricity were close to those for the healthy machine; hence the LDA classification cannot distinguish between healthy and the 12% static eccentricity fault for a few samples.

5.2.3 Comparing FEA with Experimental Data

To validate the proposed detection method, experimental data were collected for both machines under different faults. The experimental data for the distributed winding machine were carried out for healthy and two types of fault: static eccentricity with two severities (25% and 50%), and one turn-to-turn short circuit fault. The concentrated winding machine was tested under healthy and two severities of static eccentricity faults (25% and 50%).

The effects of both speed and torque were combined to evaluate the accuracy of LDA classification for fault detection and identification. First, the training samples and the testing samples were collected of the same torque. LDA was performed separately for samples collected from three torque levels ($20A$, $50A$ and $70A$). Each torque case contains a number of classes that define the machine health status. The sample space for each class contains 11 samples generated by varying the speed from 500 rpm to 1000 rpm in steps of 50 rpm, with a sampling frequency of $10kHz$ (10000 points were recorded for each sample ($1s$)). The leave-one-out method was used to test and validate the classification method. (Results are shown in Tables 5.4 and 5.5 for cases 1, 3 and 4).

In the second case, the training samples and the testing samples were collected using different torque levels. Two torques was tested: $30A$ and $100A$. In the $30A$ case, the testing

samples were collected while the machine is operating at a torque corresponding to $30A$ while the training samples were interpolated from samples collected from torques of $20A$, $50A$ and $70A$. The sample space for each class contains 11 samples generated by varying the speed from 500 rpm to 1000 rpm in steps of 50 rpm. The same procedure was followed for the $100A$ case and the results are shown in Tables 5.4 and 5.5 for cases 2 and 5).

Table. 5.4 shows a comparison of the classification results for fault detection between the experimental and FEA simulation for the distributed winding machine under healthy, 25% eccentricity fault and 12% short circuit fault. Table 5.5 shows a comparison of the classification results between the experimental and FEA simulation for the concentrated winding machine under healthy and two severities of eccentricity fault (25% and 50%). Table 5.6 shows a comparison of the classification results for fault severity detection between the experimental and FEA simulation for the distributed winding machine under two severities of eccentricity fault (25% and 50%).

Table 5.4 Comparison of LDA classification results between experiments and FEA to detect the fault type for the distributed winding machine. Each class contains 11 samples correspond to speeds $500 - 1000$ rpm).

Classification Results						
	Experimental results			FEA results		
case #	Healthy	25% eccentricity	One turn short	Healthy	25% eccentricity	One turn short
1-20A	91%	91%	100%	100%	100%	100%
2-30A	82%	82%	82%	91%	82%	91%
3-50A	91%	82%	91%	91%	91%	100%
4-70A	91%	82%	82%	90%	82%	82%
5-100A	72%	63%	72%	82%	72%	82%

The results show that the most accurate classification can be achieved when the testing and the training samples were collected from the same load. A minimum of 82% of the

Table 5.5 Comparison of LDA classification results between experiments and FEA for the concentrated winding machine. Each class contains 11 samples correspond to speeds $500 - 1000$ rpm).

Classification Results						
	Experimental results			FEA results		
case #	Healthy	25% eccentricity	One turn short	Healthy	25% eccentricity	One turn short
1-20A	100%	91%	100%	100%	100%	100%
2-30A	82%	72%	82%	91%	82%	91%
3-50A	91%	82%	91%	91%	91%	91%
4-70A	91%	82%	91%	91%	91%	91%
5-100A	72%	72%	72%	72%	72%	82%

Table 5.6 Comparison of LDA classification results between experiments and FEA to detect the fault severity for the distributed winding machine. Each class contains 11 sample corresponds to speeds $500 - 1000$ rpm).

Classification Results						
	Experimental results			FEA results		
case #	Healthy	25% eccentricity	50% eccentricity	Healthy	25% eccentricity	50% eccentricity
1-20A	91%	91%	91%	100%	91%	100%
2-30A	82%	82%	82%	91%	82%	91%
3-50A	91%	82%	82%	91%	91%	91%
4-70A	82%	82%	82%	91%	82%	82%
5-100A	72%	62%	82%	82%	82%	82%

samples were classified correctly. Interpolation for the training samples can be used if the testing samples were collected from a load close to the training samples load, but the accuracy decreases if the training samples were collected from loads that were too different from the testing samples loads. A minimum correct classification of 62% in the case of $100A$ was achieved to detect eccentricity fault. A minimum percentage of 72% achieved in the case of $30A$ for eccentricity fault detection.

To test the method over the operating range and not only at a specific torque, the entire

sampling space was modified to contain different torques and speeds. Tables 5.7 and 5.8 show a comparison of the correct classification results between experimental data and FEA of fault detection and classification for the distributed winding machine. The sample space for each class contains 40 samples, so a total of 120 samples were used to generate the training matrix. The 40 samples correspond to 4 different currents, each case contains 10 samples that were generated by varying the speed from 550 rpm to 1000 rpm in steps of 50 rpm. The combination of the amplitude of the first 15 harmonics were used as the features for the LDA classification; the leave-one-out method was used to validate the classification. Fig.5.5 shows the full training matrix construction for the healthy case and two different faults. Fig.5.6 shows the construction of the healthy portion of the full training matrix.

$$\left[\begin{array}{ccccc} x_1 1 & x_1 2 & x_1 3 & \cdots & x_1 15 \\ \vdots & \vdots & \vdots & & \vdots \\ x_{40} 1 & x_{40} 2 & x_{40} 3 & \cdots & x_{40} 15 \\ \hline x_{41} 1 & x_{41} 2 & x_{41} 3 & \cdots & x_{41} 15 \\ \vdots & \vdots & \vdots & & \vdots \\ x_{80} 1 & x_{80} 2 & x_{80} 3 & \cdots & x_{80} 15 \\ \hline x_{81} 1 & x_{81} 2 & x_{81} 3 & \cdots & x_{81} 15 \\ \vdots & \vdots & \vdots & & \vdots \\ x_{120} 1 & x_{120} 2 & x_{120} 3 & \cdots & x_{120} 15 \end{array}\right] \begin{array}{l} \left.\begin{array}{l} \\ \\ \\ \end{array}\right\} \text{H} \\ \left.\begin{array}{l} \\ \\ \\ \end{array}\right\} 25\%\ \text{ECC.} \\ \left.\begin{array}{l} \\ \\ \\ \end{array}\right\} 12\%\ \text{short} \end{array}$$

Figure 5.5 Full training matrix for healthy case and two faults (25% eccentricity and 12% turns of phase A shorted).

Table 5.7 A comparison of LDA classification results to detect the fault type for the distributed winding machine between experiments and FEA using the full training matrix.

Classification Results			
	Exp. using current	Exp. using voltage	FEA Data
Healthy	87.5%	85%	95%
25% eccentricity	85%	80%	88%
One turn short	88%	85.5%	92.5%

$$
\mathrm{H}\left\{\begin{array}{l}
\left[\begin{array}{ccccc}
x_1 1 & x_1 2 & x_1 3 & \cdots & x_1 15 \\
\vdots & \vdots & \vdots & & \vdots \\
x_{10} 1 & x_{10} 2 & x_{10} 3 & \cdots & x_{10} 15
\end{array}\right] \\
\left[\begin{array}{ccccc}
x_{11} 1 & x_{11} 2 & x_{11} 3 & \cdots & x_{11} 15 \\
\vdots & \vdots & \vdots & & \vdots \\
x_{20} 1 & x_{20} 2 & x_{20} 3 & \cdots & x_{20} 15
\end{array}\right] \\
\left[\begin{array}{ccccc}
x_{21} 1 & x_{21} 2 & x_{21} 3 & \cdots & x_{21} 15 \\
\vdots & \vdots & \vdots & & \vdots \\
x_{30} 1 & x_{30} 2 & x_{30} 3 & \cdots & x_{30} 15
\end{array}\right] \\
\left[\begin{array}{ccccc}
x_{31} 1 & x_{31} 2 & x_{31} 3 & \cdots & x_{31} 15 \\
\vdots & \vdots & \vdots & & \vdots \\
x_{40} 1 & x_{40} 2 & x_{40} 3 & \cdots & x_{40} 15
\end{array}\right]
\end{array}\right.
\begin{array}{l}
\left.\begin{array}{l} \\ \\ \end{array}\right\} 20\mathrm{A} \\
\left.\begin{array}{l} \\ \\ \end{array}\right\} 30\mathrm{A} \\
\left.\begin{array}{l} \\ \\ \end{array}\right\} 40\mathrm{A} \\
\left.\begin{array}{l} \\ \\ \end{array}\right\} 50\mathrm{A}
\end{array}
$$

Figure 5.6 Training matrix for healthy case only.

Table 5.8 A comparison of LDA classification results to detect the severity of eccentricity fault for the distributed winding machine between experiments and FEA using the full training matrix.

Classification Results			
	Exp. using current	Exp. using voltage	FEA Data
Healthy	85.5%	87.5%	91%
25% eccentricity	77.5%	80%	87.5%
50% eccentricity	80%	77.5%	90.5%

The results show that using the MSCA with the LDA as a classification method was able to detect the type of the fault and estimate the severity, either by using the harmonics of the phase voltages or of the current signals. When the training and testing features are extracted from samples collected at different operating loads, the classification result was not as accurate compared to the case when the samples are collected from the same operating torque. For fault detection, an average of 89.6% of the samples were classified correctly for the FEA samples, while 81% of the total samples were classified correctly from the experimental data using the harmonics in the measured feedback current, and 81.6%

were classified correctly based on the harmonics in the voltage signal.

In practical applications, tested machines might differ due to the manufacturing tolerance and the variations in the material properties. To evaluate the robustness of the detection methods, Additive White Gaussian Noise (AWGN) with different Signal to Noise Ration (SNR) levels was added to the tested current samples. A comparison of the classification results for fault detection between experimental and FEA is shown in Table 5.9. For this case, the sample space contains 30 samples corresponding to three classes: healthy, 25% static eccentricity and one turn-to-turn short circuit fault. Each class contains 10 samples generated by varying the speed from 550 rpm to 1000 rpm in steps of 50 rpm, with a sampling frequency of $10KHz$ for a current of $20A$. It is noted that the change in the harmonics amplitude due to the noise affects the classification results, which makes the detection based on the harmonics amplitude not robust at high noise levels.

Table 5.9 A comparison of LDA classification results for the distributed winding machine for different SNR levels. Each class 10 contains samples correspond to speeds $550 - 1000$ rpm).

Classification Results						
	Experimental results			FEA results		
SNR (dB)	H	25% eccentricity	One turn short	H	25% eccentricity	One turn short
100	90%	80%	90%	100%	100%	90%
90	90%	80%	90%	100%	100%	90%
80	88%	83%	85%	95%	92%	88%
70	80%	75%	79%	90%	86%	82%
60	70%	65%	71%	80%	70%	76%

5.2.4 Effect of Temperature

The change in the operating temperature causes multiple changes to the stator current and voltage. The increase of the operating temperature will cause an increase in the stator

phase resistance and a decrease in the magnet remanence flux. The effect of temperature is simulated by changing the values of the stator resistance and the magnet remanence flux based on (4.14) and (4.15).

Table 6.21 shows the simulation results of fault classification for fault detection under different temperatures. The sample space contains 40 samples corresponding to 4 classes: Healthy, 12% static eccentricity, 12% short circuit fault and 80% demagnetization. Each class consists of 11 samples generated by varying the speed from 1000 rpm to 2000 rpm in a steps of 100 rpm. The training samples were collected at an operating load of $20A$ at a temperature of 20^0C, while the testing samples were collected at a temperatures of $20^0C, 70^0C$ and 150^0C.

Table 5.10 LDA classification results for fault detection using FEA results. Each class contains 11 samples correspond to speeds $1000 - 2000$ rpm).

	Classification Results					
	Concentrated Winding			Distribution Winding		
	20^0C	70^0C	120^0C	20^0C	70^0C	120^0C
Healthy	100%	72%	63%	100%	72%	63%
12% eccentricity	91%	72%	55%	91%	72%	63%
12% short	100%	81%	63%	100%	81%	72%
80% demag.	100%	63%	55%	91%	55%	55%

It can be noticed that if the training samples were collected from an operating temperature that is close to the operating temperature of the testing samples, the classifier was able to detect the fault type. However, if the testing samples were collected from a different operating temperatures compared to the temperature at which the training samples were collected, the accuracy of the classifier reduced, especially for demagnetization fault because it is mainly related to temperature. A minimum percentage of 63% of the samples were classified correctly for the 70^0C case while a minimum correct classification percentage of

55% achieved for the 120^0C case.

Chapter 6

The Commanded Voltages Approach

Different faults in PMSMs will cause various and independent changes to the machine performance and parameters. These changes will be reflected in the machine flux linkages, which can be determined and measured from the machine voltages. This chapter shows how to use the commanded voltages as a method for fault detection and separation. The shift direction in the commanded d-axis and q-axis voltages can be used to detect the type of the fault, and the amount of the shift can be used to estimate the severity. This method can be applied during the normal operation of the machine, while the motor is running at steady state.

6.1 Variations of V_d and V_q Under Various Faults

6.1.1 V_d and V_q Variations Under Eccentricity Fault

It was shown in Chapter 2 and Chapter 4 that in the case of static eccentricity, the machine saturates earlier compared to the healthy machine. This early saturation is reflected as an increase in the total flux linkages in the machine. Fig.6.1 shows a comparison of the magnetic flux density for the FSCW machine between the healthy machine and a machine with 80% static eccentricity fault.

The increase in the machine flux density (in the zoomed region) can be noticed in the case of eccentric machine. Due to the nonlinearity of the machine, the increase in the magnetic

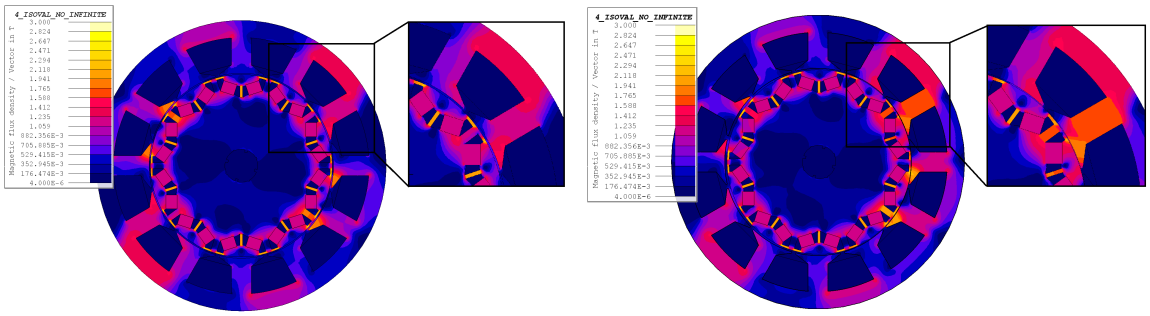

(a) Flux density for healthy machine

(b) Flux density for a machine with 80% eccentricity

Figure 6.1 Comparison of the magnetic flux density between a healthy machine and a machine with 80% eccentricity.

flux density, in the lower airgap region, will be larger than the decrease in the magnetic flux density, in the higher airgap region. This causes an increase in the total flux linkages in the machine. The increase in the total flux linkages increase the value of both λ_d and λ_q. Based on (2.11) and (2.12), increasing λ_d and λ_q, for the same operating load, increases V_d but decreases V_q. So in the case of an eccentricity fault, the point (V_d, V_q) in the V_d-V_q plane will shift toward the top left, and as the severity of eccentricity fault increases the point (V_d, V_q) shifts more to the top left of the curve.

6.1.2 V_d and V_q Variations Under Demagnetization Fault

In the case of partial demagnetization fault, a nonuniform magnetic flux density generates around the rotor, which causes a disturbance to the magnetic flux in the motor and reduce the total magnetic flux density generated from the magnets. Fig.6.2 shows a comparison of the magnetic flux line between healthy and the machine with Mag_1 demagnetized.

Demagnetizing one or more of the rotor magnets cause a decreasing in the total magnetic flux linkages (λ_{pm}). Based on (2.10), decreasing λ_{pm} causes a reduction in the total d-axis flux. Other effect of demagnetization fault is the change in the magnetic flux in the

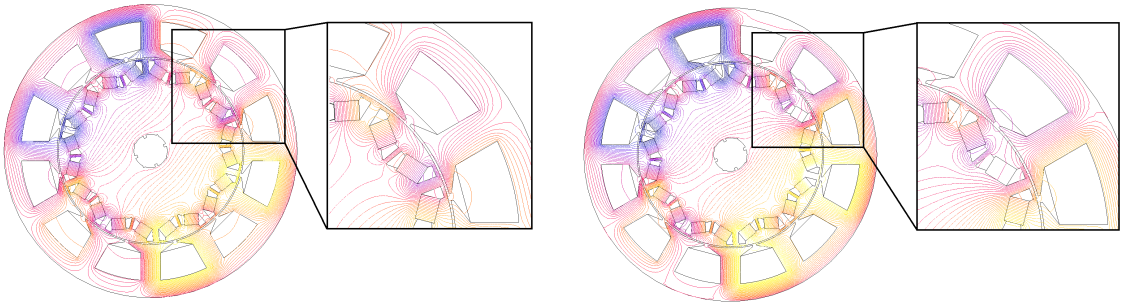

(a) Flux lines for healthy machine

(b) Flux lines for a machine with mag. 1 demagnetized

Figure 6.2 Comparison of the flux lines between healthy machine and a machine with one magnet fully demagnetized.

machine. The demagnetized region will have the same effect as an air region, forcing the flux to concentrate more in the q-axis of the machine. This increases the total q axis flux linkages in the machine. Based on (2.11) and (2.12), decreasing λ_d and increasing λ_q implies a decrease of both V_d and V_q compared to the healthy case. Therefore, in the case of demagnetization fault the point (V_d, V_q) in the V_d-V_q plane will shift toward the bottom left, and as the number of demagnetized magnets increases the shift in the point (V_d, V_q) will increase.

6.1.3 V_d and V_q Variations Under Turn-to-turn Short Circuit Fault

It was shown in (2.29)-(2.34) that in the case of turn-to-turn short circuit fault, the equivalent model for PMSM will contain two components: a healthy component and a variable component related to the short circuit fault. The variable component is related to the circulating short circuit current in the shorted turns. This current is can be approximated as a sinusoidal current and can be described as $i_f = |i_f| \cos(\theta + \phi_f)$, where $|i_f|$ is the magnitude of the short circuit current, and ϕ_f is the phase shift of the short circuit current. Based on this assumption, the variable component can be expanded to contain a DC component

and an oscillated component. The DC component of the d and q axes under steady state operation is given as:

$$v_{df,DC} = \frac{1}{3}\left(r_f|i_f|\sin(\phi_f) - \omega_e(M_{a_h a_f} + L_{a_f})|i_f|\sin(\phi_f)\right) \tag{6.1}$$

$$v_{qf,DC} = \frac{1}{3}\left(r_f|i_f|\cos(\phi_f) - \omega_e(M_{a_h a_f} + L_{a_f})|i_f|\cos(\phi_f)\right) \tag{6.2}$$

The short circuit current can be estimated using the following equation:

$$i_f = \frac{r_f i_a + e_f}{r_f + R_f} \tag{6.3}$$

where r_f is the equivalent resistance of the shorted turns, and R_f is value of the short resistance. It is noted from (6.1) and (6.2) that the DC component depends on the magnitude and the angle shift of short circuit current, which is determined by the severity of the short circuit fault. Fig.6.3 shows the short circuit current in the FSCW machine under different severities of turn-to-turn short circuit fault.

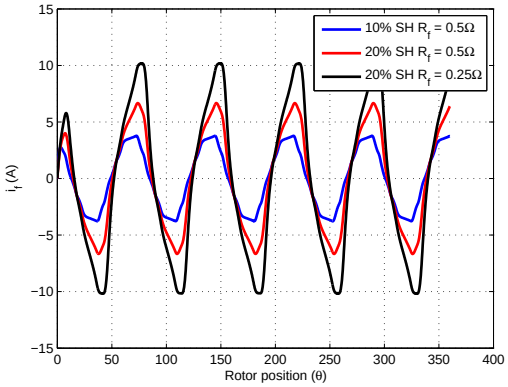

Figure 6.3 Short circuit current for the FSCW machine for different severities of short circuit fault.

As the severity of turn-to-turn short circuit fault increases, the magnitude of the short

circuit current and therefore the DC component in both the d and the q axes will increase as well. Increasing the DC components cases the value of the d and q voltages to increase too. The effect of short circuit fault can also be observed using the change in the magnetic flux density and flux lines. Fig.6.4 shows a comparison of the flux density and the flux lines between healthy machine, and a machine with 20% of the turns of phase A coil conductors are shorted.

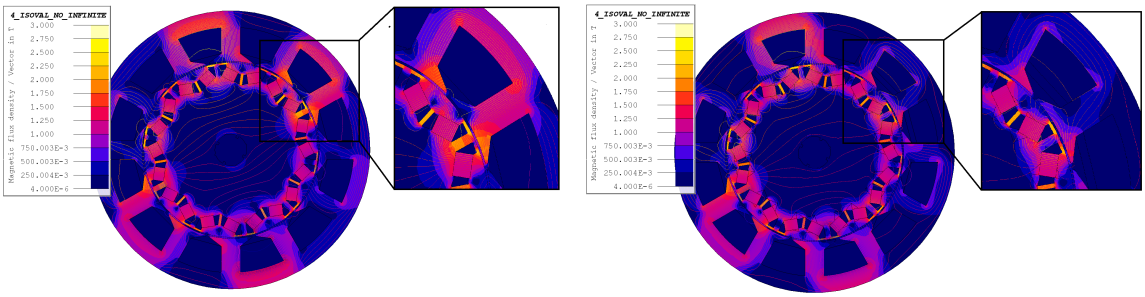

(a) Flux density and flux lines for a healthy machine

(b) Flux density and flux lines for 20% short circuit fault

Figure 6.4 Comparison of the flux density between a healthy machine and a machine with 20% of the turns in phase A conductors are shorted.

Under turn-to-turn short circuit fault, the total flux density decreases in the shorted region (the zoomed region), this means a decrease in the value of λ_q. However, in the short region, more flux lines are closing in the d-axis of the machine causing an increase in λ_d. Decreasing λ_q and increasing λ_d increases the value of V_d and V_q. Therefore, in the case of short circuit fault, the point (V_d, V_q) shifts towards the top right in the V_d-V_q plane. It is noticed that turn-to-turn short circuit fault depends on the number of the shorted turns and the values of the shorted resistance. As the number of shorted turns increases or the value of the shorted resistance decreases, the values of V_d and V_q increases more.

Fig.6.5 summarize the change in the commanded voltages under different faults compared to the healthy case.

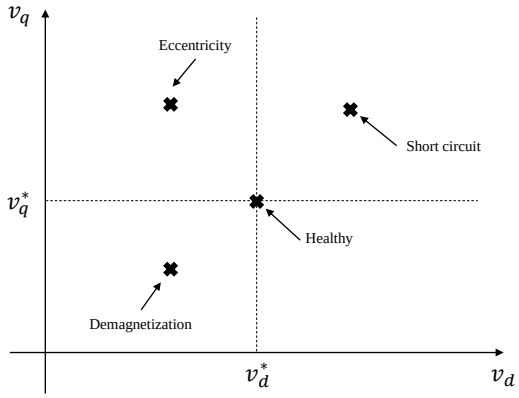

Figure 6.5 The shift in the commanded voltages under the tested faults

6.2 Numerical And Experimental Results

The tests were applied while the motors were operating at steady state with rated torque. To find the operating conditions when the machine is operating at this torque, the machine needs to be characterized (i.e. finding the value of the machine d and q axes inductances under different operating conditions). Following the characterization method discussed in chapter 2, the simulation results for the torque, λ_d, and λ_q versus the current angle (δ) at different current loads for the FSCW machine is shown in Fig.6.6

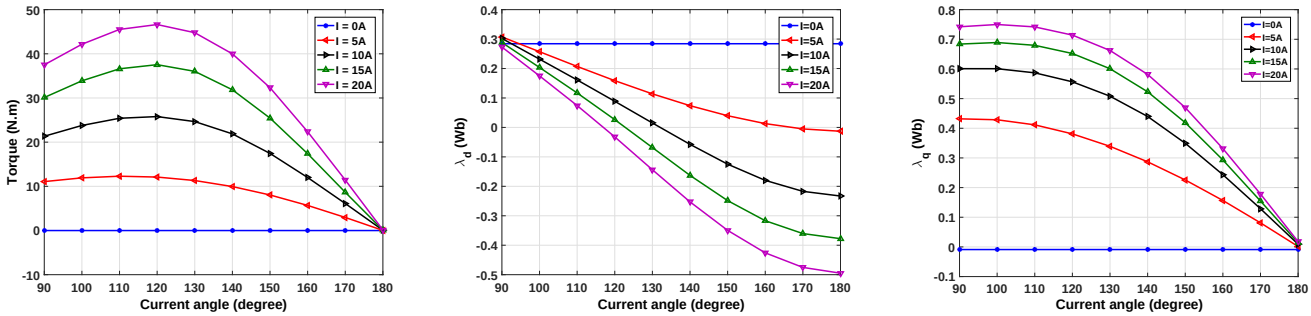

(a) Torque vs δ (b) λ_d vs δ (c) λ_q vs δ

Figure 6.6 Simulation results for the characterization of the FSCW machine under different operating loads at a speed of $300rpm$

The maximum torque was achieved at an operating angle $\delta = 120°$. Therefore, all the

tests will be applied at a control angle of 120°.

6.2.1 Static Eccentricity Fault Results

Fig.6.7 shows the simulation results for the variation in λ_d and λ_q for different severities of eccentricity faults compared with the healthy machine. The machine was running at a speed of $300rpm$ and the applied current was $5A$ at an angle of 120° ($i.e. I_q = 4.33A, I_d = -2.5A$). As discussed in Section 6.1.1, the extra saturation due to the shift in the stator geometry will bring up the values of λ_d and λ_q relative to a healthy machine.

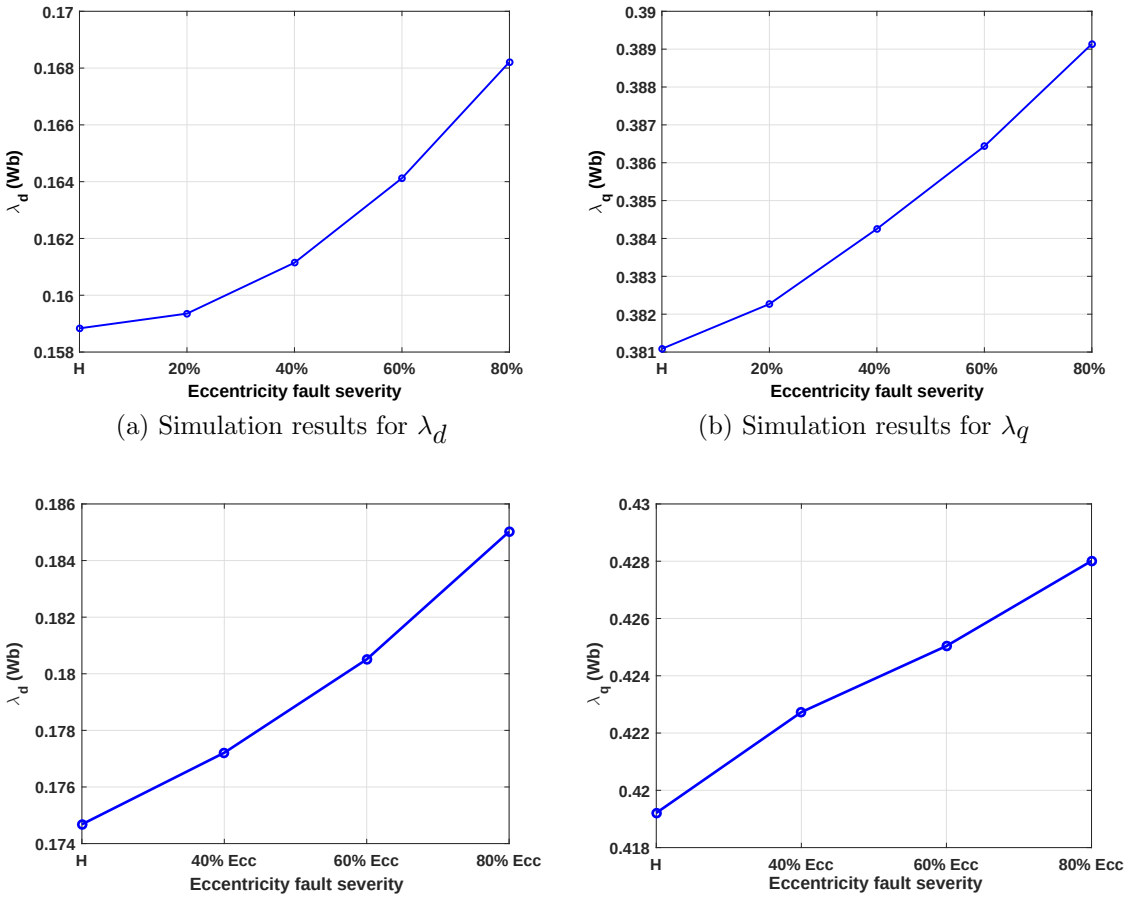

(a) Simulation results for λ_d

(b) Simulation results for λ_q

(c) Experimental results for λ_d

(d) Experimental results for λ_q

Figure 6.7 λ_d and λ_q for healthy and different severities of eccentricity fault at I = 5A and $\delta = 120°$

Fig.6.8 shows the change in the values of V_d and V_q for the FSCW machine under different severities of static eccentricity compared to the healthy case. It can be noted that in the case of eccentricity fault, the value of V_d decreases, and the value of V_q increases, moving the point (V_d, V_q) to the upper left in the V_d-V_q plane. The change in V_d and V_q depends on the severity of eccentricity fault. As eccentricity becomes more severity, the point (V_d, V_q) shifts more to the upper left in the V_d-V_q plane.

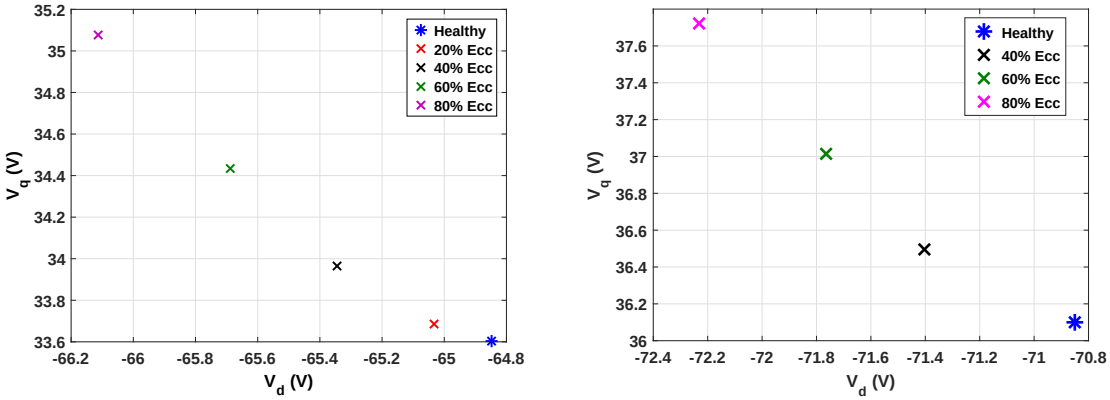

(a) Simulation results V_d vs V_q

(b) Experimental results V_d vs V_q

Figure 6.8 Simulation and experimental results for the change in V_d and V_q for healthy and different severities of static eccentricity fault at I = 5A and $\delta = 120°$

6.2.2 Partial Demagnetization Fault Results

Three levels of partial demagnetization fault were tested for the FSCW machine using simulations and experimental tests. Fig.6.9 shows a comparison of the variation in λ_d and λ_q between simulations and experimental data. The machine was operated at a speed of $300rpm$ and the current applied is $10A$ at an angle of 120°.

Fig.6.9 shows that both simulation and experimental results exhibit the same behavior. The value of λ_d decreases, but the value of λ_q increases. This decreases the value of V_d and V_q moving the point (V_d, V_q) to the bottom left of the V_d-V_q plane. Fig.6.10 shows a

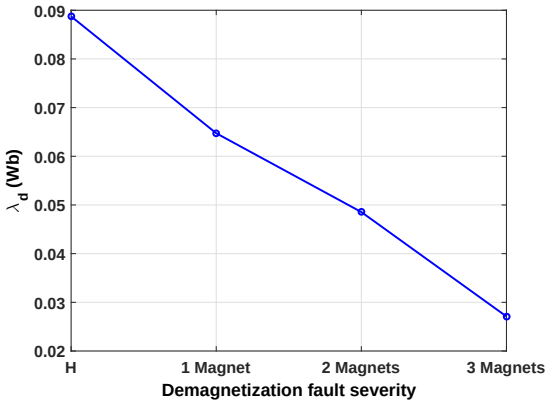

(a) Simulation results for λ_d

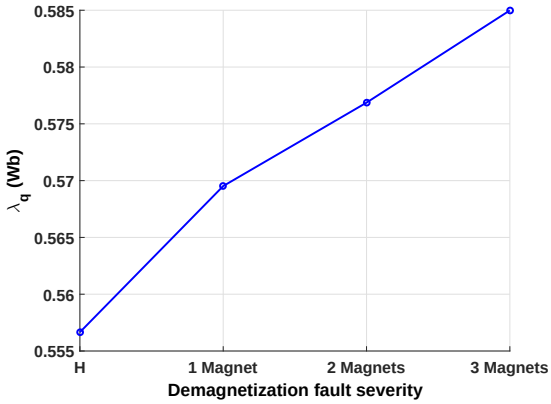

(b) Simulation results for λ_q

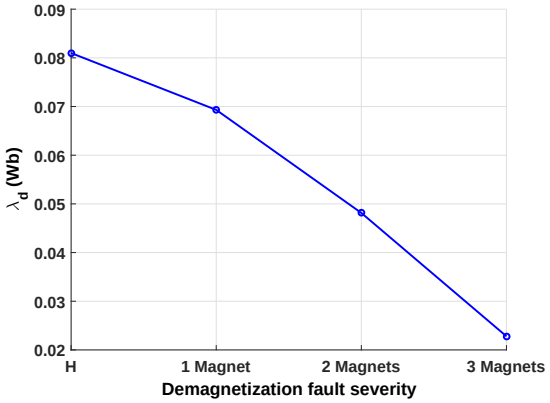

(c) Experimental results for λ_d

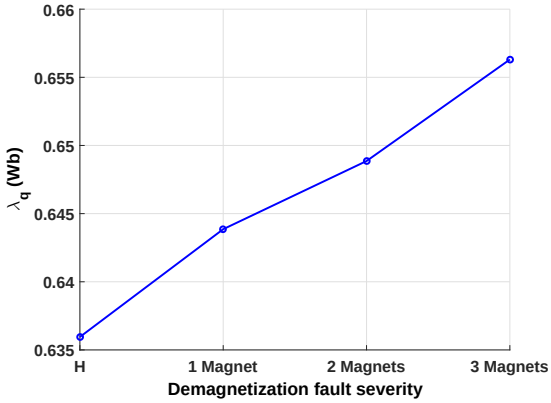

(d) Experimental results for λ_q

Figure 6.9 Simulations and experimental results for λ_d and λ_q for the FSCW machine under healthy and 3 levels of demagnetization fault (1, 2 and 3 magnets) at I = 10A and $\delta = 120°$

comparison between simulations and experimental results for the change in V_d and V_q under healthy and three severities of partial demagnetization faults.

6.2.3 Turn-to-turn Short Circuit Fault Results

Simulations and experimental tests were performed on two levels of turn-to-turn short circuit fault: 10% and 20% of the total turns of phase A conductors. To vary the severity of each level, two different shorted resistances were used (0.5 Ω and 0.25 Ω, which is equal to 33.3% and 16.6% of the stator resistance respectively). Fig.6.11 shows the variation in λ_d and λ_q

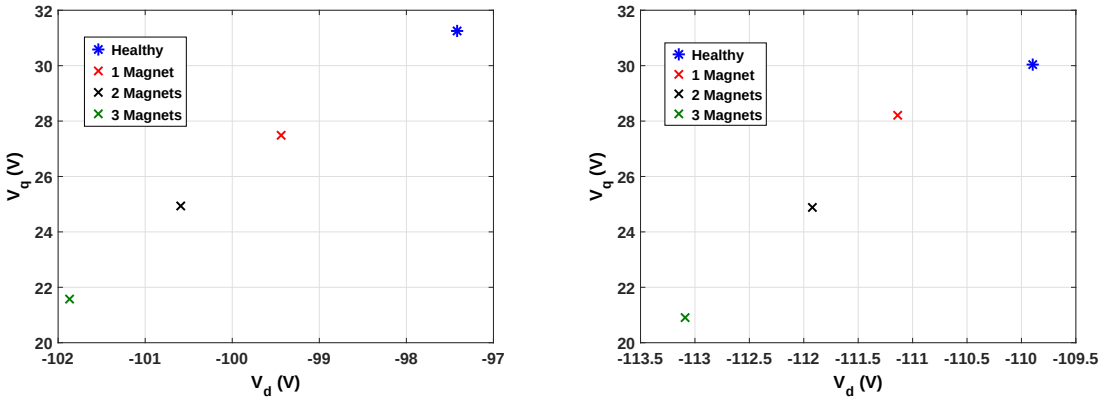

(a) Simulation results V_d vs V_q

(b) Experimental results V_d vs V_q

Figure 6.10 Simulation and experimental results for the change in V_d and V_q for healthy and 3 levels of demagnetization fault at I = 10A and $\delta = 120°$

for the tested turn-to-turn short circuit fault. The machine was operated at a speed of 300 rpm and the current applied was $10A$ at an angle of 120°.

In the case of short circuit fault, the value of λ_d increases, but the value of λ_q decreases, which causes an increasing in both V_d and V_q; this shifts the (V_d, V_q) point in the V_d-V_q plane to the upper right as shown in Fig.6.12.

Based on the previous results, the shift direction of the point (V_d, V_q) can be used as an indicator to detect the type of fault and also estimate the severity. In the case of an eccentricity fault, the point (V_d, V_q) shifts towards the upper left of the plane; in the case of partial demagnetization fault, the point (V_d, V_q) shifts towards the bottom left of the plane; and for turn-to-turn short circuit fault, the point (V_d, V_q) shifts towards the upper right of the plane. Fig.6.13 compares the results between simulations and experimental results that summarize the change in the point (V_d, V_q) at different fault types and severities, for two torques ($I = 5A$ and $I = 10A$) at an angle of $\delta = 120°$ running at a speed of $300rpm$.

It can be noted from Fig.6.13 that as the current increases, it became harder to detect eccentricity fault. As the applied current increases, the saturation in the machine from

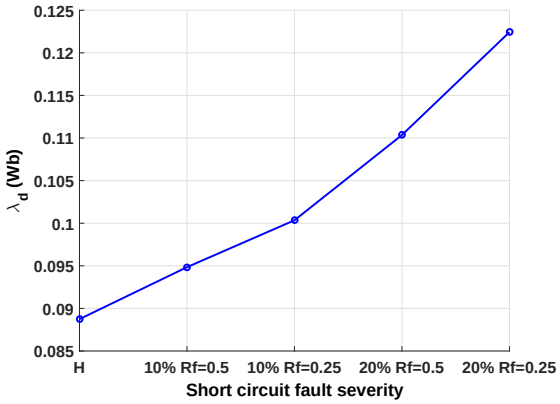

(a) Simulation results for λ_d

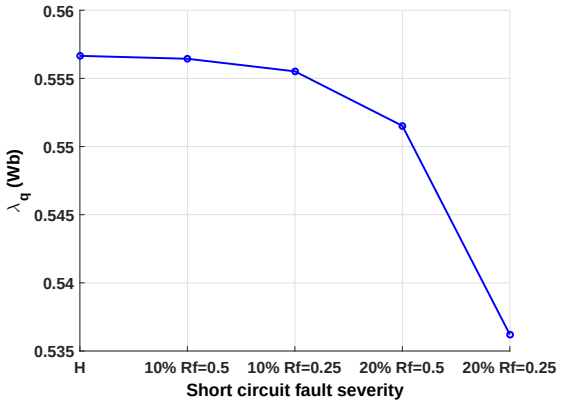

(b) Simulation results for λ_q

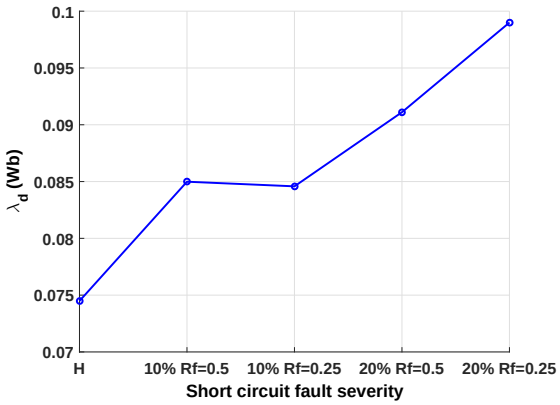

(c) Experimental results for λ_d

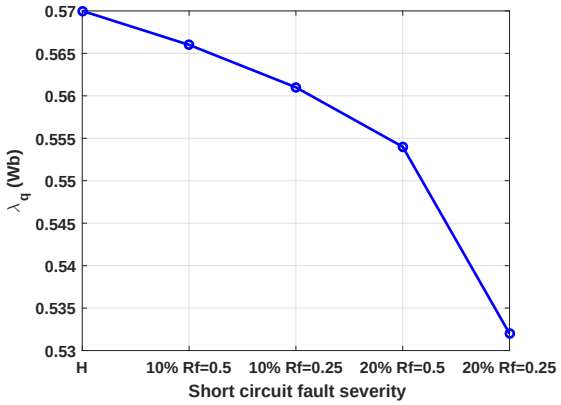

(d) Experimental results for λ_q

Figure 6.11 Simulations and experimental results for λ_d and λ_q under healthy and 2 levels of turn-to-turn short circuit fault at I = 10A and $\delta = 120^\circ$

the stator flux will mask the effect of the extra saturation from eccentricity fault makes it harder to observe the shift in V_d and V_q. However, for partial demagnetization and short circuit faults, the shift in V_d and V_q can still be observed even at high currents using both simulations and experimentally. Table6.1 summarize the changes in the d and q axis voltages under different faults and severities while the machine was operating at a speed of $300rpm$ and a current of $5A$ at an angle of 120^0.

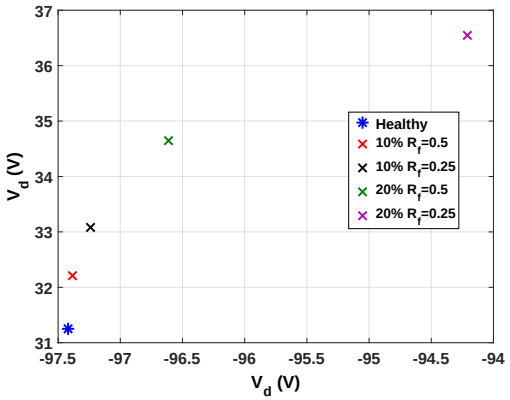

(a) Simulation results V_d vs V_q

(b) Experimental results V_d vs V_q

Figure 6.12 Simulation and experimental results for the change in V_d and V_q for healthy and 2 levels of short circuit fault at I = 10A and $\delta = 120°$

Table 6.1 Simulation and the experimental results for V_d and V_q for the FSCW machine under different faults

	FEA Simulation		Experimental	
Fault Type	Vd	Vq	Vd	Vq
Healthy	-64.8	33.6	-78.9	44.6
20% Eccentricity	-65	33.6	-	-
40% Eccentricity	-65.3	33.9	-	-
60% Eccentricity	-65.6	34.4	-	-
80% Eccentricity	-66.1	35	-	-
1 Magnet Demag.	-66.3	30	-81.6	40
2 Magnets Demag.	-67.7	27.9	-81.9	31.5
3 Magnets Demag.	-69.2	24.2	-82.7	28.6
10% Short Rf = 0.5	-64.3	34.5	-75.3	52.9
10% Short Rf = 0.25	-63.5	35.2	-71.9	52
20% Short Rf = 0.5	-61.8	35.7	-70.6	53
20% Short Rf = 0.25	-59.1	35.3	-68.7	53.7

6.2.4 Effect of Magnet Angle

Fig.6.14 shows the simulation results for the shift in the d and q voltages for the concentrated winding machine under healthy, and the three tested machine. The same shift behaviour in the commanded voltages can be observed in the static eccentricity and turn-to-turn short

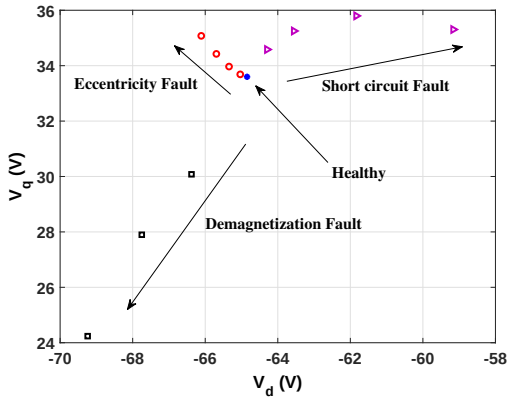

(a) V_d vs V_q simulation results $I = 5A, \delta = 120^\circ$

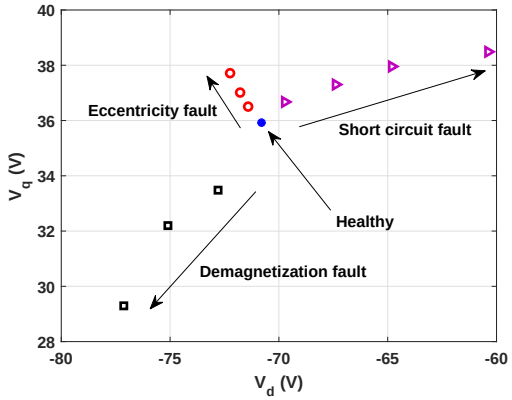

(b) V_d vs V_q experimental results $I = 5A, \delta = 120^\circ$

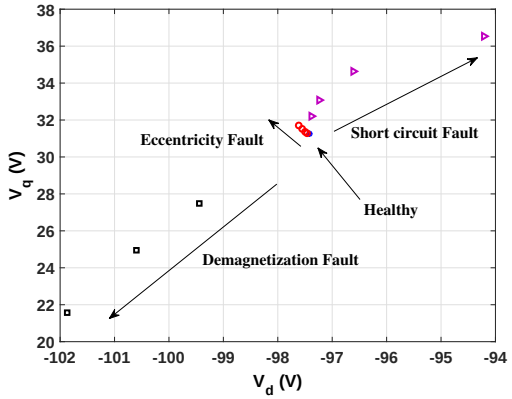

(c) V_d vs V_q simulation results $I = 10A, \delta = 120^\circ$

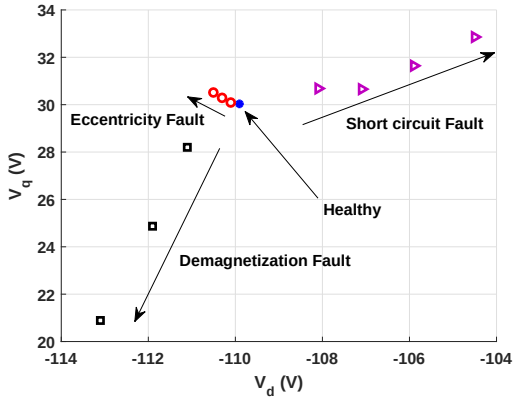

(d) V_d vs V_q experimental results $I = 10A, \delta = 120^\circ$

Figure 6.13 Simulation and experimental results for the change in V_d and V_q for healthy and different faults for I = 5A, $\delta = 120^\circ$ and I = 10A, $\delta = 120^\circ$

circuit faults. However, for partial demagnetization the shift in the commanded voltages was mainly in the q axis voltage but not in the d axis.

The behaviour of the reduction in the q-axis voltage is similar to the case of the FSCW machine. However, the d-axis voltage increased which is opposite to the case of the FSCW machine. This is due to the magnets rotation angle. In the case of partial demagnetization, the demagnetized magnet will have properties similar to the air that block the flux lines path. If the magnets are not rotated (as in the case of the concentrated winding machine), the flux lines will pass through the back iron of the rotor causing a decrease in λ_q and therefore

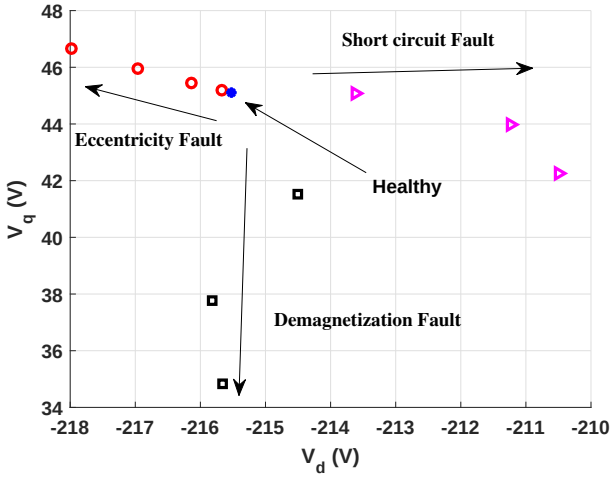

Figure 6.14 Simulation results for the change in V_d and V_q for healthy and the three tested faults for the concentrated winding machine for I = 75A and $\delta = 120°$

increase in V_d. However, if the magnets are rotated, the demagnetized magnets will block the path of the flux lines and push them toward the q-axis of the machine. This causes an increase in λ_q and therefore decrease in V_d. To study the effect of the magnet rotation angle, the rotor geometry for the concentrated winding machine was modified by rotating the magnet angle at different degrees. Fig.6.15 shows the modification in the magnet placement of one pole of the rotor magnets and Fig.6.16 shows the cross geometry for the original concentrated winding machine and the modified rotor magnets for 0, 10, and 20 rotation angles.

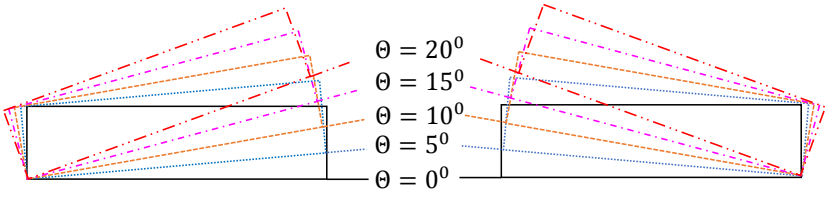

Figure 6.15 Single pole magnet rotation of the concentrated winding machine

Fig.6.17 shows a comparison of the flux lines, for the concentrated winding machine,

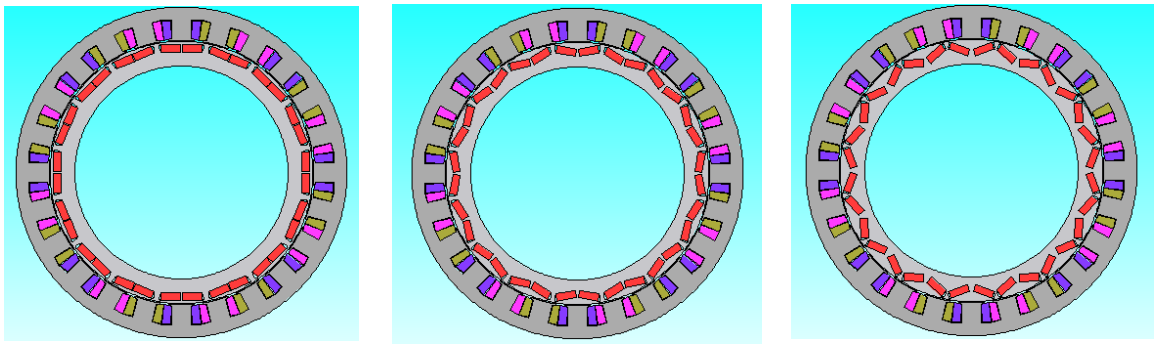

(a) $\Theta = 0^0$ (b) $\Theta = 10^0$ (c) $\Theta = 20^0$

Figure 6.16 Modified magnets for the concentrated winding machine

between a zero rotation angle and 15^0 rotation angle under one magnet fully demagnetized.

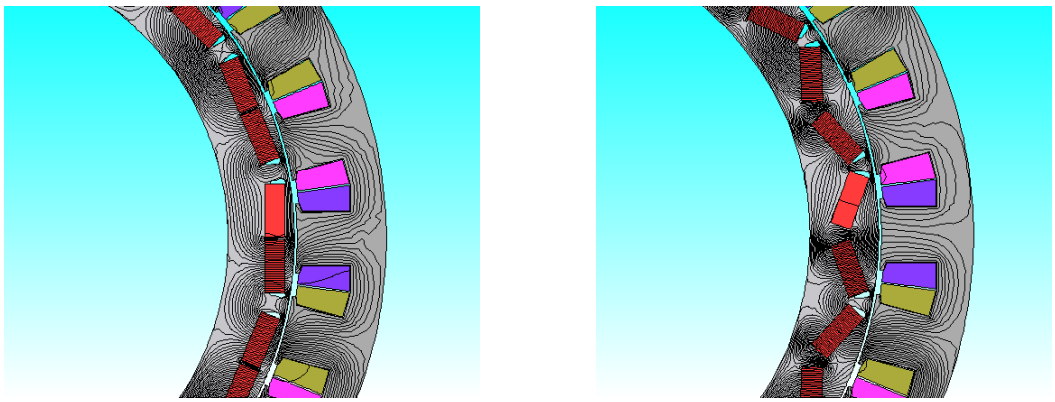

(a) $\Theta = 0^0$ (b) $\Theta = 15^0$

Figure 6.17 Comparison of the flux lines for 0^0 and 15^0 magnet rotation angle under demagnetization faut

Fig.6.18 shows a comparison of the shift in V_d and V_q for the concentrated winding machine under healthy and different severities of demagnetization fault for the different magnet rotation angles. It can be noted that the value of Vq does not change for all the cases as expected. The only change is in the value of V_d which is due to the change in the flux concentration due to the magnet rotation angle.

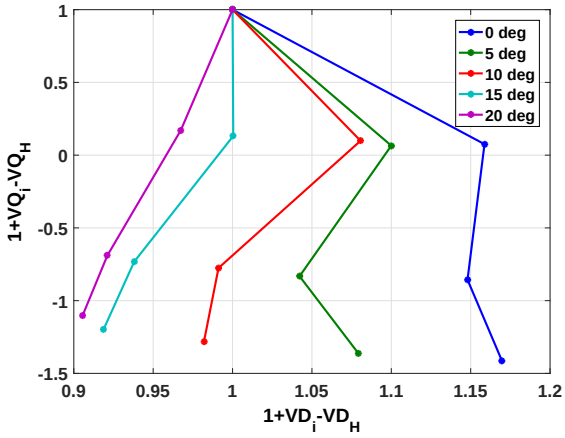

Figure 6.18 The effect of the magnet rotation on V_d and V_q for the concentrated machine under healthy and demagnetization fault

The rotation of the magnet angle will also affect the change V_d and V_q under eccentricity fault. When the magnets are rotated, the flux will have more steel to pass through. This reduces the saturation in the rotor steel compared to the case when the magnet are not rotated. In this case, the extra saturation in the machine due to eccentricity fault will be more noticeable and the effect of the extra saturation can be more noticable with the rotated magnets compared to original magnets position. Therefore, the increase in λ_d and λ_q will be higher in the case of rotated magnets compared to the non rotated magnets for eccentric machine. The increase in λ_d and λ_q implies that the increase in V_q and the decrease in V_d will be more in the case of rotating magnets. Fig.6.19 shows a comparison of the shift in V_d and V_q for the concentrated winding machine under healthy and different severities of eccentricity fault for the different magnet rotation angles, the motor was operating at a speed of $2000rpm$ and the applied current is $75A$.

It can be noted from Fig.6.19 that the change in the saturation affect both V_d and V_q, but it wont change the directing of the shift. In all cases, the point (V_d, V_q) was shifted to the top left of the V_d-V_q plane, but the amount of the shift was higher in the case of rotated

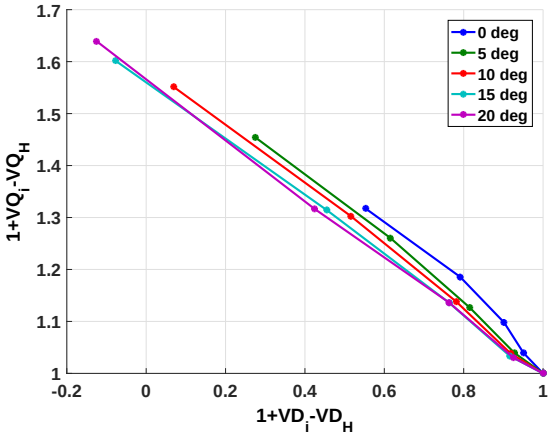

Figure 6.19 The effect of the magnet rotation on V_d and V_q for the concentrated machine under healthy and eccentricity fault

magnets compared to non rotated magnets.

6.2.5 Effect of Speed and Temperature

The operating speed and temperature of PMSM will change frequently. Therefore, it is important to validate the separation method under different operation speeds and temperature. Three speeds were simulated for the FSCW machine using FEA ($300rpm$,$500rpm$ and $600rpm$). For each speed the commanded voltages (V_d and V_q) were measured under different loads. Fig.6.20 shows the simulation results for the variation in the FSCW machine voltages V_d and V_q under healthy and the three tested faults.

The change in the machine operating temperature causes a change in the machine voltages due to the change in the stator resistance and the change of the magnet remanent flux with temperature. The increase in the temperature was simulated in FEA by changing the phase resistance and the magnet remanence as in (4.14) and (4.15). Fig.6.21 shows the simulation results for the effect of the temperature increase on the d and q axis voltages for healthy the three different faults. Table 6.2 summarize the change in the commanded voltages for the

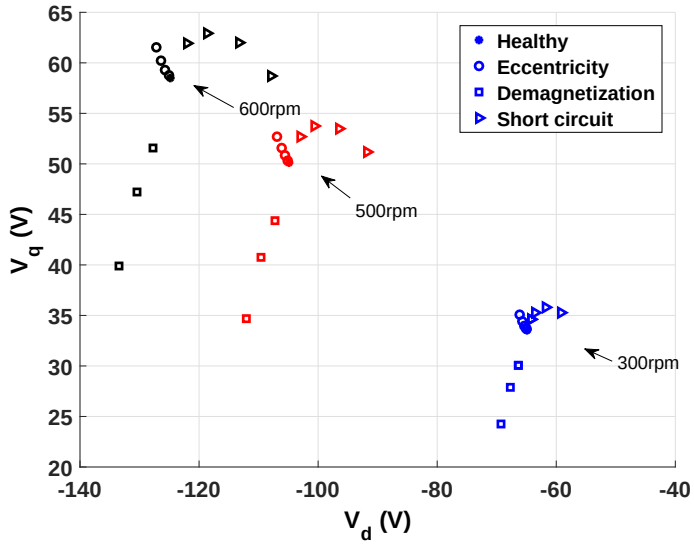

Figure 6.20 Simulation results for the change of V_d vs V_q for the FSCW machine under healthy and three different faults under two speeds $300rpm$,and $500rpm$ ($I = 5A, angle = 120^0$ and temp $= 20^0C$)

three faults under different operating temperatures.

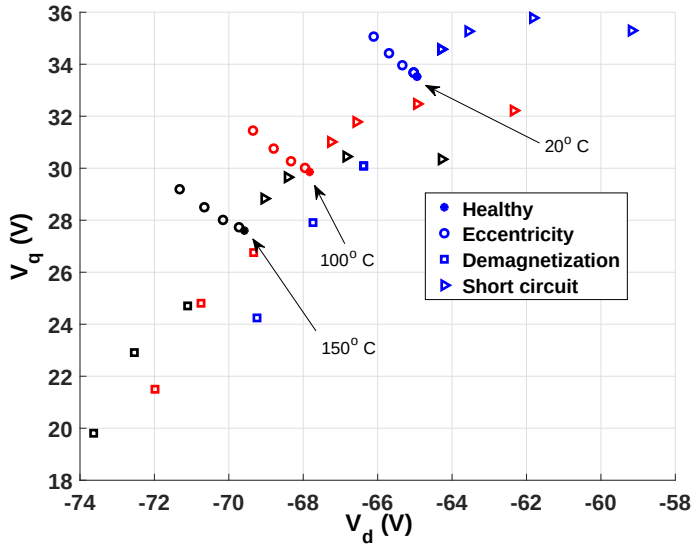

Figure 6.21 Simulation results for the change of V_d vs V_q for the FSCW machine under healthy and three different faults under three temperatures 20^0C, 100^0C and 150^0C ($I = 5A, angle = 120^0$ and speed $= 300rpm$)

It can be noted from Fig.6.20 and Fig.6.21 that the change in the speed and temperature shifts the value of both the d and the q axis voltages, which might decrease the accuracy of

Table 6.2 Comparison for the simulation results for V_d and V_q for the FSCW machine under different faults and operating temperatures

	20^0C		100^0C		150^0C	
Status	Vd	Vq	Vd	Vq	Vd	Vq
Healthy	-64.9	33.5	-67.8	29.8	-69.5	27.6
20% eccentricity	-65	33.6	-67.9	30	-69.7	27.7
40% eccentricity	-65.3	33.9	-68.3	30.2	-70.1	28
60% eccentricity	-65.9	34.4	-68.7	30.7	-70.6	28.4
80% eccentricity	-66.1	35	-69.3	31.4	-71.3	29.2
1 Magnet demag.	-66.3	30	-69.3	26.7	-71.1	24.7
2 Magnets demag.	-67.7	27.9	-70.7	24.8	-72.5	22.9
3 Magnets demag.	-69.2	24.2	-71.9	21.4	-73.6	19.8
10% short R f = 0.5Ω	-64.3	34.5	-67.2	31	-69	28.8
20% short Rf = 0.5Ω	-61.8	35.7	-64.9	31.4	-66.8	30.4
10% short Rf = 0.25Ω	-63.5	35.2	-66.5	31.7	-68.4	29.6
20% short Rf = 0.25Ω	-59.1	35.3	-62.3	32.2	-64.2	30.3

the detection method; however the shift of the (V_d, V_q) point caused by the different faults shows the same behaviour under different temperatures.

6.3 Fault Detection and Separation Algorithm

6.3.1 Proposed Detection Method

The shift in the voltages (V_d and V_q) under different faults is consistent for different operating loads, speeds and temperatures. Therefore, the shift in the commanded voltages can be used as a detection method to detect the fault type and estimate its severity. However, the machine operates at different operating and environmental conditions. Therefore, it is important to account for the changes in the commanded voltages using these factors into consideration. Fig.6.22 shows a block diagram of the proposed detection and separation method using the commanded voltage approach.

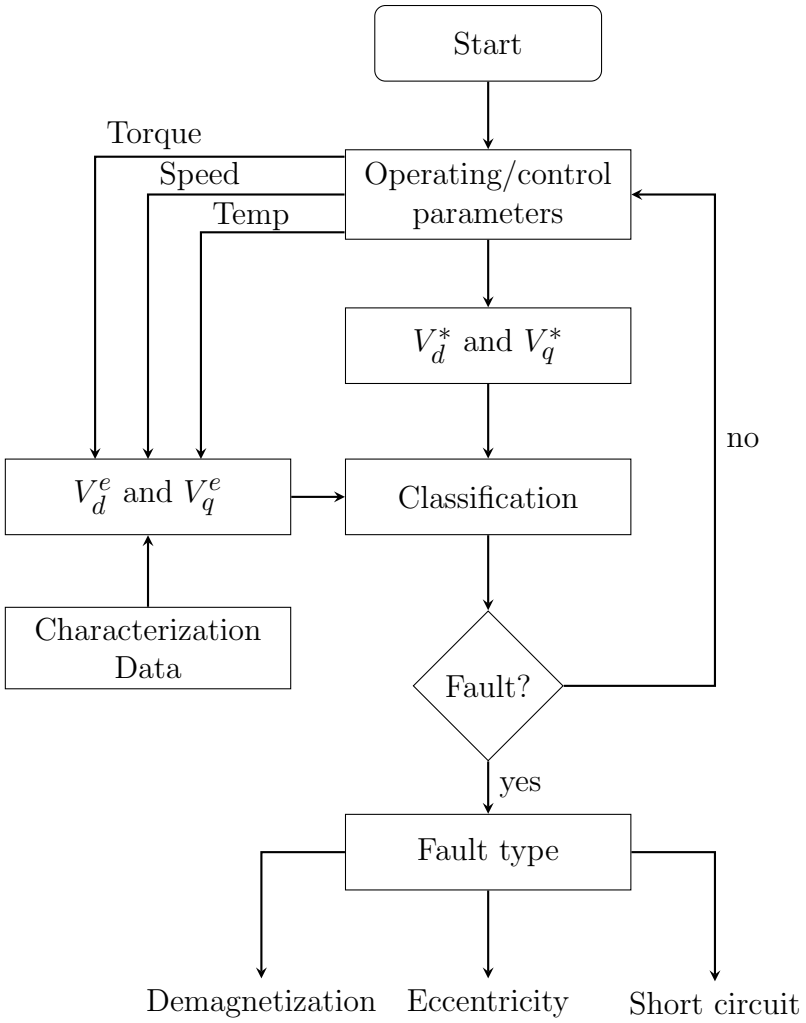

Figure 6.22 Block diagram for fault detection and separation using the commanded voltages

The following detection method is proposed:

- The motor needs to be characterized first to generate the motor flux linkages maps as shown in Fig.6.6b and Fig.6.6c. These maps can be used as a lookup table to estimate the d and q inductances at any different operating point.

- At any operating point the value of the motor commanded voltages can be estimated as follows:

– The angular speed ω_{ee} is calculated from the measured speed as follow:

$$\omega_{ee} = Speed * \frac{2\pi}{60} * P \tag{6.4}$$

– The motor inductances (L_d and L_q) are estimated using the operating torque from the lookup tables. An spline interpolation is used to estimate the value of (L_d and L_q) if the machine is operating at a torque that is not tested during the motor characterization.

– The operating temperature affects the stator resistance and the magnet permeance flux. The increase in the stator resistance and the decrease in the magnet permeance flux can be estimated as follows:

$$R_{ST} = R_{s0}\left[1 + \alpha_R(T - T_0)\right] \tag{6.5}$$

$$\lambda_{pmT} = \lambda_{pm0}\left[1 - \alpha_{Br}(T - T_0)\right] \tag{6.6}$$

– The estimated commanded voltages are estimated using the following equations:

$$V_d^e = R_{sT}.I_d - Ł_q I_q \omega_{ee} \tag{6.7}$$

$$V_q^e = R_{sT}.I_q + \left[\lambda_{pmT} + L_d I_d\right]\omega_{ee} \tag{6.8}$$

- The measured voltages of the machine is recorded and comparing to the estimated voltages. These voltages can be used a classification features. The classifier output defines the machine health status (whether it is healthy or faulted), and by using the voltages shift direction, the fault type can be detected and the severity can be

estimated.

In order to have a high classification accuracy, it is important for the voltages to be estimated correctly to the actual measured voltages. Fig.6.23 shows a comparison between the actual and the estimated voltages for the FSCW machine under different operating conditions. The FSCW machine was first characterized using 6 different operating torques (0, 2, 5, 10, 15 and 20A) at a speed of 300rpm, and for an operating temperature of 20^0C. The estimated voltages were calculated at different speeds, loads, and temperatures. Interpolation using spline interpolation was performed to estimate the d and q inductances.

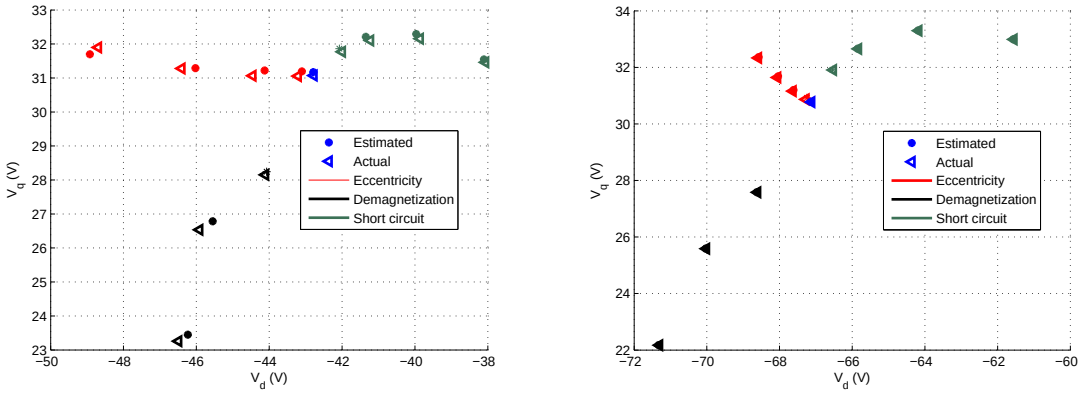

(a) 3A 120^oC and 300rpm (b) 5A 80^oC and 300rpm

Figure 6.23 Comparison between actual and estimated commanded voltages under different operating conditions

The results shows that the proposed method is able of estimating the machine voltages correctly for different operating load, speed, and temperature. It is also shown that the effect of the speed and temperature can be adjusted analytically, which reduce the number of variation parameters to only the current. However, the accuracy of the estimated voltages depends on the number of samples in the lookup tables, the higher the number of characterization tests, the more accurate the estimation.

6.3.2 Classification Implementation

To have an accurate results for detecting the fault the type and severity, a classification method is needed. Two features were extracted from each case: the d-axis voltage and the q-axis voltage. The actual commanded voltages at different operating condition is used as the testing samples. For every testing sample, the training samples were generated by calculating V_d^e and V_q^e around that tested sample operating condition. The variation was chosen to be 10%. For example if the testing sample collected for a machine operating at a speed of $200rpm$, a torque of $10A$, and a temperature of 20^0C, the training training samples is calculated for all the speeds from $190rpm$ to $210rpm$, for each speed the loads is varied from $9.5A$ to $10.5A$, and the temperature is varied from 19^0C to 21^0C. A total of 1000 combination samples can be generated as a training samples for each testing sample.

For the concentrated winding machine, 11 cases were generated using FEA. One case corresponds to the healthy conditions, four cases correspond to static eccentricity fault, generated by varying the severity from 20% to 80% in steps of 20% of the airgap length, three cases corresponds to partial demagnetization fault, by demagnetized 1, 2 and 3 consecutive magnets, and three cases represent turn-to-turn short circuit fault (12.5% and 25% and 62.5% of the turns in phase A are shorted). The machine was first characterized at a speed of $500rpm$, the operating temperature is 20^0C and the current was varying from $0A$ to $150A$ in steps of $10A$. The characterization data can be used to generate the lookup tables for the flux linkages. These lookup tables were used to estimate the flux linkages for the training samples. The testing samples were collected from speeds of $500rpm$ and $1000rpm$ at an operating temperatures of 20^0C, 100^0C, and 150^0C with loads of $10A$, $50A$, and $100A$. 18 samples were generated as a testing samples for each health status (a total of 198 testing

samples), and for each testing sample a 1000 samples were generated as a training samples.

For the FSCW machine 11 cases were generated using FEA, one for healthy, 3 for eccentricity fault (40%-80% in steps of 20%), three cases for demagnetization by demagnetizing 1, 2, and 3 adjacent magnets, and 4 cases represent short circuit fault (10% with $R_f = 0.5$, 12% with $R_f = 0.25$, 20% with $R_f = 0.5$, and 20% with $R_f = 0.25$). The machine was characterized at a speed of $300rpm$, the operating temperature is 20^0C and the current was varied from $0A$ to $20A$ in steps of $5A$. The testing samples were collected from speeds of $300rpm$ and $500rpm$ at an operating temperatures of 20^0C, 100^0C, and 150^0C with loads of $2A$, $3A$, $5A$, $8A$, and $10A$. 36 samples were generated as a testing samples for each health status (a total of 432 testing samples), and for each testing sample a 1000 samples were generated as a training samples. Experimental tests were performed for the FSCW machine under healthy and the tested faults with the same severities. The testing samples for the experimental data were collected from speeds of $300rpm$ and $500rpm$ at an operating temperatures of 20^0C with loads of $2A$, $3A$, $5A$, $8A$, and $10A$. 10 samples were generated as a testing samples for each health status (a total of 110 testing samples), and for each testing sample a 1000 samples were generated as a training samples.

6.3.3 Classification Results

Table 6.3 shows the classification results of fault detection and separation for the concentrated winding machine using three classifiers (KNN, LDA, and QDA). Table 4.2 shows a comparison of the classification results the classification results of fault detection and separation between simulations and experimental data for the FSCW machine using the commanded voltages approach.

Table 6.5 summarizes the the average classification results of fault detection and sepa-

Table 6.3 Classification results for the concentrated winding machine

	Concentrated winding machine		
Machine Status	K-NN	LDA	QDA
Healthy	80%	83%	82%
20% ECC	75%	79%	78%
40% ECC	80%	80%	82%
60% ECC	78%	79%	78%
80% ECC	79%	81%	80%
1 Magnet	88%	88%	86%
2 Magnets	89%	91%	90.5%
3 Magnets	91.5%	93%	91.5%
12.5% Short	82%	88%	85%
25% Short	87%	90%	90%
50% Short	88%	92%	91%

Table 6.4 Classification results for the FSCW machine

	FSCW machine					
	FEA Simulation			Experimental results		
Machine Status	K-NN	LDA	QDA	K-NN	LDA	QDA
Healthy	98%	100%	99%	95%	97%	96%
40% ECC	86%	85%	86%	79%	79%	78%
60% ECC	82%	82.5%	83%	80%	78%	75%
80% ECC	80%	82.5%	82.5%	75%	80%	80%
1 Magnet	92%	95%	95%	90%	92%	88%
2 Magnets	88%	92%	90%	90%	88%	89%
3 Magnets	90%	95%	94%	85%	89%	88%
10% short $R_f = 0.5\Omega$	90%	85%	90%	82%	80%	82%
10% short $R_f = 0.25\Omega$	90%	90%	90%	84%	88%	87%
20% short $R_f = 0.5\Omega$	90%	92%	91%	80%	90%	88%
20% short $R_f = 0.25\Omega$	92%	92%	90%	83%	91%	85%

ration using the commanded voltages approach for all tested machines (including the distributed winding machine) using the three classification methods.

The classification results show that the proposed algorithm was able to detect the fault type and estimate its severity accurately for different operating and environmental condi-

Table 6.5 The average classification results for all the tested machines

	Concentrated winding	Distributed winding		FSCW machine	
	FEA	FEA	EXP	FEA	EXP
KNN	83.4%	88.9%	83.9%	87.8%	82.8%
LDA	85.8%	90.1%	86.5%	88.8%	86.2%
QDA	84.9%	90%	85.1%	87.9%	86.2%

tions. However, at high operating loads, it was hard to classify eccentricity fault correctly since that the extra saturation due to eccentricity fault is masked because the machine is saturated at high operating torque.

Chapter 7

Conclusion

This work proposed a general algorithm for fault detection and identification in PMSMs under different operating conditions. The incremental inductance approach is proposed as a detection method when the motor is operating at standstill, the MCSA/MVSA and the commanded voltages approaches are proposed when the motor is operating at steady state. The main advantage of the methods is that it doesn't require any additional hardware components, the same signals that are used for the controller are used for detecting the fault type and estimating the severity. This makes the proposed methods cost efficient, easy to implement regarding the motor placement, and it remove the necessary to take the motor apart to detect the health status.

The incremental inductance approach is based on the change in the saturation in the machine under faulted condition compared to the healthy machine. Eccentricity and demagnetization faults directly affects the saturation in the machine. Therefore, using the incremental inductance can be most suitable to detect these two faults. Turn-to-turn short circuit fault doesn't cause a direct change in the saturation. Therefore, using the incremental inductance method can be used as an indicator for a short circuit fault, but the classification accuracy decreases when it comes to detect the severity of this fault.

The main advantage for the commanded voltage approach is that it can be applied during normal operation of the machine. The results show a high accuracy in detecting demagnetization and short circuit faults. Eccentricity showed a high detection classification

at lower torque level. However, as the operating torque increases, the detection accuracy decrease. Therefore, this method can be suitable for detecting demagnetization and short circuit faults regardless of the operating load.

The MCSA is the most straightforward method for fault detection. This method can be applied for detecting all three faults during steady state operation. However, in order to have a high classification accuracy, a large number of samples is required to cover the whole operating range. which might not be possible and easy to obtain.

BIBLIOGRAPHY

BIBLIOGRAPHY

[1] W. le Roux, R. Harley, and T. Habetler, "Detecting rotor faults in low power permanent magnet synchronous machines," *IEEE Trans. Power Electron.*, vol. 22, pp. 322–328, Jan 2007.

[2] Y. Da, X. Shi, and M. Krishnamurthy, "A new approach to fault diagnostics for permanent magnet synchronous machines using electromagnetic signature analysis," *IEEE Trans. Power Electron.*, vol. 28, pp. 4104–4112, Aug 2013.

[3] Z. Yang, X. Shi, and M. Krishnamurthy, "Vibration monitoring of PM synchronous machine with partial demagnetization and inter-turn short circuit faults," in *2014 IEEE Transportation Electrification Conference and Expo (ITEC)*, pp. 1–6, June 2014.

[4] "Report of large motor reliability survey of industrial and commercial installations, part I," *IEEE Trans. Ind. App.*, vol. IA-21, pp. 853–864, July 1985.

[5] B. Ebrahimi, M. Javan Roshtkhari, J. Faiz, and S. Khatami, "Advanced eccentricity fault recognition in permanent magnet synchronous motors using stator current signature analysis," *IEEE Trans. Ind. Electron.*, vol. 61, pp. 2041–2052, April 2014.

[6] S. Rajagopalan, W. Roux, T. Habetler, and R. Harley, "Dynamic eccentricity and demagnetized rotor magnet detection in trapezoidal flux (brushless DC) motors operating under different load conditions," *IEEE Trans. Power Electron.*, vol. 22, pp. 2061–2069, Sept 2007.

[7] B. Ebrahimi and J. Faiz, "Feature extraction for short-circuit fault detection in permanent-magnet synchronous motors using stator-current monitoring," *IEEE Trans. Power Electron.*, vol. 25, pp. 2673–2682, Oct 2010.

[8] J. Rosero, L. Romeral, J. Ortega, and E. Rosero, "Short-circuit detection by means of empirical mode decomposition and wigner-ville distribution for PMSM running under dynamic condition," *IEEE Trans. Ind. Electron.*, vol. 56, pp. 4534–4547, Nov 2009.

[9] J. Rosero, J. L. Romeral, J. Cusido, J. A. Ortega, and A. Garcia, "Fault detection of eccentricity and bearing damage in a pmsm by means of wavelet transforms decomposition of the stator current," in *Applied Power Electronics Conference and Exposition, 2008. APEC 2008. Twenty-Third Annual IEEE*, pp. 111–116, Feb 2008.

[10] S. Rajagopalan, J. A. Restrepo, J. M. Aller, T. G. Habetler, and R. G. Harley, "Nonstationary motor fault detection using recent quadratic time-frequency representations," *IEEE Transactions on Industry Applications*, vol. 44, pp. 735–744, May 2008.

[11] S. Rajagopalan, J. M. Aller, J. A. Restrepo, T. G. Habetler, and R. G. Harley, "Detection of rotor faults in brushless dc motors operating under nonstationary conditions," *IEEE Transactions on Industry Applications*, vol. 42, pp. 1464–1477, Nov 2006.

[12] Z. Yang, X. Shi, and M. Krishnamurthy, "Vibration monitoring of pm synchronous machine with partial demagnetization and inter-turn short circuit faults," in *2014 IEEE Transportation Electrification Conference and Expo (ITEC)*, pp. 1–6, June 2014.

[13] K. Alameh, N. Cite, G. Hoblos, and G. Barakat, "Feature extraction for vibration-based fault detection in permanent magnet synchronous motors," in *2015 Third International Conference on Technological Advances in Electrical, Electronics and Computer Engineering (TAEECE)*, pp. 163–168, April 2015.

[14] D. Torregrossa, A. Khoobroo, and B. Fahimi, "Prediction of acoustic noise and torque pulsation in pm synchronous machines with static eccentricity and partial demagnetization using field reconstruction method," *IEEE Trans. Ind. Electron.*, vol. 59, pp. 934–944, Feb 2012.

[15] B. Ebrahimi and J. Faiz, "Magnetic field and vibration monitoring in permanent magnet synchronous motors under eccentricity fault," *IET Electric Power Applications*, vol. 6, pp. 35–45, January 2012.

[16] M. Khov, J. Regnier, and J. Faucher, "Monitoring of turn short-circuit faults in stator of pmsm in closed loop by on-line parameter estimation," in *IEEE International Symposium Diagnostics for Electric Machines, Power Electronics and Drives, 2009. SDEMPED 2009.*, pp. 1–6, Aug 2009.

[17] J. Lee, Y.-J. Jeon, D. chul Choi, S. Kim, and S. W. Kim, "Demagnetization fault diagnosis method for pmsm of electric vehicle," in *39th Annual Conference of the IEEE Industrial Electronics Society, IECON 2013*, pp. 2709–2713, Nov 2013.

[18] N. Leboeuf, T. Boileau, B. Nahid-Mobarakeh, N. Takorabet, F. Meibody-Tabar, and G. Clerc, "Estimating permanent-magnet motor parameters under inter-turn fault conditions," *IEEE Trans. Magnetics*, vol. 48, pp. 963–966, Feb 2012.

[19] P. Yulong, L. Xing, L. Yi, and C. Feng, "Effect of air gap eccentricity on rotor eddy current loss in high speed PMSM used in FESS," in *2014 17th International Symposium Electromagnetic Launch Technology (EML)*, pp. 1–6, July 2014.

[20] J. Hong, S. Park, D. Hyun, T. june Kang, S. B. Lee, C. Kral, and A. Haumer, "Detection and classification of rotor demagnetization and eccentricity faults for PM synchronous motors," *IEEE Trans. Ind. App.*, vol. 48, pp. 923–932, May 2012.

[21] M. Kim, S.-K. Sul, and J. Lee, "A stator turn-fault detection method for inverter-fed ipmsm with high-frequency current injection," in *2013 IEEE Energy Conversion Congress and Exposition (ECCE)*, pp. 3528–3533, Sept 2013.

[22] T. Ilamparithi, S. Nandi, and J. Subramanian, "A disassembly-free offline detection and condition monitoring technique for eccentricity faults in salient-pole synchronous machines," *IEEE Transactions on Industry Applications*, vol. 51, pp. 1505–1515, March 2015.

[23] W. Le Roux, R. Harley, and T. Habetler, "Detecting faults in rotors of PM drives," *IEEE Industry Applications Magazine*, vol. 14, pp. 23–31, March 2008.

[24] S. Nandi, H. A. Toliyat, and X. Li, "Condition monitoring and fault diagnosis of electrical motors-a review," *IEEE Transactions on Energy Conversion*, vol. 20, pp. 719–729, Dec 2005.

[25] S. Rajagopalan, J. Aller, J. Restrepo, T. Habetler, and R. Harley, "Detection of Rotor Faults in Brushless DC Motors Operating Under Nonstationary Conditions," *IEEE Trans. Ind. App.*, vol. 42, pp. 1464–1477, Nov 2006.

[26] S. Nandi, S. Ahmed, and H. Toliyat, "Detection of rotor slot and other eccentricity related harmonics in a three phase induction motor with different rotor cages," *IEEE Trans. Energy Conv.*, vol. 16, pp. 253–260, Sep 2001.

[27] Z. Zhu, L. Wu, and M. Mohd Jamil, "Influence of Pole and Slot Number Combinations on Cogging Torque in Permanent-Magnet Machines With Static and Rotating Eccentricities," *IEEE Trans. Ind. App.*, vol. 50, pp. 3265–3277, Sept 2014.

[28] T. Goktas, M. Zafarani, and B. Akin, "Separation of broken magnet and static eccentricity failures in pmsm," in *2015 IEEE International Electric Machines Drives Conference (IEMDC)*, pp. 1459–1465, May 2015.

[29] Y. Da, X. Shi, and M. Krishnamurthy, "Health monitoring, fault diagnosis and failure prognosis techniques for brushless permanent magnet machines," in *2011 IEEE Vehicle Power and Propulsion Conference (VPPC)*, pp. 1–7, Sept 2011.

[30] M. K. Mohanty, *Direct torque control of permanent magnet synchronous motor drives with conventional and svm approach*. PhD thesis, 2014.

[31] Z. Zhu, D. Howe, E. Bolte, and B. Ackermann, "Instantaneous magnetic field distribution in brushless permanent magnet DC motors. I. open-circuit field," *IEEE Trans. Magnetics*, vol. 29, pp. 124–135, Jan 1993.

[32] Z. Zhu and D. Howe, "Instantaneous magnetic field distribution in brushless permanent magnet DC motors. II. armature-reaction field," *IEEE Trans. Magnetics*, vol. 29, pp. 136–142, Jan 1993.

[33] Z. Zhu and D. Howe, "Instantaneous magnetic field distribution in brushless permanent magnet DC motors. III. effect of stator slotting," *IEEE Trans. Magnetics*, vol. 29, pp. 143–151, Jan 1993.

[34] Z. Zhu and D. Howe, "Instantaneous magnetic field distribution in permanent magnet brushless dc motors. IV. magnetic field on load," *IEEE Trans. Magnetics*, vol. 29, pp. 152–158, Jan 1993.

[35] L. Cappelli, Y. Coia, F. Marignetti, and Z. Zhu, "Analysis of Eccentricity in Permanent-Magnet Tubular Machines," *IEEE Trans. Ind. Electron.*, vol. 61, pp. 2208–2216, May 2014.

[36] M. Michon, R. C. Holehouse, K. Atallah, and G. Johnstone, "Effect of rotor eccentricity in large synchronous machines," *IEEE Transactions on Magnetics*, vol. 50, pp. 1–4, Nov 2014.

[37] W. Thomson and A. Barbour, "On-line current monitoring and application of a finite element method to predict the level of static airgap eccentricity in three-phase induction motors," *IEEE Trans. Energy Conversion*, vol. 13, pp. 347–357, Dec 1998.

[38] S. N. Foster, J. G. Cintron-Rivera, and E. G. Strangas, "Detection of incipient stator winding faults in PMSMs with single-layer fractional slot concentrated windings," *Electric Power Systems Research*, vol. 131, pp. 231 – 243, 2016.

[39] K. Rahman and S. Hiti, "Identification of machine parameters of a synchronous motor," *IEEE Trans. Ind. App.*, vol. 41, pp. 557–565, March 2005.

[40] J. Cintron-Rivera, A. Babel, E. Montalvo-Ortiz, S. Foster, and E. Strangas, "A simplified characterization method including saturation effects for permanent magnet machines," in *2012 XXth International Conference Electrical Machines (ICEM)*, pp. 837–843, Sept 2012.

[41] M. N. Murty and V. S. Devi, *Pattern recognition: An algorithmic approach*. Springer Science & Business Media, 2011.

[42] A. M. Martinez and A. Kak, "PCA versus LDA," *IEEE Trans. Pattern Anal. Mach. Intell.*, vol. 23, pp. 228–233, Feb 2001.